MEMBRANE BENDING IS CRITICAL FOR ASSESSING THE THERMODYNAMIC STABILITY OF PROTEINS IN THE MEMBRANE

by

Keith M. Callenberg

B.S., San Jose State University, 2008

Submitted to the Graduate Faculty of the
Dietrich School of Arts and Sciences in partial fulfillment
of the requirements
for the degree of Doctor of Philosophy

University of Pittsburgh

2013

UNIVERSITY OF PITTSBURGH

DIETRICH SCHOOL OF ARTS AND SCIENCES

This dissertation was presented

by

Keith M. Callenberg

It was defended on

July 30, 2013

and approved by

Dr. Daniel M. Zuckerman, Assistant Professor, Department of Computational and Systems Biology, University of Pittsburgh

Dr. Patrick C. A. van der Wel, Assistant Professor, Department of Structural Biology, University of Pittsburgh

Dr. Christopher J. Langmead, Associate Professor, Department of Computer Science, Carnegie Mellon University

Dissertation Director: Dr. Michael Grabe, Associate Professor, Department of Biological Sciences, University of Pittsburgh

MEMBRANE BENDING IS CRITICAL FOR ASSESSING THE THERMODYNAMIC STABILITY OF PROTEINS IN THE MEMBRANE

Keith M. Callenberg, Ph.D.

University of Pittsburgh, 2013

The ability of biological membranes to bend is critical to understanding the interaction between proteins and the lipid bilayer. Experimental and computational studies have shown that the membrane can bend to expose charged and polar residues to the lipid headgroups and water, greatly reducing the cost of protein insertion. However, current computational approaches are poorly equipped to accurately model such deformation; atomistic simulations often do not reach the time-scale necessary to observe large-scale rearrangement, and continuum approaches assume a flat, rigid bilayer. In this thesis we present an efficient computational model of a deformable membrane for probing these interactions with elasticity theory and continuum electrostatics.

To validate the model, we first investigate the insertion of three membrane proteins and three aqueous proteins. The model finds the membrane proteins and aqueous proteins stable and unstable in the membrane, respectively. We also investigate the sensitivity of these predictions to changes in several key parameters.

The model is then applied to interactions between the membrane and the voltage sensor segments of voltage-gated potassium channels. Despite their high numbers of basic residues, experiments have shown that voltage sensors can be stably accommodated in the membrane. For simple continuum electrostatics approaches that assume a flat membrane, the penalty of inserting these charged residues would seem to prohibit voltage sensor insertion. However, in our method the membrane deforms to enable interaction between solvent and the charged residues. Our calculations predict that the highly charged S4 helices of several potassium channels are in fact stable in the membrane, in accord with experimental observations.

Experimental and computational evidence has shown that the cost for inserting multiple charged amino acids into the membrane is not additive; it is not as costly to insert a second charge once a first has already been inserted. Our model reflects this phenomenon and provides a simple mechanical explanation linked to membrane deformation.

We additionally consider the energetics of passive ion penetration into the membrane from bulk solvent. We use coarse-grained molecular dynamics to guide our input parameters and show that ion permeation energy profiles agree with atomistic simulations when membrane bending is included.

Acknowledgements

I would like to thank my advisor for teaching me to think scientifically, my parents for their love and support, and my wife and son for sharing the beautiful ups and downs of every day with me.

I dedicate this work to my son, Michael Augustine.

Contents

List of Figures

List of Tables

Chapter 1

Introduction

1.1 Background and motivation

Functionally, membranes separate the cell from its external environment. They delineate organelles from the cytoplasm, and this compartmentalization is essential for carrying out specialized chemistry in the cytoplasm and the lumen of the golgi, mitochondria, endoplasmic recticulum, and other cellular spaces. Without the membrane, the cell cannot survive. Indeed, the functional mechanism of many antimicrobial small molecules and peptides is to open pores in the cell membrane that ultimately lead to rupture and cell death.

However, compartmentalization is not all that membranes do; they serve as a platform for the organization of the channels, transporters, and signaling membrane proteins that control the flow of material and information from one side of the membrane to the other. Membranes determine the nature of all communication that goes on between the inside and the outside of the cell or organelle. The biological membrane is the gatekeeper that directly or indirectly determines what can pass through. Also, most of the fundamental biochemical functions of cells involve membranes at some point in their arc, including: protein synthesis, DNA replication in prokaryotes, protein secretion, and hormonal responses.

Compositionally, membranes are structured as bilayers, largely composed of amphipathic lipid molecules. The term "amphipathic" means two natures, and indicates that lipids typically feature a hydrophilic polar headgroup and a hydrophobic acyl tail. The hydrophobic tails sequester away from water, creating a highly nonpolar environment in the center of the membrane. However, biological membranes are more than just simple lipids; membranes are teeming with diversity. Charged lipids, rafts, sterols, cytoskeletal

connection, and diverse proteins change the structure and behavior of the membrane. This diversity comes about largely because of the broad range of functions performed by the proteins embedded in the membrane.

There are a wide variety of important functions performed by proteins that live in the membrane. Membrane receptor proteins respond to and transmit signals in and out of the cell or organelle. Ion channels and transporters shuttle solutes across the membrane that would otherwise rarely cross the hydrophobic membrane core. Membrane enzymes such as oxidoreductases, transferases and hydrolases are another large class, along with cell adhesion molecules that enable interaction between cells.

The lipid hydrocarbon tails create a highly hydrophobic membrane core that is inhospitable to charged and polar species. As a result, proteins that embed in the membrane are generally structured to present nonpolar residues to the lipid acyl chains and charged and polar residues to the lipid polar headgroups and water. There are notable circumstances, however, in which charged molecules must pass through or reside in the membrane for normal biological function. Indeed, many charged residues found in transmembrane protein segments are evolutionarily conserved [3]. In particular, the voltage sensor domains of voltage-gated potassium channels contain five to six charged residues that are essential to channel opening and closing, and evidence suggests these domains reside in the transmembrane region. Another interesting example is the HIV TAT protein, which is known to cross membranes quickly despite its large number of charged arginine residues [4].

Classic studies of the thermodynamic properties of amino acid analogs suggest that 65-80 kcal/mol of energy is required for charged residues to enter organic phases from aqueous solution [5]. However, experiments harnessing the translocon [6] and outer membrane proteins [7] have shown that membrane insertion energies for charged groups are significantly lower. Molecular dynamics simulations propose that membrane bending stabilizes charged residues by allowing water molecules access to the otherwise buried charge [8, 9]. This is in agreement with experiments showing that the bilayer thins in the presence of a charged voltage sensor domain and that the domain is hydrated in the membrane [10]. The driving hypothesis of this thesis is that membrane bending plays a central role in explaining the discrepancy between the behavior of the bulk matter and what occurs in living systems.

How can we test whether membrane deformation is at the heart of these observations? While experimental methods are ideal – they should always be considered the gold standard – the scale of this question is small and requires precision. Experiments often do not have the spatial or temporal resolution to distinguish what is happening at the molecular level. To get at the heart of what is physically occurring, models and

theory are needed to go hand-in-hand with experiment. Additionally, because of the extreme diversity present in membranes and embedded proteins, some might question the general applicability of results from any particular experimental protein-membrane system. Experimental methods are also often costly and do not often scale well. For these reasons, we have explored this question with a theoretical and computational approach, backed by experimental observations whenever possible.

While molecular dynamics methodologies have been used to answer many important biochemical and biophysical questions, they are unable to sample long enough to reach equilibrium in many situations. This is especially relevant when considering conformational changes of large protein complexes in the membrane such as voltage-gated channels, and BAR domains that adhere to and induce large scale curvature. Correlated with the sampling issue is the high computational expense of atomistic molecular dynamics. Coarse-grained models have been developed to reduce the degrees of freedom, thereby reducing the computational expense, but despite this, much of the same sampling issue remains.

We therefore turn to continuum models which simplify these calculations by treating the membrane and surrounding aqueous environment as continuous substances rather than thousands of discrete particles. This dramatically reduces the number of calculations that must be carried out for any given situation. In our model we focus on three energy components: elasticity, electrostatics, and nonpolar solvation. Since membrane bending is essential to our primary question, we need a model that allows for distortion in the lipid bilayer; elasticity theory has been used for over 30 years to successfully describe membrane shapes. Electrostatics is the primary energy opposing permeation, as discussed above. Nonpolar water reorganization is an important driving force for the folding of proteins, and it stabilizes molecules in the greasy interior of the membrane away from water. In Chapter 2 and chapters that follow, we will clearly define the terms in this model more precisely. In the rest of this chapter we will place our model in the context of previous work, and then describe the general outline of the dissertation.

1.2 A brief history of continuum models for studying the interaction of ions and proteins with the membrane

From the electrostatics perspective, Parsegian pioneered analytical calculations of charged species in membranes with a study of an ion passing through a low-dielectric slab [11]. Ben-Tal and co-workers, as well as Roux, built upon this theory to propose models of peptide association that were more complex and required numerics [12, 13]. These studies introduced a higher level of detail with all-atom representations of the proteins.

Classical elastostatics were initially proposed by Helfrich to describe the equilibrium shape of the membrane [14]. This theory was first applied to radially symmetric protein inclusions by Huang [15] and expanded to include mean bending, bilayer compression, and surface tension by Andersen and colleagues [16]. Elastostatics, along with continuum field theories, were later used to develop models of protein-protein interactions mediated by the membrane [17–19]. These models could all be solved analytically because they did not treat the protein in atomic detail, and they ignored many of the other molecular forces such as hydrophobic forces and electrostatics.

More recently, the Mosberg Lab developed a continuum model for investigating the orientation and stability of proteins in the membrane called Positioning of Proteins in Membranes (PPM) [20]. The PPM model is largely based on the calculation of solvent accessible surface area, parameterized using values from the partitioning of small molecules between aqueous and organic phases. The computational efficiency of PPM has led to its application to nearly all publicly available membrane protein structures, catalogued in a useful online database named Orientations of Proteins in Membranes (OPM) [21].

Up to this point, no studies had yet integrated membrane deformation with continuum electrostatics. The Grabe lab was the first to do so in its development of a model that incorporated elasticity theory from Helfrich with Poisson-Boltzmann electrostatics and a nonpolar solvation term [22]. Following this, the Weinstein lab developed a multiscale method that combined MD simulations with an elastic representation of the membrane [23–25]. In their model, atomistic MD simulations are performed and time-averaged in order to set the protein-membrane contact boundary in the continuum representation. The Weinstein lab applies this model to quantify the energetics of membrane deformations presented by the simulations.

While these recent models from the Mosberg and Weinstein labs have demonstrated utility for several important applications, they are not particularly well-suited for answering whether membrane deformation is essential for charge insertion. In the Weinstein model, the free energy of insertion is given only by a difference in accessible surface area. While the surface area is parameterized to effectively minimize hydrophobic mismatch and expose polar residues to water, the theory by which it does so is relatively unproven. The Weinstein model additionally requires MD simulations, reducing its computational efficiency. On the other hand, the PPM model does not require external simulations and is highly efficient. The authors of the PPM model have also presented some rigorous validation of their method based on the predicted hydrophobic thickness compared to experimental measurements. However, the PPM model is based on a rigid slab

membrane that cannot deform and react to the presence of the protein as a biological membrane can.

We present in this thesis a method that builds upon the earlier work in the Grabe lab that utilizes elasticity theory, continuum electrostatics, and a term for nonpolar solvation. In the extended model, the calculation of these energy terms is uniquely coupled with a search algorithm to optimize the membrane shape surrounding a transmembrane protein. This development enables us to probe and explore a much broader range of biological systems as shown in the chapters that follow.

1.3 Outline of this thesis

This dissertation is organized as follows:

Chapter 2 introduces the model and demonstrates its ability to discriminate between water soluble and membrane proteins. In this chapter we also investigate the sensitivity of the model to several key parameters.

Chapter 3 investigates the insertion of isolated voltage sensor segments of voltage-gated potassium channels. It also applies the model to permeation of a hydrophobic peptide, and the identification of the hydrophobic segment of a large ion channel. Additionally, Chapter 3 provides a simple mechanical basis for the non-additivity of charge insertion into the membrane.

Chapter 4 discusses the passive permeation of ions through the membrane and shows that the results of our model based on continuum theory are in good agreement with results from coarse-grained and atomistic molecular dynamics.

Chapter 5 presents the electrostatics underpinning our model and a freely distributed, open source graphical interface for performing these calculations on a flat membrane.

Finally, Chapter 6 summarizes our results and discusses several future directions for extending the numerics of the model and applying it to new biological problems.

Chapter 2

A computational model for predicting the stability of proteins in the membrane: validation and analysis

2.1 Introduction

There is a need for quantitative models that predict the stability and interaction of membrane proteins with the membrane. There is a need at not only a fundamental level so that we have a deeper and more accurate understanding of membrane protein interactions with the membrane, but also from a practical perspective. Molecular dynamics cannot sample long enough to achieve true equilibrium. Coarse-grained models are a good start, but they still have sampling issues and they must be parameterized. On the other hand, continuum methods are fast and they have been used for a very long time, so they have been parameterized to some extent.

The goal of this chapter is twofold: 1) we introduce the theoretical framework for our continuum model of protein interactions with the membrane and 2) we test the model against a set of known water soluble and known membrane proteins. We apply the model to a range of biological systems in the following chapters, but here we focus on the theory and validation of the model by identifying the key parameters, examining how the predictions depend on these key parameters, and comparing the model with test systems.

As we will discuss, there are three energetic terms in our model. The first term, and the one that is unique to our model, is the elastostatic treatment of the membrane. The second term is the continuum electrostatics for which we use Poisson-Boltzmann theory. Finally, we also include a nonpolar solvation energy term. While Poisson-Boltzmann theory is the gold standard for continuum electrostatics, there is not a standard, well-accepted nonpolar energy formulation when considering the partitioning of large molecules and proteins into membranes. For this reason we explore the impact of this term by comparing the results from two different nonpolar models.

2.2 Theory and Methods

We employ a physics-based continuum model to investigate the stability of proteins in the membrane. We model the total insertion energy, ΔG_{total}, as the sum of three energy components:

$$\Delta G_{total} = \Delta G_{mem} + \Delta G_{elec} + \Delta G_{np} \tag{2.1}$$

where the first term on the right-hand side (ΔG_{mem}) is the energy associated with distortion in the membrane caused by embedding the protein, the second term (ΔG_{elec}) is the electrostatic cost required to move the charged protein from solution into the low-dielectric environment of the membrane, and the final term (ΔG_{np}) is the nonpolar or hydrophobic energy gained by removing portions of the protein surface from water and burying them in the membrane. All energies are calculated with respect to the protein free in solution far from an unstressed membrane; negative values therefore indicate stabilization in the membrane.

2.2.1 Elastic energy

Membranes are made up of lipids that have a headgroup that interacts with water and a nonpolar tail that is sequestered away from the water. The shape and energy of the membrane in our model are determined using linear elasticity theory, in which each leaflet is described by a thin surface in polar coordinates, $u(\mathrm{r},\theta)$, illustrated in Fig. 2.1, with material properties that can be tuned to the membrane of interest. The total membrane deformation energy is given by:

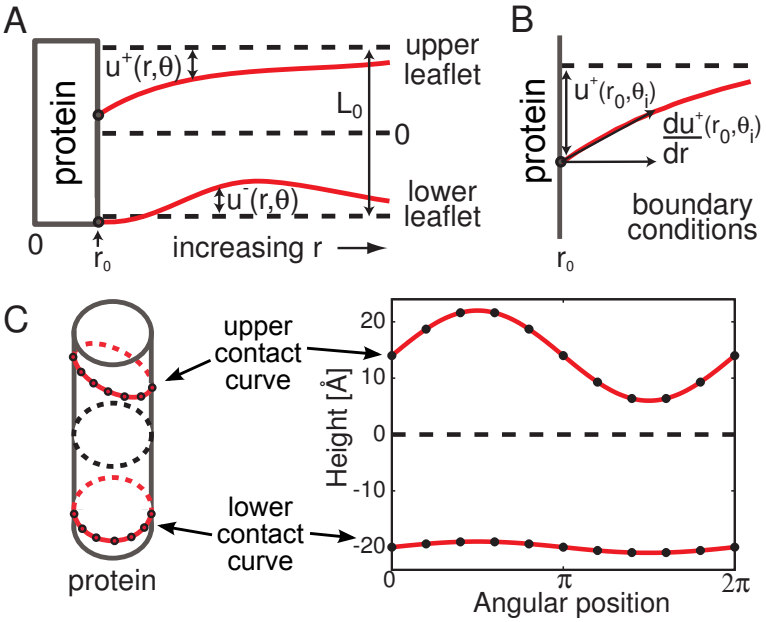

FIGURE 2.1: Geometry of the system.

A) Cross section showing membrane distortions in the upper and lower leaflets. Solid red lines indicate the membrane-water interfaces. Dashed black lines indicate the equilibrium heights of the membrane leaflets and the midplane at z=0. The equilibrium bilayer thickness is L_0. B) The protein-membrane contact angle is proportional to the height deviation from equilibrium. C) The protein (gray) is shown in a 3-D representation with red curves indicating the height of the upper and lower leaflets as they contact the protein transmembrane segment. Black nodes on these curves are used as the boundary conditions for solving the elasticity equation. The numeric values of these nodes are optimized by the search algorithm. 2-D representation of upper and lower contact curves are shown on the right.

$$\begin{aligned}\Delta G_{mem} = \frac{1}{2}\int_\Omega & \frac{K_a}{L_0^2}(u^- - u^+)^2 + \dots \\ & \frac{K_c}{2}\left((\nabla^2 u^-)^2 + (\nabla^2 u^+)^2\right) + \dots \\ & \frac{\alpha}{2}\left((\nabla u^-)^2 + (\nabla u^+)^2\right) d\Omega, \end{aligned} \tag{2.2}$$

where u^+ is the shape of the upper leaflet and u^- is the shape of the lower leaflet; L_0 is the equilibrium thickness of the membrane, K_c is the membrane bending energy, α is the surface tension, and K_a is the compression modulus. The energy of the upper and lower leaflets are coupled through the compression modulus. The functional derivative of Eq. 2.2 with respect to variations in u^+ and u^- gives the partial differential equation (PDE) that determines the shapes of each leaflet. Each surface obeys the following PDE:

TABLE 2.1: Base parameters for all calculations

Parameter	**Value**
Electrostatics Grid Dimensions	$161 \times 161 \times 161$ Å^3
Counter-Ions	0.1 M symmetric salt
Protein Dielectric	2.0
Membrane Dielectric	2.0
Headgroup Dielectric	80.0
Solvent Dielectric	80.0
Solvent Probe Radius	1.4 Å
Surface Sphere Density	10.0 grid points/Å^2
Temperature	298.15 K
Membrane Thickness	See Table 2.2
Headgroup Thickness	8.0 Å
Bending modulus (K_c)	See Table 2.2
Compression modulus (K_a)	See Table 2.2
Surface tension (α)	3.00×10^{-13} NÅ

TABLE 2.2: Elastic membrane material properties

Lipid type	**Thickness**	K_a	K_c
GMO [16]	42.0 Å	1.425×10^{-11} N/Å	2.85×10^{-10} NÅ
POPC [26]	43.1 Å	2.30×10^{-11} N/Å	8.5×10^{-10} NÅ

$$\begin{aligned} \nabla^4 u^+ - \gamma \nabla^2 u^+ + \beta(u^+ - u^-) &= 0 \\ \nabla^4 u^- - \gamma \nabla^2 u^- + \beta(u^- - u^+) &= 0. \end{aligned} \tag{2.3}$$

where $\gamma = \alpha/K_c$ and $\beta = 2K_a/(L_0^2 K_c)$. The last term on the left-hand side of each equation couples the upper and lower leaflets. This coupled set of fourth-order equations requires two boundary conditions to be specified on the inner boundary, where the bilayer contacts the protein, and at the outer boundary, far from the protein. We assume that the membrane is flat at its equilibrium length, L_0, far from the protein. We solve this equation for $u^+(r,\theta)$ and $u^-(r,\theta)$ together applying height and contact angle boundary conditions at the membrane-protein interface as described below and shown in Fig. 2.1B. After solving for $u^+(r,\theta)$ and $u^-(r,\theta)$, the total membrane energy is determined by carrying out the integral in Eq. 2.2.

Elastic properties In the case where the membrane must bend to incorporate a protein, you can imagine that the elastic properties of the membrane will drastically affect the protein stability. Elastic properties including the compression and bending moduli

were taken from experimental values for glyceryl monooleate (GMO) [16] and palmitoyloleoylphosphatidylcholine (POPC) membranes [26]. Membrane material properties are shown in Table 2.2. The total bilayer thickness was calculated by taking the experimental D_{HH} value that represents the phosphate-phosphate distance and adding 16 Å for the headgroup thickness [27].

2.2.2 Electrostatic energy

The electrostatic energy of the protein, G_{elec}, is highly dependent on the local dielectric environment, and there is a large energetic cost for moving charged and polar residues into the membrane [28]. We determine the electrostatic potential, Φ, by solving the Poisson-Boltzmann equation:

$$-\nabla \cdot [\epsilon(r)\nabla\phi(r)] + \kappa^2(r)sinh[\phi(r)] = \frac{e}{k_B T} 4\pi\rho(r), \tag{2.4}$$

where $\phi = \Phi/k_B T$ is the reduced electrostatic potential, κ is the Debye-Huckel screening coefficient to account for ionic shielding, ϵ is the spatially-dependent dielectric constant, e is the electron charge and ρ is the charge density within the protein. The total electrostatic energy is then given by:

$$G_{elec} = \int \Phi \, \rho \; dx \, dy \, dz. \tag{2.5}$$

In solution, ϵ was set to the value of water for all points outside of the protein molecular surface while ϵ is modified to take on values corresponding to the membrane for all points between the upper surface, u^+, and lower surface, u^-, determined from solving Eq. 2.2. Additionally, κ is set to zero for points between u^+ and u^- indicating a lack of ion penetration into the membrane. ΔG_{elec} is then given by the difference between the electrostatic energies calculated in solution and in the presence of the membrane. A detailed description of the manipulations to the microenvironment of the protein in the presence of the membrane can be found in Chapter 5 and [29].

2.2.3 Nonpolar energy

There is an energetic penalty for placing solutes in water due to the disruption of the water hydrogen bond network. We model this penalty by assuming that the energy difference of the protein in solution compared to the protein in the membrane, ΔG_{np},

is proportional to the difference in the protein's solvent accessible surface area (SASA) between solution and the membrane [30]:

$$\Delta G_{np} = a \cdot (A_{mem} - A_{sol}), \tag{2.6}$$

where A_{mem} is the protein SASA in the membrane, A_{sol} is the total protein SASA, and $a = 0.028$ kcal/mol·Å^2. The a constant has been determined based on the partitioning of small molecules between aqueous and organic phases [31]. SASA values are calculated with a modified Shrake-Rupley algorithm [32] using the solvent-accessible surface representation of the protein with a 1.4 Å water probe radius. In the presence of the membrane, if the point on the surface of the protein lies between the upper, u^+, and lower, u^-, leaflets then it is considered occluded and does not contribute to A_{mem}. MATLAB's cubic interpolation function was used to navigate between the position of the point on the protein surface and the grid points describing the upper and lower membrane surfaces.

Alternative nonpolar method We implemented a nonpolar model similar to the Positioning of Proteins in Membranes (PPM) method developed by Lomize and colleagues [20]. The PPM method calculates the transfer free energy for moving atoms into the membrane using a SASA-based model:

$$\Delta G_{transfer} = \sum_{i=1}^{N} ASA_i \ \sigma_i \ f(z_i) \tag{2.7}$$

where N is the number of atoms in the protein, σ_i is the atomic solvation parameter that varies based on atom type, ASA is the solvent accessible surface area, and $f(z)$ is the water concentration gradient at the z-position of the atom. Several sets of σ parameters were presented and tested by the PPM model [20]. We used the σ parameters derived from the decadiene experiments [33]. The water concentration gradient f is used to scale the energetic effect of atoms based on their depth in the membrane. We did not include f in our implementation because the depth dependence it reproduces is already accounted for in our model by the electrostatic energy.

2.2.4 Preparation of protein structures

Protein X-ray structures were downloaded from the Protein Data Bank. All non-protein atoms such as waters and ligands were removed from the structure. PDB2PQR version 1.8 was used with the CHARMM forcefield to assign partial charges and radii

[34, 35]. Finally, all proteins were oriented in the membrane using the Auto-Orient function of APBSmem [29]. The Auto-Orient feature calculates the principal axes of the molecule and aligns the longest axis to the Z normal, perpendicular to the membrane. This assumption was appropriate for the membrane proteins as this orientation minimizes hydrophobic mismatch. For the aqueous proteins it is less clear that lower energy transmembrane orientations do not exist. However, aligning the longest axis perpendicular to the membrane plane presented the least amount of charged residues to the hydrophobic membrane core compared to other fully transmembrane orientations. We therefore believe these are the lowest energy transmembrane orientations for these aqueous proteins.

2.2.5 Determining the inner radius

In coupling the elastic, nonpolar, and electrostatic energy components it is necessary to define the inner radius, r_0, at which the membrane contacts the protein. A method, illustrated in Figure 2.2, was developed to automatically calculate the radius for the cylindrical approximation of the protein. Briefly, the van der waals radii of all protein atoms are first projected onto a cartesian grid in the X-Y plane. Grid points on the outer boundary of the protein are then determined using a custom edge detection algorithm. The algorithm first identifies an arbitrary starting point on the outer boundary and then follows the boundary in a clockwise direction until the first point is encountered again. The distance from the origin is then calculated for all boundary points, and finally the median distance from the origin was selected as the inner radius r_0 of the membrane domain.

2.2.6 Identifying optimal protein-membrane contact shapes

To optimize the boundary conditions at the protein-membrane interface, $u(r_0, \theta)$, with respect to the minimum insertion energy, ΔG_{total}, we have coupled the insertion energy calculation to a search algorithm. We previously used Powell's method which is a conjugate gradient-based algorithm that does not require the calculation of derivatives [36]. We show in Chapter 3 and [37] that Powell's method performs well under several difficult situations including finding the lowest energy state for a peptide translated through the membrane. In Appendix A we also discuss several search strategies that speed up the search. However, conjugate gradient-based methods such as Powell's are best suited for local optimization, and have difficulty trouble escaping local minima. We have therefore adjusted our algorithm to begin with a simulated annealing approach for global optimization [38]. Once the simulated annealing method has reached a tolerance

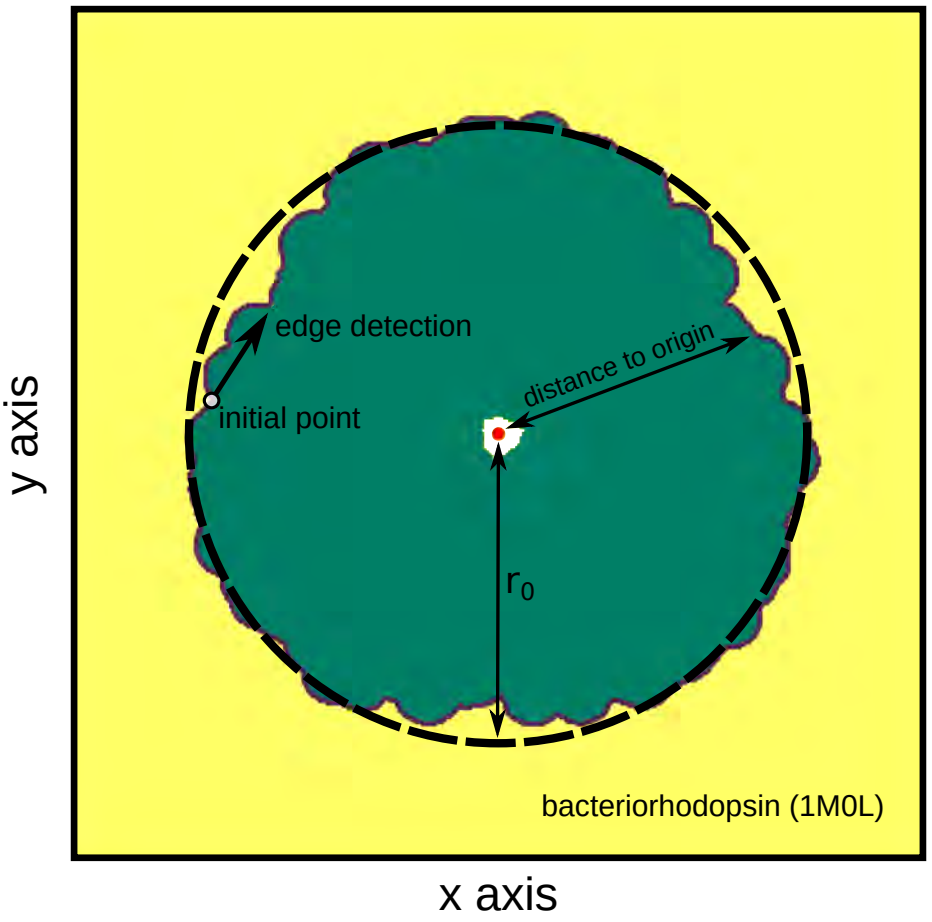

FIGURE 2.2: Determining the effective radius of the protein.

The protein (green) is projected onto the X-Y plane. Grid points on the protein's outer boundary (purple) are determined using an edge detection algorithm. The distances from all boundary points to the origin (red dot) are calculated and the median value is taken as the inner radius, r_0.

threshold, a trust region algorithm is used for local refinement of the boundary curve [39]. We find empirically that while this hybrid method does not always yield the optimal solution quickest, it is more sure to do so than Powell's method alone.

2.2.7 Contact slope

The slope at which the membrane contacts the protein, $\frac{du}{dr}$ (shown in Fig. 2.1), is also an important boundary condition that needs to be optimized. In order to avoid adding additional dimensions to our search space, we began each search by first optimizing the contact boundary curve for the upper and lower leaflets for each protein-membrane system while assuming a zero contact slope. Contact angle searches were then carried out to identify the optimal slope. Finally, the contact boundary curve was subsequently re-optimized with the optimal contact slope. To validate this approximation we performed several searches that included the contact slope as an extra dimension in the search and found that the total insertion energy of the approximation was always within 2 kcal/mol.

2.3 Results

The model was tested on three water soluble proteins and three membrane proteins. Several criteria were used to select protein structure candidates. First, since our model utilizes atomic detail for the electrostatic and nonpolar energy calculations, a high resolution x-ray structure is essential. Second, the protein must be definitively aqueous or definitively transmembrane. Some water soluble proteins are known to anchor, permeate, or otherwise interact with membranes. We avoided such structures in order to clearly separate the two classes of structures. Finally, the overall shape of the protein structure must be roughly cylindrical to be compatible with our current numeric method. This requirement comes partially from designing the current implementation of our elastic solver for polar coordinates. Additionally, and perhaps more importantly, since the two leaflets of the membrane are coupled through the compression term (see equation 2.3), all points in the upper leaflet must be matched by a point in the lower leaflet. Therefore, the shape of the protein at the upper leaflet should be fairly similar to the shape at the lower leaflet. Cylindrical geometry satisfies both of these conditions.

The three aqueous proteins we chose were chymotrypsin, insulin, and green fluorescent protein (GFP). Chymotrypsin is a serine protease located in the digestive system of vertebrates. The hormone insulin is a key component in the regulation of carbohydrate and fat metabolism. GFP is a beta-barrel protein derived from jellyfish that emits green fluorescence when exposed to ultraviolet light. A literature search was performed to confirm that these proteins are not known to independently interact with the membrane.

The three membrane proteins we chose were outer membrane protein A (OmpA), voltage-dependent anion channel (VDAC), and bacteriorhodopsin. OmpA is a porin found in the outer membrane of gram negative bacteria. VDAC is an ion channel with a large pore that localizes to the outer mitochondrial membrane. Bacteriorhodopsin is a proton pump found in archaebacteria that utilizes light energy to transfer protons across the membrane.

2.3.1 Elastostatics: membrane stiffness regulates insertion

We started by exploring how changes to membrane stiffness influenced protein stability in the membrane. Glyceryl monooleate (GMO) is a synthetic compound that forms highly flexible membranes. Although it is not found in nature, GMO proved to be essential for early studies in membrane biophysics by providing a robust, solvent-free membrane system [40]. Palmitoyloleoylphosphatidylcholine (POPC) is a standard lipid found in eukaryotic cells that forms stiffer, physiologically-relevant membranes.

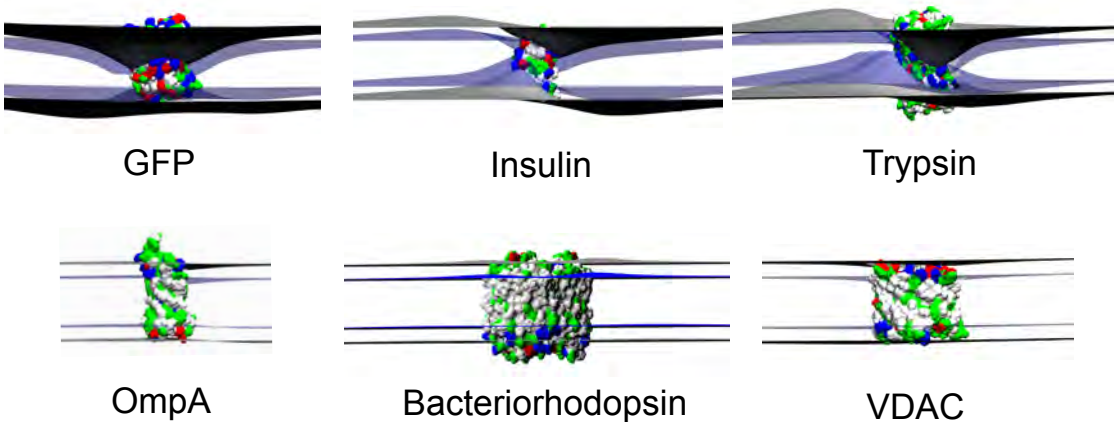

FIGURE 2.3: Optimal membrane deformation for 3 aqueous proteins (top row) and 3 membrane proteins (bottom row).

The upper and lower leaflets of the bilayer are represented as gray surfaces while the membrane headgroup-core interfaces are depicted as transparent blue surfaces. The bilayer deforms only slightly for the membrane proteins, while dramatic membrane deformation is predicted for the aqueous proteins. The "pinched" state observed in the water soluble proteins minimizes the amount of polar and charged residues exposed to the low dielectric of the membrane core. Proteins are displayed in a molecular surface representation and colored according to residue type: basic residues in blue, acidic in red, polar in green, and nonpolar in white.

Here we compare results from calculations using the GMO parameters to those of a POPC bilayer. Calculations were carried out to optimize the contact boundary curve for all 6 proteins in both membrane types and we present the total insertion energies in Table 2.3. We find that for the stiffer POPC membrane, our model is able to discriminate membrane proteins from aqueous proteins. The model predicts a positive transfer energy for inserting soluble proteins into the membrane, but the membrane protein energy values are all negative, indicating greater stability in the membrane. For the membrane proteins, since very little bending occurs (Figure 2.3), there is little difference in energy between the two membrane types. However, dramatic bending is observed in the case of the aqueous proteins. This extreme deformation occurs to expose the numerous charged and polar residues on the soluble protein surfaces to water. There is a large elastic penalty for such significant bending, however, and the insertion energy is therefore significantly increased with the stiff POPC membrane parameters.

We further explore in Section 3.3.5 and [37] how the stiffness of the bilayer can have a dramatic effect on the stability of peptides in the membrane. We show that an alpha helix can be stable in a membrane with elastic properties determined from flexible GMO membranes, yet unstable with a modest increase in membrane stiffness. In that case we held the bending modulus, K_c, constant and modified only the compression modulus, K_a, which is appropriate for an increased concentration in membrane-stiffening molecules such as cholesterol.

TABLE 2.3: Predicted insertion energy for flexible and stiff membranes

Protein (PDB ID)	**GMO** (kcal/mol)	**POPC*** (kcal/mol)
Chymotrypsin (4CHA)	-59.7	22.1
Insulin (4INS)	-21.7	14.9
GFP (1GFL)	-34.7	8.8
OmpA (1QJP)	-113.7	-110.9
VDAC (3EMN)	-170.2	-169.1
Bacteriorhodopsin (1M0L)	-296.2	-295.6

Both aqueous and membrane proteins are stable in the membrane when flexible GMO membrane properties are used. When elastic properties from stiffer POPC bilayers are used, the water soluble proteins are predicted to be marginally unstable in the membrane. Water soluble proteins are displayed in italics. The asterisk indicates the base parameter value used in other calculations when not specified.

2.3.2 Electrostatics: influence of protein dielectric

The use of the continuum Poisson-Boltzmann equation is used extensively throughout protein biophysics. However, there is a significant amount of debate over the appropriate dielectric value for the interior of the protein [41]. A dielectric range of 2 to 10 is often discussed as appropriate, though some work has shown this may be even higher [42]. It is certainly an approximation to assign a single value to the heterogeneous environment of the protein, and several studies indicate that the protein dielectric should actually vary throughout the protein [41]. This has led to several groups that have modeled a discretely varying dielectric in the protein, and others that have developed methods which allow for a dielectric gradient inside the protein [43]. It is also worth noting that different values have been suggested for different kinds of calculations such as pKa, solvation, or ligand binding. Following work by Sitkoff and co-workers, we have chosen a protein dielectric of 2 as our standard value [44].

We investigated the sensitivity of our model's predictions to the protein dielectric. We chose two water soluble proteins, chymotrypsin and insulin, and for these explored a range of protein dielectrics up to 10. For each dielectric value, we optimized the boundary conditions to identify the lowest energy membrane deformation. As we changed the protein dielectric, the standard model parameters (Table 2.1) with POPC membrane properties were left unchanged to isolate the influence of the modified dielectric. In Figure 2.4 we show that although both of these aqueous proteins are unstable in the membrane with our standard value of 2, our model predicts that chymotrypsin is stable in the membrane for protein dielectrics 8 and greater.

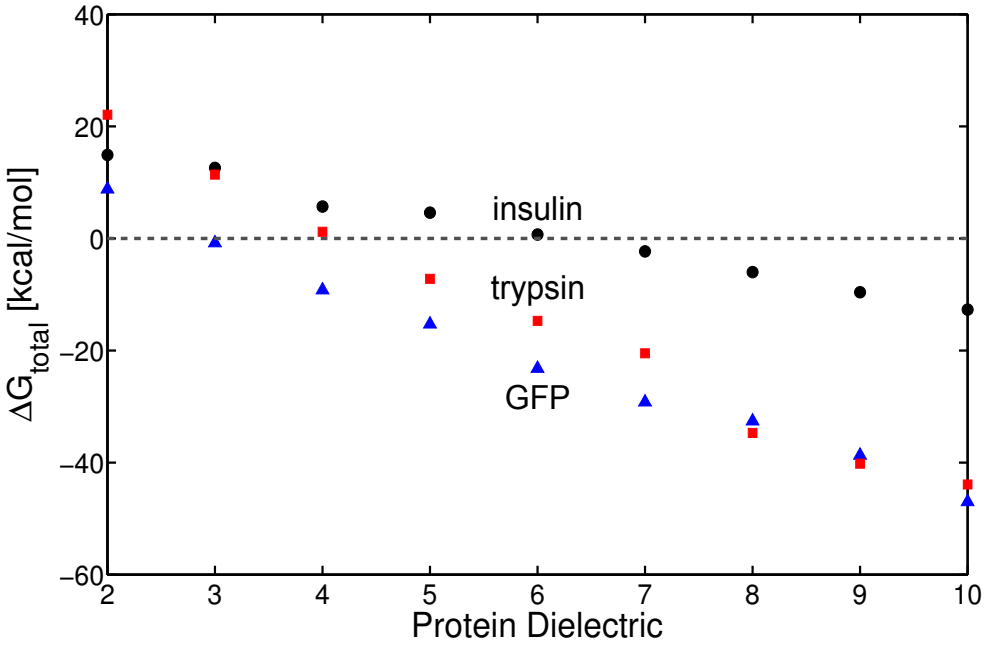

FIGURE 2.4: Increasing protein dielectric (ϵ_p) makes water soluble proteins stable in the membrane.

The search algorithm was carried out on the aqueous proteins insulin (black circles), trypsin (red squares), and GFP (blue triangles) for protein dielectrics from ranging 2 to 10. Insertion energy values decrease as ϵ_p increases. While none are stable using our standard value $\epsilon_p = 2$, all 3 proteins become stable in the membrane over this range. The values at $\epsilon_p = 2$ correspond to the energies reported in the asterisk marked columns in Tables 2.3, 2.4, and 2.5.

2.3.3 Electrostatics: influence of headgroup dielectric

The electrostatic energy is a dominant term when considering the total insertion energy of protein into the membrane. While the Poisson-Boltzmann equation is an accepted model for calculating this energy, there are assumptions that must be made regarding the dielectric value of the lipid environment and the protein. While many studies agree that the core of the membrane is best represented by a low dielectric of 1 to 2, there is some debate about how best to model the headgroup region [45].

We model the headgroup region separately from the core of the bilayer as an 8 Å thick region of dielectric 80 and counter-ion accessibility set to zero [27, 46]. Similar to the core of the membrane, protein atoms buried in this region are not considered solvent accessible. Together, these parameters create a region that is ideal for large residues such as tryptophan that have been shown to anchor proteins in the membrane. However, a headgroup dielectric of 80, the same as the solvent dielectric, may over-stabilize the insertion of charged moieties into this region. We therefore investigated the effect of decreasing the headgroup dielectric to 40 in our model (Table 2.4). As expected, all proteins were destabilized by the decrease in ϵ_{hg}. The membrane proteins remained very

TABLE 2.4: Decreasing headgroup dielectric decreases the stability of all proteins in the membrane

Protein (PDB ID)	$\epsilon_{hg} = 40$ (kcal/mol)	$\epsilon_{hg} = 80^*$ (kcal/mol)
Chymotrypsin (4CHA)	69.9	22.1
Insulin (4INS)	32.0	14.9
GFP (1GFL)	36.2	8.9
OmpA (1QJP)	-89.3	-110.9
VDAC (3EMN)	-145.2	-169.1
Bacteriorhodopsin (1M0L)	-252.0	-295.6

Water soluble proteins are displayed in italics. The asterisk indicates the base parameter value used in other calculations when not specified.

stable in the membrane, and the water soluble proteins became more clearly unstable in the membrane. Interestingly, the difference between the least stable membrane protein and the most stable aqueous protein was slightly increased by the decrease in headgroup dielectric.

2.3.4 Nonpolar models

A key aspect of our model is the nonpolar energy component, which can be quite large. Many studies have focused on this energy term for small molecules, e.g. [44, 47], and significant work has been done to achieve greater accuracy by including volume dispersion terms [48]. However this work has largely been focused on small molecules and peptides, and it is generally agreed that the area term dominates for large solute sizes [48, 49]. Very few studies have explored the nonpolar energy associated with moving large molecules, proteins, or protein complexes into the membrane.

We implemented a nonpolar solvation energy model based on the Positioning of Proteins in Membranes (PPM) model from Lomize and colleagues that takes the atom type into account when calculating the nonpolar energy [20]. The rationale for this heterogeneous treatment of the exposed surface area is that some atoms placed in water will disrupt the bulk water hydrogen bond network more than others. For example, carbon atoms are simply disruptive to the hydrogen bond network, while nitrogen atoms possess some propensity to form hydrogen bonds with water molecules. Under the PPM model, there is a positive nonpolar energy associated with moving a nitrogen atom into the membrane, and a negative energy for moving a carbon atom into the membrane. In contrast, the surface area of all atoms in our standard nonpolar model is considered equally disruptive. We therefore expect the PPM model to yield higher nonpolar energies. More details about the model and our implementation can be found in Section 2.2.3.

TABLE 2.5: Predicted insertion energies increase under an alternative nonpolar model

Protein (PDB ID)	**Standard nonpolar***	**PPM** [20]	**PPM,** $\epsilon_p = 10$
Chymotrypsin (4CHA)	22.1	186.3	172.8
Insulin (4INS)	14.9	91.3	79.0
GFP (1GFL)	8.8	138.2	105.8
OmpA (1QJP)	-110.9	15.4	-17.2
VDAC (3EMN)	-170.2	20.3	-29.0
Bacteriorhodopsin (1M0L)	-296.2	-23.2	-110.6

The atomic solvation parameter (PPM) method leads to higher insertion energies for all six proteins. Water soluble proteins are displayed in italics. All energies in kcal/mol. The asterisk indicates the base parameter used in all other calculations unless otherwise specified.

We carried out calculations using the PPM method as a replacement for our standard nonpolar method and found that the insertion energies for these proteins were all greater when using the PPM model (Table 2.5). While all of the aqueous proteins remained unstable in the membrane, two of the membrane proteins were also predicted to be unstable under the PPM model. Since we found in Section 2.3.2 that modest increases in protein dielectric can stabilize insertion (Fig. 2.4), we then performed a set of calculations in which we combined the PPM nonpolar method with a protein dielectric of 10. Under this combination, all of the membrane proteins were stable in the membrane, while none of the aqueous proteins were predicted to be stable. Interestingly, for all three methods, the insertion energies between the most stable aqueous protein (GFP) and the least stable membrane protein (OmpA) is within ∼3 kcal/mol. This highlights the importance of the absolute values of these insertion energies since the relative energies do not seem to vary between these three models.

2.4 Discussion

We applied our method to a set of three membrane proteins and three water soluble protein structures. Our model predicted that all membrane proteins are stable in the membrane while the aqueous proteins are not. The ability of our model to discriminate membrane proteins from soluble proteins is crucial as we extend our method to more controversial proteins in later chapters. There was a clear difference between the two sets of proteins we examined in this chapter. The transmembrane portions of the membrane proteins were dominated by nonpolar residues, while the entire surface of each aqueous proteins was covered with charged and polar amino acids. However, some proteins do not neatly fit into these categories. For instance, there are many membrane proteins that bear evolutionarily conserved charged and polar residues in their transmembrane

regions [3]. In particular, voltage-gated ion channels require charged residues in the TM segment to sense changes in membrane potential. While controversial, experiments and simulations show that even isolated voltage sensor segments can be stably accommodated in the membrane [8, 50]. In Chapter 3 we present complementary evidence that despite the presence of many charged residues, such proteins can be stable in the membrane.

In the future, particularly given the speed and computational efficiency of our method, we plan to apply our model to a much larger set of structures. While the primary aim of our model is to provide a detailed, microscopic picture of protein-membrane interactions, it would be interesting to determine the statistical accuracy of our model in a macroscopic context such as a large set of protein structures from the Protein Data Bank. Such analysis may be useful in identifying particular regimes under which our model performs poorly and regimes for which our model could be improved.

Chapter 3

Membrane bending is critical for the stability of voltage sensor segments in the membrane

While it is energetically prohibitive to bury charge in the hydrophobic core of the bilayer, the membrane is a flexible structure that can deform to accommodate such charge. In this chapter we present further details of our method for calculating the stability of solutes in the membrane based on elasticity theory and continuum electrostatics. The coupling of a search algorithm to our insertion energy calculations permits us to explore a range of biological phenomena that were beyond the scope of the original method developed in the Grabe lab [22]. We show that the energy required to embed charged residues in the membrane can be highly non-additive, and our model provides a simple mechanical explanation for this non-additivity. In addition we predict that a controversial class of peptides, voltage sensor segments of voltage-gated potassium channels, can stably insert into a deformable membrane. We also use the model to investigate hydrophobic mismatch in a large mechanosensitive channel. [1]

[1] This chapter is adapted from: K M Callenberg, N R Latorraca, and M Grabe. Membrane bending is critical for the stability of voltage sensor segments in the membrane. Journal of General Physiology, 140(1):5568, 2012 [37].

3.1 Introduction

The membrane serves as a barrier between the interior of a cell and its environment, allowing the cell to retain essential components and control its internal chemistry. The primary constituents of the membrane are amphipathic lipids composed of a polar headgroup that faces solution and a hydrophobic tail that forms a low-dielectric barrier preventing ions and molecules from penetrating the membrane [51]. Much of the communication and exchange of material between the inside and outside of the cell is mediated by embedded membrane proteins that enable a variety of biological phenomena from small molecule and ion transport to cell signaling. The transmembrane (TM) spanning regions of membrane proteins are characteristically made up of hydrophobic amino acids, which are energetically compatible with the hydrophobic environment of the membrane core. However, charged residues within the TM domains of a variety of proteins present an electrostatically challenging situation to stable inclusion in the membrane. For example, voltage-sensor domains of voltage-dependent ion channels contain charged arginines and lysines in the membrane-spanning S4 segment that make it possible for the protein to respond to electric fields [52–55]. A classic study of the thermodynamic properties of amino acid analogs suggests that it requires 65-80 kcal/mol of energy for charged residues to enter organic phases from water [5], and numerical calculations support these high energies [44]. Various models have been proposed to explain how voltage-dependent proteins are able to stably accommodate charged residues in the hydrophobic span of the bilayer. For instance, the S4 segment may be positioned within a canaliculus of the protein where it avoids interaction with the bilayer core and makes charge pairs with other regions of the protein [56–61]. Yet electron paramagnetic resonance (EPR) experiments on KvAP suggest that some portions of the S4 segment directly interact with lipid, while other portions are protected from the lipid [62]. Additionally, biotin-avidin accessibility experiments on the KvAP S4 segment suggest even more extensive interactions of S4 with the lipid [63]. Studies have also attempted to explain the stability of these charged segments in terms of lipid composition [64, 65], but it is still unclear to what extent charged voltage sensor segments are exposed to lipid and whether they are truly stable in any lipidic environment.

Recent translocon [6, 66] and porin folding [67] based experiments have presented data in which charged residues only destabilize a membrane protein by a few kcal/mol. In light of these results, it is not surprising that voltage-dependent membrane proteins harbor charged residues in the membrane-spanning region, but how do we reconcile these low insertion energies with the large values derived from bulk partitioning experiments [5]? Molecular dynamics (MD) simulations suggest that membrane bending helps stabilize charges in the membrane by allowing water access to the buried amino acid [9, 68,

69]. This is in accord with experiment and MD simulation on the voltage sensor from KvAP (segments S1-S4) showing that the bilayer thins in the presence of the voltage sensor and that the voltage sensor is significantly hydrated in the membrane [70]. Based on such observations, we developed a solvation model for protein insertion into the membrane that treats the membrane as a deformable continuum [22], similar to classic studies by Helfrich and others [14, 16, 18], but we couple membrane bending to protein electrostatics and hydrophobic forces in an analogous manner to theoretical treatments of small molecule solvation [71, 72]. Interestingly, both MD simulations [9, 69] and our continuum based molecular calculations [22] predict significantly larger destabilization energies, on the order of 10-18 kcal/mol, than those predicted by the translocon and porin folding scales. Nonetheless, these values are much smaller than those based on bulk experiments [5, 44] due to bilayer deformations in the presence of buried charged amino acids that expose charged groups to water and polar lipid headgroups [9, 68, 69]. Previously, we predicted the energetics of charged TM segments by using linear elasticity theory to allow for membrane bending, and our results clearly showed that these distortions facilitate favorable electrostatic interactions between charged protein moieties and solvent and polar headgroups at a minimal cost to the membrane bending energy [22]. However, our method was severely limited by the ability to only allow distortions in the upper leaflet and the need to posit a priori the boundary curve of the protein-membrane interface using pre-determined geometries. For simple protein sequences harboring a single charged residue, we show here that we made good guesses to the contact curve in our original study, but for more complex peptide sequences a systematic approach must be adopted. We have therefore expanded our previous work by introducing a search on the inner boundary curve of the protein-membrane interface to find optimal distortions in the membrane. Additionally, we now allow both the upper and lower leaflets to deform.

These extensions to our original model have allowed us to probe several phenomena central to membrane biophysics. Our method successfully identifies the TM segment of a membrane protein, and it predicts the vertical position of the protein within the membrane that minimizes the total insertion energy. Unlike other continuum membrane models, our method allows for large membrane deformations that cover hydrophobic stretches of the TM protein and dramatically reduces the system energy. We explore the influence of varying the membrane thickness on the stability of the mechanosensitive channel MscL, and we predict a degree of water accessibility that is in good agreement with experiment. We show that insertion energy values are not additive, in particular when considering the insertion of multiple charged residues into the TM region. Finally, our method predicts that the S4 segments of voltage-dependent potassium channels are stable in the membrane, and we calculate stability values and membrane distortions

that are in semi-quantitative agreement with fully atomistic and coarse-grained MD simulations; however, we show that stability values can vary greatly depending on the material properties of the bilayer. In the Discussion, we suggest additional areas of biology to which we could apply our method as well as current limitations and future changes to the algorithm.

3.2 Materials and Methods

3.2.1 Theory

As in our previous work [22], we assume that membrane protein stability is dominated by three energetic components: membrane bending, G_{mem}; electrostatics, G_{elec}; and nonpolar interactions between the protein and water, G_{np}. All free energy changes are calculated by comparing the energy of the protein in a reference state completely in solution, far from an unstressed membrane with the energy of the protein embedded in the membrane. Hence, G_{mem} is zero for the reference state. We assume that the protein structure is the same in the reference state and the membrane-embedded state. Membrane protein stability is then given by the difference in the total energy of the protein in solution compared to the energy in the environment of the membrane:

$$\Delta G_{total} = \Delta G_{mem} + \Delta G_{elec} + \Delta G_{np} \tag{3.1}$$

All three energy terms on the right hand side of Eq. 1 are coupled in a complex manner through the shape of the membrane. As the membrane shape is changed, this influences the electrostatic energy of the system and the nonpolar energy by altering the amount of protein surface exposed to water. These second two energy terms drive changes in the shape of the membrane as our search algorithm, described below, minimizes G_{total}. The shape and energy of the membrane are determined using linear elasticity theory, in which each leaflet is described by a thin surface, u(x,y), illustrated in Fig. 3.1, with material properties that can be tuned to the membrane of interest. The total membrane bending energy is given by:

$$\begin{aligned}\Delta G_{mem} = \frac{1}{2}\int_{\Omega} &\frac{K_a}{L_0^2}(u^- - u^+)^2 + \dots \\ &\frac{K_c}{2}\left((\nabla^2 u^-)^2 + (\nabla^2 u^+)^2\right) + \dots \\ &\frac{\alpha}{2}\left((\nabla u^-)^2 + (\nabla u^+)^2\right) d\Omega,\end{aligned} \tag{3.2}$$

where u^+ is the shape of the upper leaflet and u^- is the shape of the lower leaflet; L_0 is the equilibrium length of the membrane, K_c is the membrane bending energy, α is the surface tension, and K_a is the compression modulus. The energy of the upper and lower leaflets are coupled through the compression modulus. The functional derivative of Eq. 2 with respect to variations in u^+ and u^- gives the partial differential equation (PDE) that determines the shapes of each leaflet. Assuming the opposite leaflet is flat, each surface obeys the following PDE:

$$\nabla^4 u - \gamma \nabla^2 u + \beta u = 0, \tag{3.3}$$

where $\gamma = \alpha/K_c$ and $\beta = 2K_a/(L_0^2 K_c)$. We solve this equation separately for u^+(x,y) and u^-(x,y) applying height and contact angle boundary conditions at the membrane-protein interface as described below and shown in Fig. 3.1B, and far from the protein, we assume that the membrane is asymptotically flat at its equilibrium length, L_0. After solving for u^+(x,y) and u^-(x,y), the total membrane energy is determined by carrying out the integral in Eq. 2. We have investigated the error associated with assuming the upper leaflet is uncoupled from the lower leaflet during the solution step, and for the class of problems examined here, the absolute error in the total energy is less than 0.5 kcal/mol (data not shown).

The electrostatic energy component is calculated with Poisson-Boltzmann electrostatics, and the nonpolar contribution is calculated from the solvent accessible surface area (SASA). Both of these methods take into account all of the atomic detail of the protein, and therefore, a PDB file, or equivalent file, is required to carry out these calculations. To compute the SASA, the rough surface of the protein is computed by running a water probe of 1.4 Å over the van der Waals surface created by the union of all atomic van der Waals surfaces for the individual atoms in the protein using the Shrake-Rupley algorithm [32]. In the presence of the membrane, we carefully keep track of which protein atoms are embedded in the membrane, and modify the SASA accordingly. Following standard convention, we ignore hydrogen atoms when calculating the SASA. To compute the electrostatic energy, we use the software APBS [73]. The protein is treated in atomic detail, and the atomic partial charges are set using the PARSE parameter set, which was parameterized to reproduce solvation transfer free energies for small molecules [31]. The protein-water interface is determined using the protein molecular surface, which is calculated by running a 1.4 Å water probe over the van der Waals radii of the protein atoms as discussed above. The dielectric value of points inside the protein were set to 2.0, in accord with the PARSE parameterization [31], and values in water were set to 80.0. In the presence of the membrane, the membrane shape determined by u^+(x,y) and u(x,y) is used to modify the local dielectric environment of the protein, and points

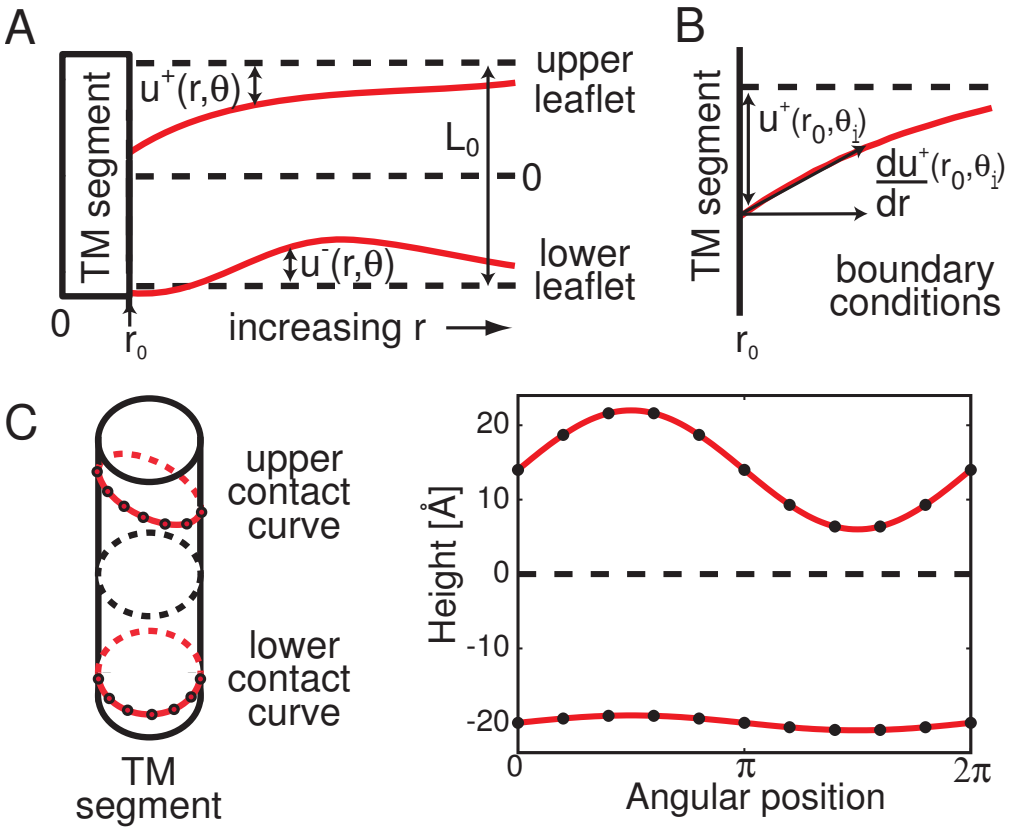

FIGURE 3.1: Geometry of the system.

A) Cross section showing membrane distortions in the upper and lower leaflets. Solid red lines indicate the membrane-water interfaces. Dashed black lines indicate the equilibrium heights of the membrane leaflets and the midplane at z=0. The equilibrium bilayer thickness is L0. B) The protein-membrane contact angle is proportional to the height deviation from equilibrium. C) The idealized helix is shown in a 3-D representation with red curves indicating the height of the upper and lower leaflets as they contact the TM segment. Black nodes on these curves are used as the boundary conditions for solving the elasticity equation. The numeric values of these nodes are optimized by the search algorithm. 2-D representation of upper and lower contact curves are shown on the right.

in the membrane are given a low dielectric value of 2.0 if in the core and 80.0 if in the headgroup region. The electrostatic energy difference for insertion, ΔG_{elec}, is then computed by subtracting the total electrostatic energy of the protein in pure solution from the value computed in the presence of the membrane. These energy terms are described in further detail in the appendix as well as in our previous work [22].

3.2.2 Construction of Transmembrane Segments

Alpha-helical peptides were constructed with the VMD plugin Molefacture version 1.1 [74]. We used SCWRL 4 [75] to optimize side-chain rotamer conformations, and MODELLER 9v8 [76] to orient the principal axes of the helix to the z-axis, perpendicular

to the plane of the membrane. The structures were converted to PQR format using PDB2PQR 1.4 [34, 35] with the PARSE radii parameter set [44]. To be consistent with most biochemical experiments, the WALP23 peptide was constructed with neutral N and C-termini in PDB2PQR by turning on the neutraln and neutralc flags. All other helical segments contained charged N and C-termini.

3.2.3 Search Algorithm for Identifying Optimal Boundary Conditions

We implemented a workflow illustrated in Fig. 3.2 to identify the shape of the membrane that minimizes the total energy in Eq. 1. For each cycle, we started with a given discretized contact boundary curve for the upper leaflet and the lower leaflet as shown in Fig. 3.1C. We solved Eq. 3 once for each leaflet with the height boundary conditions imposed by the posited boundary curve. The imposed contact angle that the membrane makes at the protein surface was treated differently for each of the problems investigated below. For the WALP peptide, we assumed a contact angle of zero, and for the MscL channel, we assumed that the contact angle was linearly proportional to the displacement from equilibrium with a coefficient of 1. For the voltage sensor helices, we carried out contact angle searches to minimizes the total energy. The solution surfaces were then provided to Eq. 2 to calculate the elastostatic energy.

The membrane shape was used to create dielectric and ion-accessibility maps which were subsequently read into the Adaptive Poisson-Boltzmann Solver (APBS) version 1.2 software package to calculate the total electrostatic energy [73]. After calculating the total energy for a given membrane shape, it was used as a cost function in a Powell's-based search [36] to generate a new boundary curve for the next cycle of the flowchart. Powell's is a conjugate gradient-based method and is particularly suited to this problem since it operates well on many dimensions and does not require the calculation of derivatives. We ended a search when the relative error was less than a small tolerance value of $5 \times 10^{-}3$, following the typical stop condition for Powell's method. In our original implementation, each boundary curve was discretized in θ, the angle around the cylindrical TM protein, and the search was carried out by vertically moving nodes on the boundary curve. However, since the displacement of adjacent points was uncorrelated, the search produced high curvature kinks in the membrane that hindered the ability to identify global minima. Therefore, we used a Fourier representation of the contact boundary:

$$u(r_0, \theta_i) = a_0 + \sum_{n=1}^{4}((a_n sin(n\theta_i) + a_{n+4} cos(n\theta_i)), \tag{3.4}$$

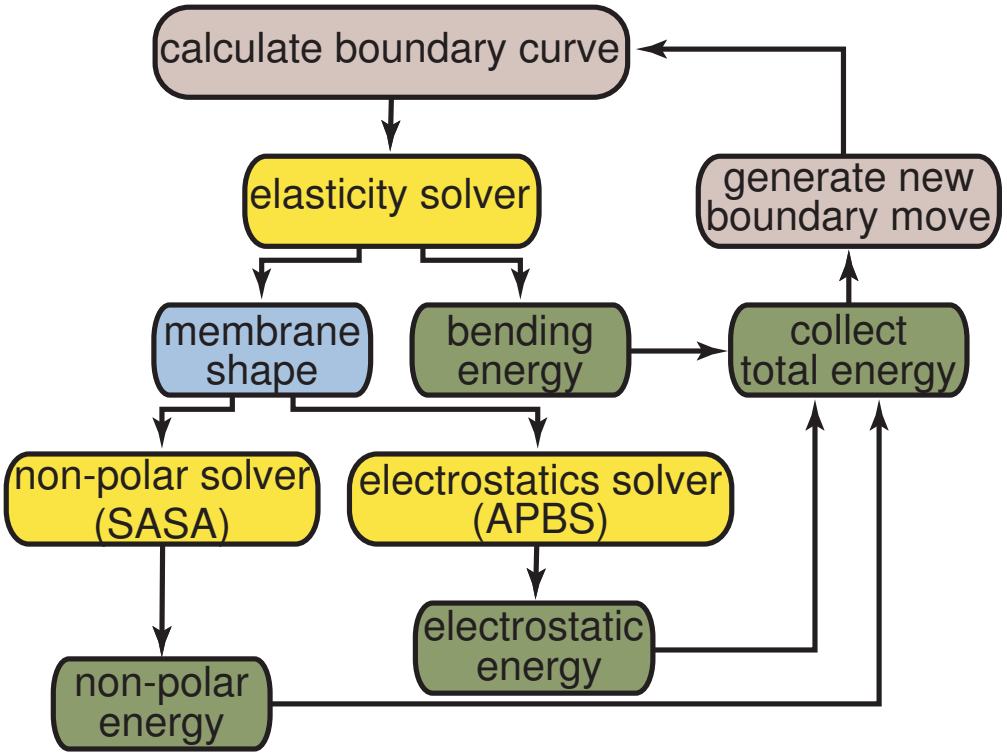

FIGURE 3.2: Algorithm for identifying the membrane shape with the lowest insertion energy.

Gray boxes represent decision steps, yellow boxes denote numerical calculation steps, the blue box denotes an intermediate product, and the green boxes represent resulting energies. The algorithm begins with either a flat membrane or an initial guess and proceeds until the total energy has been minimized.

where a_0 is a constant offset, a_n is the amplitude of the nth mode, r_0 is the radius of the TM protein and θ_i is the angular position discretized with 10 points along the membrane-protein boundary. We determined that including terms above n=4 did not improve the minimum energy configuration; however, it did increase the search space and number of iterations required to find the minimum. For n=4, the search space is 8 + 1 for the upper leaflet and 8 + 1 for the lower leaflet for a total dimension of 18.

3.3 Results

3.3.1 Our Model Captures Large-scale Membrane Rearrangements

Integral membrane proteins are characterized by stretches of hydrophobic residues that are well suited for incorporation into the low-dielectric core of the membrane. The chemical nature of these regions is important for the initial targeting of the chain to the membrane from the translocon and for the ultimate stability of the protein in the lipidic

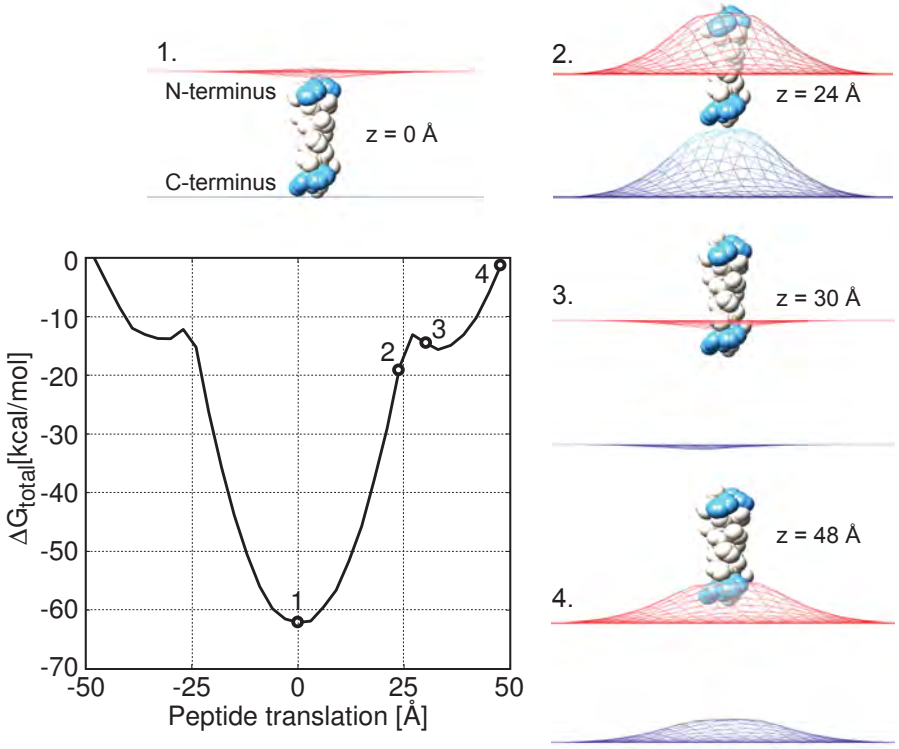

FIGURE 3.3: Translation of a hydrophobic WALP peptide across the membrane.

The COM of the peptide was initially placed at the center of the membrane at position 1, which is 60 kcal/mol more stable than the reference state in pure water. The minimized system geometry for each numbered item on the energy curve is shown around the graph. The hydrophobic residues are white, the flanking tryptophan residues are cyan, and the upper and lower membrane-water surfaces are the red and blue meshes, respectively. The protein was translated in the positive and negative directions in 3 Å steps, and a minimization was carried out in each case using the membrane shape from the previous step as the initial guess. At position 2, the membrane undergoes considerable deflection to continue to cover the hydrophobic residues of the protein. At position 3, the elastic energy penalty outweighs the nonpolar energy benefit of fully covering the peptide and a snap-through occurs. Finally, position 4 shows that there is a slight energetic advantage to bending the membrane to bury the terminal tryptophan residues in the interfacial headgroup region.

environment. However, the boundaries of TM segments are often poorly delineated since these stretches usually contain a few polar or charged residues. Therefore, it is important when modeling these systems to consider that the membrane-protein boundary is likely to have a complex shape that covers hydrophobic residues while exposing polar and charged residues to water. Moreover, the hydrophobic nature of the TM protein can induce large-scale conformational rearrangements in the bilayer when anchored to cytoskeletal elements or proteins attached to apposing membranes. For instance, SNARE, BAR, ESCRT-III and coat proteins all cause significant deformations in the membrane [77–81].

Most methods for identifying optimal protein placement and stability in the membrane

assume that the membrane is static, ignoring its dynamic and flexible nature [2, 21, 82]. In principle, our method not only captures small deformations of the membrane that occur around buried charged residues, but it also allows for large-scale, low energy conformations that may occur when an embedded protein is under load due to attachment to the cytoskeleton, for instance. To test our ability to identify such large distortions, we solved for the membrane shape that maximizes the stability of a WALP23 peptide (sequence GWWLALALALALALALALALWWA). WALPs are ideal for exploring membrane-protein interactions since their midsection has a strong hydrophobic signature and flanking tryptophan residues anchor the protein in the membrane by partitioning into the headgroup-water interface [83, 84].

We translated the peptide from one side of the membrane to the other, moving the center of mass (COM) from -48 to +48 Å in 3 Å steps. At each position, we used the search algorithm outlined in Fig. 3.2 to determine the optimal membrane configuration and corresponding energy as shown in Fig. 3.3. All energy differences are computed with respect to the reference state in which the membrane protein is free in solution far from an unperturbed membrane. The system energy takes on a minimum value of ∼-60 kcal/mol when the peptide COM coincides with the middle of the bilayer at z=0. In this configuration, inset 1 shows that there is no hydrophobic mismatch since the membrane is flat, yet the hydrophobic residues (white) are maximally embedded in the membrane and the tryptophan residues (cyan) are in the headgroup region. When the peptide is moved to +24 Å (inset 2), the total energy increases because the membrane bends to cover the hydrophobic residues. At +30 Å , the membrane bending energy becomes larger than the hydrophobic energy required to uncover the TM, and the bilayer exhibits a snap-through instability that extracts the TM (panel 3 in Fig. 3.3). Our analysis shows that our search algorithm can successfully identify large-scale deflections in the membrane that bring about drastic reductions in the total energy of the system.

3.3.2 Predicting Optimal Membrane Thickness for a Mechanosensitive Channel

Even when the hydrophobic domain of a membrane protein is clearly delineated, mismatch between the length of the hydrophobic stretch and the equilibrium length of the membrane can lead to bilayer distortions and an increase in the energy of the system, and conversely, mismatch can lead to distortions in the protein [85, 86]. X-ray lamellar diffraction studies show that the membrane expands or compresses at the edge of the protein to accommodate for hydrophobic mismatch [87], and mismatch has been shown to cause proteins to segregate to specific locations in the cell [88]. Changes in membrane thickness have also been shown to influence the functional state of membrane

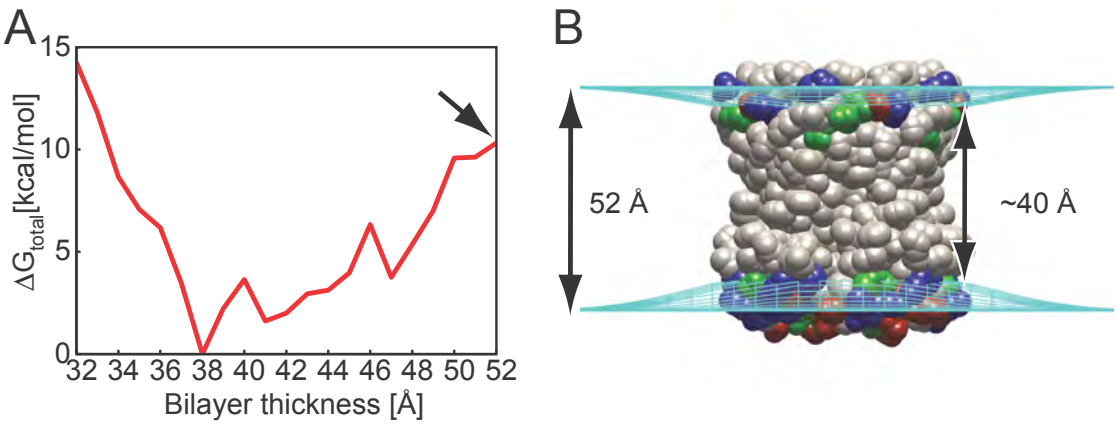

FIGURE 3.4: Optimization of membrane thickness for a mechanosensitive channel.

A) We swept through a range of equilibrium membrane thickness values in 1 Å steps, and for each value, we identified the membrane shape that optimizes the total insertion energy for the closed state structure of the mechanosensitive channel of large conductance (MscL, PDBID: 2OAR). The system is most stable at a 38 Å thickness for our choice of membrane parameters. The stabilization energy increases by more than 10 kcal/mol when the membrane thickness is reduced by 6 Å, and it increases to about 10 kcal/mol in a membrane that is 14 Å thicker. The energy is more sensitive to decreases in the equilibrium membrane thickness than increases in the thickness. B) The membrane thins at the edge of the channel to expose regions of polar (green), basic (blue) and acidic (red) residues when its thickness is greater than the optimal value of 38 Å. To exemplify this situation, we embedded MscL in a non-ideal membrane with an equilibrium length of 52 Å. The membrane shape (cyan mesh) that minimizes the insertion energy highlights the thinning that occurs at the protein-membrane boundary. The energy of this situation is indicated by the arrow in panel A.

proteins such as mechanosensitive channels and voltage-gated ion channels [89]. The mechanosensitive channel of large conductance (MscL) is a homomeric pentamer that is thought to open and close like the aperture of a camera [90]. The application of membrane tension biases the channel from a closed state, in which the TM α-helices are primarily perpendicular to the plane of the membrane, to an expanded, open state, in which the helices are significantly tilted. This tilt decreases the hydrophobic length of the membrane spanning region in the open state with respect to the closed state. Perozo and co-workers hypothesized that this structural change in the channel should lead to greater stabilization of the open state in thinner membranes compared to thicker membranes, and they verified their claim by showing that the channel open probability increased as the bilayer thickness decreased at a fixed pressure [91].

We used our model to determine the membrane thickness that optimally stabilizes the closed state of the MscL structure from M. tuberculosis [92]. We removed the cytoplasmic helices and embedded the TM domain in the bilayer. We then used our search algorithm to determine the optimal membrane contact curve and total insertion energy for a given membrane thickness as shown in Fig. 3.4B. Next, we varied the equilibrium membrane length over the range of values suggested by the experiments

carried out by Perozo and colleagues and plotted the energy values with respect to the minimum value (Fig. 3.4A). The channel is stable in the membrane over the entire range with the optimal thickness being 38 Å. For values larger than 38 Å, the membrane thins as it approaches the channel surface. The OPM method predicts an optimal thickness that is several ngstroms larger than our method [21]; however, our value is in better agreement with fluorescence spectroscopy studies showing that the hydrophobic thickness of the bilayer is 25 Å [93]; ignoring the headgroup region, we predict a thickness of 24 Å. Previous low resolution models have been used to calculate the influence of membrane thickness on the open probability of the channel [94], but this is not possible with our method since the structure of MscL in the open state is unknown.

3.3.3 Amino Acid Insertion Energies Are Not Additive

Hydrophobicity scales provide a straightforward means for assessing the stability of transmembrane proteins by adding up the individual energetic contribution from each amino acid in the transmembrane domain to determine the overall stability. However, insertion energy scales based on in vitro translation and insertion via the Sec61 translocon suggest that the apparent transfer free energy for an amino acid depends on the amino acid sequence of the transmembrane segment [66]. Thus, it is possible that amino acid insertion energy values are not additive, which would severely limit the value of any hydrophobicity scale.

Based on molecular simulations [9, 69], non-additivity has been suggested to arise because there is no additional membrane bending energy to insert a second or third charged residue after the membrane has bent to expose the first charged residue. To further examine this hypothesis, we constructed α-helical peptides containing zero to three charged residues and probed their stability in the membrane. We find that the energetic cost of inserting each additional charged amino acid is significantly less than that of inserting the first (Table 3.1). While a peptide with a single central arginine is 10 kcal/mol less stable than one with alanine, the addition of a second arginine requires only 1 additional kcal/mol, and a third requires only an additional 2 kcal/mol. These low energies support results from recent MD simulations which found that there is essentially no additional energetic cost required to insert an arginine once the first has already formed a water defect [95]. Experimental support for non-additivity comes from membrane protein folding experiments, which show that the cost to insert two charged residues is less than twice the sum of inserting a single charged residue [67]. Nonetheless, we predict cooperativity values of 9 kcal/mol for inserting two arginines, while the predicted cooperativity based on the porin folding studies is only 1.6 kcal/mol [67]. These energy values are highly dependent on system geometry, and it may be

TABLE 3.1: The insertion energy of charged residues is not additive.

Peptide sequence	ΔG_{total} (kcal/mol)
...NNKKAAAAAAAAAAAAAAAAAAAKKNN...	-49.5
...NNKKAAAAAAAAA**R**AAAAAAAAAKKNN...	-39.4
...NNKKAAAAAAAA**RR**AAAAAAAAAKKNN...	-37.6
...NNKKAAAAAAA**R**A**R**AAAAAAAAAKKNN...	-36.2
...NNKKAAAAAA**R**AA**R**AAAAAAAAAKKNN... *	-38.5
...NNKKAAAAAAA**RRR**AAAAAAAAAKKNN...	-33.2
...NNKKAAAAA**R**A**R**A**R**AAAAAAAAAKKNN...	-32.6
...NNKKAAA**R**AA**R**AA**R**AAAAAAAAAKKNN... **	-37.6

Peptides were constructed with the sequences listed below flanked by 12 glycine residues. A helix with a single arginine at the center of the membrane is10 kcal/mol less stable than one with an alanine, but the addition of a second arginine makes the peptide only 1 kcal/mol less stable since the membrane has already bent to expose the central arginine. Further, the cost of including a third charged arginine is similarly an additional 1 kcal/mol. Helices with arginines spaced 2 apart (RXXR) are more stable than those with no spacing or single spacing since the membrane must only bend on one side of the helix to expose the residues to water. This incurs minimal elastic and nonpolar penalties. Helices indicated by * and ** were also created as 3_{10} helices, and their energy values are discussed in the main text.

difficult to compare values obtained for a single pass α-helix with those obtained from a beta barrel. Our results highlight the non-additivity inherent in this system and suggest that a simple hydrophobicity scale may lead to incorrect conclusions, especially when considering highly charged proteins or peptides.

While our method captures the non-additivity inherent in these systems, we wanted to compare our calculations to Generalized Born models for electrostatics in the presence of the membrane, which do not account for changes in membrane geometry [2, 21, 82]. To make a proper comparison with these models, we extracted the electrostatic component of the insertion energy for helices containing 0 to 3 arginines from Table 3.1 and reported these values in Table 3.2. Energy values are reported as $\Delta\Delta G_n = \Delta G_n - \Delta G_{n-1}$, such that the value represents the energy required to insert one more charged residue into the TM helix. Even the electrostatic component of the energy alone from our model is highly non-additive; however, the energy values calculated using the model of Im and co-workers is quite linear [2, 96], indicating that subsequent arginines are as costly to insert as the first. Additionally, the electrostatic component of the energy for inserting even a single charged residue is 25-30 kcal/mol greater than that predicted with our model. For charged membrane proteins and membrane-associated proteins, Generalized Born models that treat the membrane dielectric as a uniform slab could give rise to incorrect results. However, for proteins that are not highly charged such methods may be sufficient.

TABLE 3.2: Comparison of insertion energy values between our method and a Generalized Born method [2].

Peptide sequence	This study	GB
...NNKKAAAAAAAAAAAAAAAAAAAKKNN...	0.0	0.0
...NNKKAAAAAAAAA**R**AAAAAAAAAKKNN...	-4.7	26.3
...NNKKAAAAAAAA**RR**AAAAAAAAAKKNN...	3.3	28.0
...NNKKAAAAAAA**RRR**AAAAAAAAAKKNN...	0.7	22.9

The electrostatic energy for the four sequences on the left were computed using both methods. Reported energy values are the difference between the current sequence and the R-1 containing helix, with the alanine sequence being set to zero. All energy values are in kcal/mol. While our method allows the membrane to bend to expose charged arginines, the Generalized Born method treats the membrane as a flat slab with a dielectric that smoothly switches from membrane to solvent. Thus, the Generalized Born method predicts an electrostatic cost that is nearly equal for each additional arginine, while our method does not exhibit additivity.

3.3.4 Some Voltage Sensor Segments Are Stable In the Membrane

Voltage-gated potassium [52], sodium [97] and proton channels [98, 99] as well as voltage-gated phosphatases [100] all contain 4-7 charged residues in their 4th TM segment critical for their ability to sense changes in the membrane potential. How such highly charged segments stably incorporate into the membrane is an outstanding question in membrane biophysics, and many researchers believe that other TM segments are required for incorporation [57, 101]. In contrast, both experiment [50] and simulations [68, 102] suggest that some S4 segments favorably adopt a transmembrane configuration.

In order to further explore these controversial results, we performed calculations on idealized helices with sequences corresponding to the S4 segments from the Kv1.2 Shaker-like potassium channel from rat and the KvAP archaebacterial channel. Note that the sequence of Kv1.2's S4 segment is identical to Shaker. In the absence of membrane bending, both helical segments are highly unstable in the membrane with transfer free energies of +72 kcal/mol and +99 kcal/mol for Kv1.2 and KvAP, respectively. Remarkably, when we allow the membrane to bend, our model predicts that both segments are quite stable in the membrane with the S4 from Kv1.2 stabilized by -31 kcal/mol and the segment from KvAP stabilized by -33 kcal/mol (Fig. 3.5). This drastic reduction in energy is brought about by relatively modest distortions in the membrane as can be seen from the minimum energy configurations also pictured in the figure. It is not surprising that the S4 segment from KvAP is 2 kcal/mol more stable than the Kv1.2 segment since it has only 5 positive charges while Kv1.2 has 6 charges.

With any new approach, it is useful to have a benchmark with which to validate the model. Fully atomistic MD simulations are the gold standard in this case, but detailed

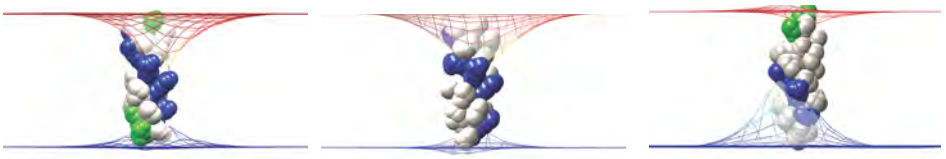

	Kv1.2	KvAP	KAT1
	SLAILRVIRLVRVFRIFKLSRHS	GLGLFRLVRLLRFLRILLIISRG	LGFRILSMLRLWRLRRVSSLFAR
no bending	+72 kcal/mol	+99	+99
bending	-31	-33	-24
coarse-grained*	-36	-38	NA
Gromos96*	-45	NA	NA

FIGURE 3.5: Membrane bending stabilizes the insertion of voltage sensor S4 segments in the membrane.

The search algorithm was carried out on S4 segments from KvAP, Kv1.2 and KAT1, and the final membrane shapes are pictured. Peptide insertion is highly unstable when no membrane bending is allowed, but considerably improved when the membrane bends to expose charged and polar amino acids. Our insertion energies for Kv1.2 and KvAP are similar to values from coarse-grained simulations (values indicated by * were taken from [102]). Experiments have suggested that isolated S4 segments of KAT1 will not readily insert [103], and while our method finds a negative insertion energy for the KAT1 S4, it is more difficult to insert than Kv1.2 and KvAP for which experiments show isolated insertion.

free energy calculations, even on a single pass TM, in the presence of a membrane are extremely demanding, and there is a large potential for sampling error. Fortunately, the Sansom group has carried out free energy calculations on both of these S4 segments using a more tractable, coarse-grained model of the system [104]. They report insertion energy values of -36 kcal/mol and -38 kcal/mol for the Kv1.2 and KvAP S4 segments, respectively [102], which is in strikingly good agreement with our absolute values as well as our predicted relative stability between both voltage-sensor segments. The Sansom group used their coarse-grained model results as a starting point to carry out fully atomistic free energy calculations on the Kv1.2 S4 segment using the GROMOS96 forcefield [102]. This resulted in a minimum energy configuration that was -45 kcal/mol more stable than the segment in water, which is 9 kcal/mol lower than the coarse-grained model results and 14 kcal/mol more stable than our results [102]. Thus, while the membrane deformations and energies in our model are similar to the deformations from coarse-grained and fully atomistic simulations, our predicted energy values are slightly higher. While there are differences in the three energy potentials that may account for these discrepancies, we believe that the most obvious deficiencies in our model are the lack of protein tilt and side chain reorientation. Adding these two additional degrees of freedom will reduce the minimum energies that our model will produce, and hopefully bring our values into closer absolute agreement with other calculations. Additionally, as explored below, the material properties of the bilayer can significantly impact the insertion energy of the helix, and it is not clear what the bilayer parameters in our model

should be to most closely approximate the properties of the coarse-grained membrane.

It is thought that the RXXR spacing of residues in many S4 segments is important to their stability. To examine this, we created 18 mutated Kv1.2 sequences preserving the total charge but disrupting the spacing, and we found every mutation led to a higher insertion energy value. Interestingly, the S4 segment from the hyperpolarization-activated potassium channel KAT1 has an unconventional charge spacing with two adjacent arginines, and there is experimental evidence that this segment will not insert into the membrane when isolated from the rest of the channel [103]. We applied our model to the KAT1 S4 segment and observed a stabilizing transfer free energy of only -24 kcal/mol, which is 7 kcal/mol less stable than either the Kv1.2 or KvAP S4 segments. Therefore, we believe that this lower insertion energy may be related to the charge spacing on KAT1; however, our results still predict that the S4 from KAT1 should be stable in the membrane which is at odds with the finding that the S3 segment is also required for membrane stabilization [103]. To specifically explore the importance of charge spacing, we systematically varied this spacing and measured the stability of single pass TM segments. Our results suggest that charged residues spaced two apart, for example RXXR, are 2-4 kcal/mol more stable than those spaced by zero or one uncharged residues (Table 3.1). Visualization of the minimum energy configuration for each case shows that the membrane need only bend on one side of the helix to expose charged residues separated by two intervening nonpolar residues, while the membrane undergoes much more extensive distortions to expose charged residues with different spacings (data not shown).

Recent, X-ray structures of voltage-gated ion channels suggest that the S4 helix exists, at least partially, in a 3_{10} helix rather than an ideal α-helix [105–107]. The 3_{10} configuration places all the charges with an RXXR spacing on one face, which localizes the membrane bending to one side of the helix and may reduce the bending energy. We explored this possibility by creating 3_{10} helices of the two sequences in Table 3.1 that have RXXR motifs, one harbors 2 arginines (indicated by * in the table) and the second harbors 3 arginines (indicated by ** in the table). The insertion energy values are higher when these sequences adopt a 3_{10} conformation versus an α-helical conformation by +5.3 kcal/mol (sequence with 2 arginine) and +5.1 kcal/mol (sequence with 3 arginine). Our calculations indicate that the α-helix configuration is slightly more stable due to an increased nonpolar stabilization; the α-helix is more compact and buries more surface area in the membrane. Thus, we believe that the propensity for portions of the S4 helix to adopt a 3_{10} configuration may be determined by local interactions with the rest of the channel rather than energetic interactions with the lipid membrane.

In our previous manuscript, we showed that the membrane dipole only moderately influenced membrane protein stability since the majority of the amino acids between the upper and lower leaflets were hydrophobic and therefore neutral [22]. However, this was the case for helices harboring a single charged residue, and it is possible that with many basic residues more charge becomes buried between the leaflets and experiences the significant positive electrostatic potential created by the lipid headgroups. To explore this scenario, we added a thin layer of positive and negative charge to the upper and lower leaflets with the negative layer closer to the membrane-water interface as described in our previous work [22]. The net charge sums to zero, and the separation length and charge values were chosen to create an interior membrane potential of +300 mV, which is near the peak dipole potential value of +260 mV measured for phosphatidylcholine headgroups with ester linkages to the tail [108]. For the configurations pictured in Fig. 3.5, the dipole potential destabilizes the TM helix by 2.6, 2.3, and 1.6 kcal/mol for the KvAP, Kv1.2, and KAT1 S4 segments, respectively. While larger than previously observed for helices with a single arginine, the destabilization is not very large, because the membrane bends to keep most charged groups out of the core.

3.3.5 Membrane Protein Stability Depends on Bilayer Stiffness

Studies on outer membrane proteins have shown that the elastic properties of the membrane influence protein stability in the membrane [85, 109]. We therefore investigated the effect of increasing bilayer stiffness on the insertion energetics by varying the bilayer compression modulus (K_a). In all calculations above, we used the K_a value of 142.5 pN/nm measured experimentally by White [40] and employed by Andersen and coworkers in their mattress models [16]. However, this value is at the low end of the physiological range, and in the presence of cholesterol K_a can be as high as 1200 pN/nm [110]. We used this later value as an upper value, and we calculated the insertion energies for each of the voltage sensor S4 helices over the entire range as shown in Fig. 3.6. In each case, we carried out the full search procedure to identify the optimal shape that minimizes insertion. As K_a increases, the total insertion energy values increase significantly due to the increase in the membrane deformation energy. Importantly, even moderate increases in the compression modulus destabilize the KAT1 S4 segment, while segments from KvAP and Kv1.2 remain stable. This observation is in very good agreement with the experimental observation that the S4 from KAT1 is not stable in the membrane alone [103], but that the isolated voltage sensor helix from KvAP readily inserts into the membrane [6].

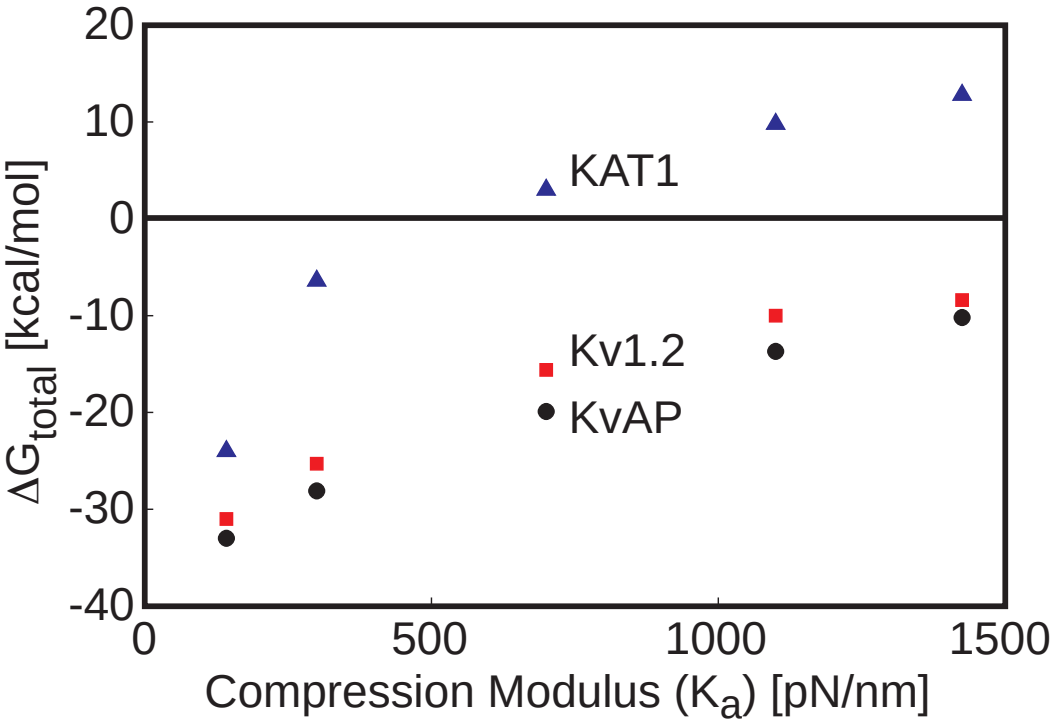

FIGURE 3.6: Protein stability depends on membrane stiffness.

The search algorithm was carried out on S4 segments from KvAP, Kv1.2 and KAT1 over a physiological range of membrane compression modulus (K_a) values. Insertion energy values for KvAP (circles), Kv1.2 (squares) and KAT1 (triangles) increase as Ka increases. Over this range, Kv1.2 and KvAP remain stable in the membrane, but KAT1 no longer inserts when K_a is above 700 pN/nm. The values at K_a = 142.5 pN/nm correspond to the configurations and energies reported in Fig. 3.5.

3.4 Discussion

We used our fast continuum method for determining the insertion energy of membrane proteins to explore several outstanding questions in membrane protein biophysics. Linking the three numeric solvers of our method and adding the search algorithm permits us to determine arbitrary distortions in the membrane, which is essential for understanding the true energetics of embedded proteins. While some implicit membrane models account for membrane flexibility [111, 112], many treat it as a rigid slab [21, 82, 96]. As shown in Fig. 3.3, our algorithm readily identifies the putative membrane-spanning region of membrane proteins and moves to bury the hydrophobic residues. As the protein is translated away from the center of the bilayer, the membrane undergoes a large, low energy conformational change to minimize the energy of the system. We believe that such distortions are important for understanding the shapes and energies of membrane proteins attached to cytoskeletal and extracellular elements such as integrins

and cadherins. Similarly, the interaction between the membrane and the protein has been shown to regulate the function of some proteins such as the stretch activated channel MscL. By systematically varying the equilibrium length of the membrane, we predict an optimal equilibrium value that minimizes the total system energy, which includes not only strain in the membrane but also electrostatics and nonpolar effects due to hydrophobic mismatch (Fig. 3.4). Based on these calculations, we predict membrane thinning at the edge of the channel for a range of equilibrium thicknesses, and the extent of this compression is in good agreement with experiments [93].

Our model suggests that amino acid insertion energies are non-additive. This is most important when considering the placement of multiple charged residues into the TM domain as we show that placing a second arginine into a TM already containing one may cost as little as 1 kcal/mol. In part due to this effect, we show that S4 voltage sensor segments can be stable in the membrane as already suggested by experiment [50], qualitative MD simulations [8], and quantitative free energy calculations [102]. Our method provides a simple mechanical explanation for this non-additivity – once the membrane bends to accommodate one charged residue it no longer needs to bend for the next one. This feature is an integral component of our method, but it is missing from other implicit membrane models [21, 82, 96] as we explicitly demonstrate in Table 3.2. However, our method still predicts insertion energies for single charged amino acids that are 4-8 kcal/mol larger than those predicted by the translocon scale [6], and 6 kcal/mol larger for arginine compared to the porin folding scale [7], but a nearly identical value for lysine compared to the porin folding scale [7]. In general, our larger values may result from limitations of our system discussed below; however, there are open questions concerning the interpretation of the translocon studies including whether the H-segment is actually centered in the membrane [9] and the role of the two additional TM segments that may alter the stability of the central residues [113].

Previously, we determined that inserting the KvAP S4-S3 helix-turn-helix motif into a flat membrane is energetically unfavorable [114], but here we show that the S4 helix is stable if the membrane is deformable. We incorporated membrane bending into our solvation model by using classical elastostatics to describe the equilibrium shape of the membrane initially proposed by Helfrich [14] and expanded to include mean bending, bilayer compression, and surface tension by Andersen and colleagues [16]. Recently, a multiscale modeling approach was developed which used a similar continuum model of the membrane to quantify the energetics of membrane deformations observed in fully atomistic membrane protein simulations [24]. This model used a simple finite difference method on a square grid to solve for the membrane shape, and with a relatively fine spatial grid, they were able to compute shapes and energies for non-cylindrical G-protein coupled receptors.

As discussed below, we intend to develop a more general membrane model that can handle arbitrarily shaped membrane proteins. Even when proteins are hydrophobically matched to the width of the membrane, it has been shown that non-cylindrically shaped proteins can induce strain in the membrane [18], and this strain can influence protein function when bilayer leaflets contain lipids favoring spontaneous curvature [115]. These considerations can be incorporated into our model through modifications to the membrane energy density in Eq. 2 as detailed by Dan and Safran [115]. At the same time, we would like to incorporate more atomistic detail of the lipid headgroups into our membrane model. For instance, charged lipids may unevenly accumulate in certain regions near the embedded protein, and the Weinstein lab has developed a mean field theory for dealing with this phenomena [23], which is well suited for our continuum method. Additionally, we could assign spatially dependent material properties that could attempt to account for different lipid densities or types in the upper versus the lower leaflet, which has been shown to affect opening of the MscL channel using simulation [116].

In summary, we have a fast, predictive method for determining the stability of proteins in the membrane that does not rely on scales or the assumption of additivity. Our results agree well with coarse-grained models and fully atomistic simulations; however, we estimate our method to be roughly 600 times faster than comparable coarse-grained MD calculations [102] and 40,000 times faster than fully atomistic calculations [9]. In the near future, we intend to include three additional features into our model. First, we intend to adopt a 3-dimensional model of the membrane that explicitly represents the strain field between the upper and lower leaflets, and we will employ edge detection to accurately represent the protein-membrane boundary. This will allow us to incorporate protein tilt into our model, which has been shown to be important for single TM WALP peptides [117–119], and it will also allow us to investigate proteins of arbitrary shape. Second, MD simulations have shown that charged residue side chains "snorkel" to interact with the polar headgroups and solvent [9]. To account for these changes, which can impact insertion energies, we will incorporate a rotamer library search on the charged residues to minimize membrane distortions and electrostatic penalties. Third, we use a simple SASA model for the nonpolar energy. We will explore different continuum models for this energy that are more specific for water to membrane transfer free energies as well as those that account for dispersive solute-solvent interactions [48]. Finally, we intend to integrate the membrane deformation algorithm presented in this manuscript into our software APBSmem [29] to help orient proteins in the membrane for use in interpreting experiments and carrying out MD simulations in a similar manner to the Orientations of Proteins in Membranes database [21].

Chapter 4

Continuum approaches to understanding ion and peptide interactions with the membrane

In Chapter 3 we applied our model to several cases of charged proteins in the membrane. In this chapter we move to a smaller scale as we apply our model to examine the interaction between ions and the membrane. We utilize coarse-grained molecular dynamics (MD) simulations to guide key input parameters for our continuum models, and we show that our ion permeation energy profiles as well as the equilibrium membrane deformation shapes from our model are in qualitative agreement with atomistic simulations. We discuss the nature of the transition state for the movement of charged species through the membrane, as well as our ability to probe this state with available computational methods. Additionally, we highlight important considerations regarding the non-equilibrium nature of permeation and dependencies on system size which may be neglected in many coarse-grained and atomistic simulations. [1]

[1]This chapter adapted from: Latorraca, N.R. (co-first author), Callenberg, K.M. (co-first author), Boyle, J.P., Grabe, M. (2013). Continuum approaches to understanding ion and peptide interactions with the membrane. BBA - Biomembranes (Submitted)

4.1 Introduction

The cell membrane serves as a critical barrier differentiating the interior of the cell from the extracellular medium. This lipid bilayer is inextricably linked to cellular identity - without a membrane, a cell would lose control of its internal chemistry as its contents diffused into the external milieu. Destruction of the cell membrane therefore equates with cell death, and organisms have evolved strategies to kill other cells by attacking their membranes, as in the mechanisms of many antibiotics. Strikingly, cells induce their own deaths by compromising the integrity of their membranes during apoptosis through decoupling the cytoskeletal network from the membrane, which leads to blebbing [120].

Chemical and physical principles underlie the membrane's dual role as defender against invaders and regulator of nutrient transport into and out of the cell. Packed hydrophobic lipids form a low-dielectric barrier to charged and polar molecules, while membrane-spanning channels and pumps exert exquisite control over the passage of ions and macromolecules. Such transmembrane (TM) proteins typically consist of hydrophobic amino acids energetically stable in the low-dielectric membrane. However, proteins with functionally important, highly charged moieties do reside in the hydrophobic bilayer core, suggesting that some mechanism must exist to mitigate the electrostatic cost of their insertion. The arginine- and lysine-rich S4 voltage sensor segments of voltage-gated potassium channels must respond to changes in potential across the membrane to open and close the channel [52, 97]. Previous works posited that portions of the protein surrounded these helices, shielding them from the hydrophobic environment [56], but recent experimental and computational data have demonstrated that charged moieties may directly penetrate and interact with the lipid bilayer.

In vitro translocation experiments suggest that TM segments harboring a central, charged residue partition into the bilayer at a small energetic cost of only 2-3 kcal/mol [121], while molecular dynamics (MD) simulations have demonstrated that an arginine residue positioned in the bilayer core may "snorkel", bringing water and ions into the bilayer to interact with the buried amino acid [9, 69]. Membrane deformations and distortions, therefore, represent a potential mechanism for charge insertion into the bilayer. We previously tested this computationally with S4 segments from three voltage-gated potassium channels and found that they favorably insert into a continuum, elastic bilayer, suggesting that membrane bending provides a simple mechanical explanation for the presence of charged residues in TM segments [37].

Membrane elasticity likely facilitates a range of biological processes, from the large-scale deformations required for vesicle budding and fusion to the localized permeation of small

molecules across bilayers. Carrier-mediated ion transport and bare ion permeation constitute two distinct contexts in which to further investigate how membrane bending modulates membrane transport phenomena. For example, ionophores such as Streptomyces-derived valinomycin selectively chelate potassium ions and shuttle them across host cell bilayers, disrupting their electrochemical gradient. Similarly, the threat of bare permeation of small ions and water molecules might have spurred the development of a high fidelity phospholipid bilayer as an early and critical evolutionary adaptation on the molecular level, later exploited by processes such as oxidative phosphorylation. Nonetheless, bare ion permeation, while rare, does occur, and its mechanism remains unclear.

Here, we focus on bare ion penetration into the membrane, which eventually leads to permeation across the bilayer. Ion permeation is thought to occur via two distinct mechanisms: solubility-diffusion and ion-induced pore formation. In the former, the ion must partition into the hydrophobic core, surmounting a considerable energy barrier, diffuse across the core, and resolvate as it exits the opposite membrane leaflet [122, 123]. However, rates for bare ion permeation predicted from solubility-diffusion theory disagree with experiment by several orders of magnitude [51]. Others have proposed that the presence of a charge induces the formation of membrane-spanning defects, which allow for the permeation of charges and water molecules through a temporary, electrostatically-favorable environment, and the primary barrier to permeation is the cost of creating a pore in the membrane. Paula and colleagues investigated how potassium permeation changes with changing bilayer thickness and found that crossing rates for thinner bilayers matched rates predicted theoretically from an ion-induced pore formation model, while rates for thick bilayer crossing matches predictions from solubility-diffusion models [124]. Recent MD data have revealed that an N-methyl guanidinium ion crossing a thin bilayer does give rise to a transient water pore through the membrane, while for thicker membranes, the bilayer simply bends from one side or the other to promote favorable electrostatics [125].

Previously, we developed a method that uses elasticity theory to predict membrane distortions around TM proteins harboring charged, buried residues [22]. Bending drastically reduces the energy required to insert these proteins in the membrane, and our model is in quantitative agreement with results from atomistic MD simulations, but at a fraction of the computational cost. Next, we developed a method for determining the shape of the membrane around chemically complex TM proteins, to determine the configuration that minimizes the total insertion energy [37]. At present, our continuum model effectively assesses the energetic equilibria involved in static membrane-protein interactions. Here, we extend our work by considering the penetration of ions into the membrane from solution. We compare our results with fully atomistic and coarse-grained

molecular dynamics simulations as well as experiment. We consider how variations in bilayer properties such as hydrophobic thickness, membrane compressibility, and membrane curvature, influence the energetics of ion penetration, and we discuss the implications of our results on our current understanding of bare ion permeation.

4.2 Methods

4.2.1 Description of the Continuum Model

Previously, we developed a continuum membrane model and search algorithm to calculate insertion energies and membrane distortions for single pass TM proteins[22, 37]. Briefly, in our model the total energetic stability of the solute in the membrane, ΔG_{total}, is approximated by the following equation:

$$\Delta G_{total} = \Delta G_{mem} + \Delta G_{elec} + \Delta G_{np} \tag{4.1}$$

where the first term on the right hand side (ΔG_{mem}) is the energy associated with distortions in the membrane caused by embedding the solute, the second term (ΔG_{elec}) is the electrostatic cost required to move the charged solute from solution into the low-dielectric environment of the membrane, and the final term (ΔG_{np}) is the nonpolar or hydrophobic energy gained by removing portions of the solute surface from water and burying them in the membrane. All energies are calculated with respect to the molecule free in solution far from an unstressed membrane; therefore, negative values indicate stabilization in the membrane. This model is in excellent agreement with free energies calculated from simulations [22], and the model supports experimental observations on the stability of voltage sensors from voltage-gated potassium channels [37].

All of the energies presented in this manuscript are equilibrium values calculated from static configurations. The exact computational details closely follow the procedure outlined in our previous manuscript [37] and additional details can be found in [22]. Briefly, the energetic terms and procedure are calculated as follows.

Membrane Deformation Energy (ΔG_{mem}). We use linear elasticity theory to determine the shape and energetic cost of deforming the bilayer at the site of ion penetration. Specifically, we use a modified Helfrich Hamiltonian, which includes terms for membrane bending, compression and tension [14, 87, 126]:

$$\Delta G_{mem} = \frac{1}{2}\int_{\Omega} \frac{K_a}{L_0^2}(u^- - u^+)^2 + \ldots \\ \frac{K_c}{2}\left((\nabla^2 u^-)^2 + (\nabla^2 u^+)^2\right) + \ldots \\ \frac{\alpha}{2}\left((\nabla u^-)^2 + (\nabla u^+)^2\right) dxdy, \tag{4.2}$$

where u^+ is the shape of the upper leaflet and u^- is the shape of the lower leaflet, L_0 is the equilibrium length of the membrane, K_c is the membrane bending energy, α is the surface tension, and K_a is the compression modulus. The surfaces are represented in the Monge gauge, and correspondingly, the integral extends over the entire x-y domain, Ω. The functional derivative of Eq. 4.2 with respect to variations in u^+ and u^- gives the following partial differential equations (PDEs) that determine the shapes of each leaflet:

$$\nabla^4 u^+ - \frac{\alpha}{K_c}\nabla^2 u^+ + \frac{2K_a}{K_c L_0^2}(u^+ - u^-) = 0 \\ \nabla^4 u^- - \frac{\alpha}{K_c}\nabla^2 u^- + \frac{2K_a}{K_c L_0^2}(u^- - u^+) = 0. \tag{4.3}$$

The last term on the left hand side of each equation couples the upper and lower leaflets. This coupled set of fourth-order equations requires two boundary conditions (BC) to be specified on the inner boundary, where the bilayer contacts the ion, and at the outer boundary, far from the ion. We assume that the membrane is flat at its equilibrium length, L_0, far from the ion. At the ion, we impose a radially symmetric contact height for the upper and lower leaflets, and we impose contact angles that determine the slope of the membrane as it meets the ion (Fig. 4.1). Thus, four independent parameters determine the boundary conditions at the inner boundary. We determined these values by carrying out a search on all four parameters to find the membrane shapes that minimize the total energy in Eq. 4.1 as discussed in reference [37]. In some cases described in the Results, we imposed some contact angles by hand based on correspondence with membranes shapes from coarse-grained MD simulations. The PDEs in Eq. 4.3 were solved using a second-order finite difference method written in radial coordinates (r and θ), and the membrane bending energy was determined by using an second-order scheme to compute the integral in Eq. 4.2. While the solver is a general 2D solver, the solutions only vary in r, not θ, due to the underlying symmetry of the system. All code was written in Matlab (The MathWorks Inc., Natick, Massachusetts).

Electrostatic Energy (ΔG_{elec}). We solve the non-linear Poisson-Boltzmann equation (NPBE) to determine the cost of inserting a charged molecule into a neutral, uncharged bilayer:

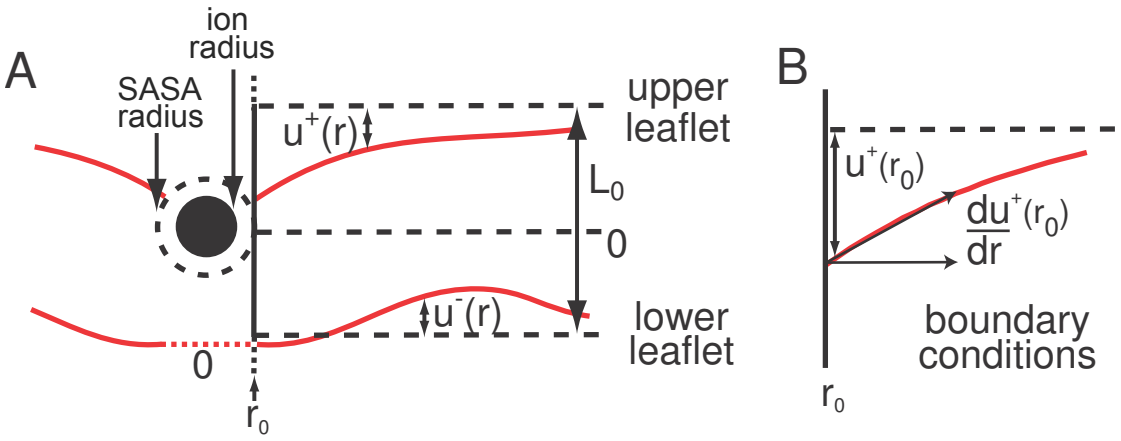

FIGURE 4.1: Geometry of the system in the continuum model.

(A) Cross section showing membrane distortions in the upper and lower leaflets. Solid red lines indicate the membrane-water interfaces. Dashed black lines indicate the equilibrium heights of the membrane leaflets and the midplane at z = 0. u^+ and u^- represent the displacement from equilibrium for the upper and lower leaflets, respectively. The equilibrium bilayer thickness is L_0. The inner boundary conditions are applied at r_0, where the solvent accessible surface area (SASA) of the ion contacts the membrane. (B) The contact point $u^+(r_0)$ is determined from the search angle that minimizes the total energy Eq. 4.1. The ion-membrane contact angle, du^+/dr, is a free parameter in the model and is tuned to molecular simulation according to Eq. 4.7. The contact point and angle on the lower leaflet are treated in similar manners.

$$-\nabla\cdot[\epsilon(\vec{r})\nabla\phi(\vec{r})]+\kappa^2(\vec{r})sinh[\phi(\vec{r})]=\frac{e}{k_BT}4\pi\rho(\vec{r}), \tag{4.4}$$

where $\phi(\vec{r}) = \Phi(\vec{r})/k_BT$ is the reduced electrostatic potential at position $\vec{r}$, κ is the Debye-Huckel screening coefficient to account for ionic shielding, ϵ is the spatially-dependent dielectric constant, e is the electron charge and ρ is the charge density within the protein. The electrostatic potential is solved using the software APBS [73] along with scripts for including the dielectric influence of the membrane similar to those found in APBSmem [29]. The electrostatic energy of the ion in the membrane compared to solution, ΔG_{elec}, is calculated by subtracting the total energy of the molecule in the membrane from the value in solution, far from the membrane. This energy is usually referred to as the Born solvation energy, ΔG_{Born}.

In a separate electrostatics calculation, we include the influence of the membrane dipole potential by adding a sheet of dipole charges at the interface between the headgroup and the hydrocarbon core – one sheet for the upper leaflet and one for the lower leaflet. This term accounts for the large electrostatic role that the membrane dipole plays in charge permeation events, and we tune the charges and the separation distance of the dipoles to achieve +300 mV at the center of the membrane, which is estimated for phosphatidylcholine bilayers [108]. For this calculation, we solve the linearized form

of the Poisson-Boltzmann equation (LPBE) to expedite the calculations. First, we calculate the total electrostatic energy of the charged molecule in the bilayer with the dipole potential on. Next, we subtract off the "self" dipole energies by turning off the charge on the permeating molecule and re-performing the calculation with the dipole charges still on. Finally, we subtract the electrostatic energy of the charged molecule with the dipole potential turned off. These three terms added in this way provide the interaction energy between the ion and the membrane dipole potential, ΔG_{dipole}. The total electrostatic energy is then given by the sum of the Born solvation energy and the dipole energy: $\Delta G_{elec} = \Delta G_{Born} + \Delta G_{dipole}$. Please note that all electrostatic energy calculations are multiplied by a factor of 1/2 to account for double counting of the charge-charge terms. This value is automatically accounted for in the energies returned by APBS [73], so we do not discuss these factors above.

Nonpolar Energy (ΔG_{np}). The nonpolar energy arises from the tendency of water to exclude molecules, resulting in the clustering of hydrophobic proteins and the stabilization of molecules in the membrane. We model the nonpolar energy, ΔG_{np}, as proportional to the difference in the ion's solvent accessible surface area (SASA) in the membrane compared to solution:

$$\Delta G_{np} = a \cdot (A_{mem} - A_{sol}), \tag{4.5}$$

where A_{mem} is the ion SASA in the membrane, A_{sol} is the total ion SASA, and a = 0.028 (kcal/mol)/Å^2. The constant a was determined based on the partitioning of small nonpolar molecules between aqueous and organic phases [127]. SASA values are calculated with a modified Shrake-Rupley algorithm [32] using the solvent-accessible surface representation of the ion with a water probe radius of 1.4 Å. In the presence of the membrane, if the point on the surface of the ion lies between the upper, u^+, and lower, u^-, leaflets then it is considered occluded and does not contribute to A_{mem}. Matlab's cubic interpolation function was used to navigate between the position of the point on the ion surface and the grid points describing the upper and lower membrane surfaces.

Minimizing the Total Energy. To simulate the permeation of an ion, we systematically translated the molecule in steps of 3 Å along an axis orthogonal to the membrane normal, which we call the z axis. For each position, we carried out a search algorithm to determine the deformation that minimized the total energy of the system in Eq. 4.1. Initially, during the search, the contact height of the upper and lower leaflets was varied as was the contact angle with which the leaflets meet the ion (Fig. 4.1B). We then imposed specific contact angles in accordance with the shapes of coarse-grained MD

simulations during these searches, described in greater detail later. To facilitate faster convergence of the search, we used the final, optimal membrane configuration from one calculation as the starting guess for the subsequent position along the pathway.

4.2.2 Coarse-Grained Simulations

We performed coarse-grained MD simulations using GROMACS version 4.5.3 [128] and the MARTINI forcefield version 2.0 with polarizable water [129]. Simulations were performed with umbrella sampling so that the z-position of the ion was harmonically restrained with respect to the center of mass of the membrane. For cation simulations, a Na^+ was used rather than K^+ since K^+ has not been parameterized in MARTINI. We sampled ion positions from one side of the membrane to the other in 1 Å steps. In each simulation, the ion was initially placed at the restraint minimum in a pre-equilibrated bilayer. We could possibly have benefited from a speed up in convergence by using the final configuration from the previous ion position to initiate new simulations, but we were also interested in the ability of the coarse-grained membrane to undergo large scale conformational changes in a limited time, so we initiated all simulations from a flat membrane. After energy minimization, molecular dynamics was performed for 60 ns. The first 10 ns of each simulation were discarded as equilibration, leaving 50 ns of simulation time for analysis.

We used semi-isotropic pressure coupling with a Berendsen barostat [130] at 1 bar in x and y with a coupling of 1 ps, a compressibility of 3.0×10^{-5}, and temperature set at 320 K. PME electrostatics were used with a 1 Å grid spacing.

The software `g_wham` was used to calculate the potential of mean force (PMF) using the weighted histogram analysis method (WHAM) [131, 132]. Two hundred bins were used to construct the histogram, and the energy in bulk solution at ±30 was defined to be 0.

4.2.3 Systems Setups and Parameters

We created input files containing radii and charge for the potassium ion and chloride ion calculations, assigning them their respective charges of +1 and -1, and we used the unhydrated radii, 1.49 Å for K^+ and 1.64 Å for Cl^-, [133]. We also had to specify r_0, the radius of the solute inclusion. See Figure 4.1 for an illustration of the geometry of the system. For K^+ and Cl^- we again used literature values, this time for the hydrated ionic radii [133].

To capture the effect of increasing bilayer thickness on ion permeation in our continuum model, we had to consider how lipid alkyl tail length, a variable in MD simulations and

TABLE 4.1: Parameters for all continuum calculations

Parameter	**Value**
Electrostatics Grid Dimensions	$161 \times 161 \times 161$ Å^3
Coarse Grid Lengths	$200 \times 200 \times 200$ Å^3
Fine Grid Lengths	$50 \times 50 \times 50$ Å^3
Counter-Ions	0.1 M symmetric salt
Protein Dielectric	2.0
Membrane Dielectric	2.0
Head group Dielectric	80.0
Solvent Dielectric	80.0
Solvent Probe Radius	1.4 Å
Surface Sphere Density	10.0 grid points/Å^2
Temperature	298.15 K
Membrane Thickness	See Table 4.2
Head group Thickness	8.0 Å
Bending modulus (K_c)	See Table 4.2
Compression modulus (K_a)	2.30×10^{-11} N/Å
Surface tension (α)	3.00×10^{-13} NÅ

experiments, corresponds to bilayer thickness, and how this in turn affects the elastic properties of the bilayer. The compression modulus, K_a, does not vary significantly between different lipid chain lengths. However, the bending modulus, K_c, does increase systematically as lipid chain length increases [134]. Rawicz and co-workers developed an empirical relation to describe the hydrophobic thickness to K_a and K_c:

$$K_c = \frac{L_c^2}{24} K_a, \tag{4.6}$$

where 24 is an empirical constant and L_c is the equilibrium hydrocarbon thickness, which is equal to the entire bilayer thickness, L_0, minus twice the thickness of the headgroup region. For all calculations, we used 8 Å as the headgroup thickness [27]. We computed K_c from an average K_a of 230 mN/m [134] and from hydrophobic thicknesses reported by Li and co-workers [125], with the exception of DSPC. For the hydrophobic thickness of DSPC, which was simulated at a higher temperature than the other lipid types, we calculated the average increase in hydrophobic thickness among the other bilayers and added this value to the thickness of DPPC. Please see Table 4.2.

All coarse-grained simulations started with an identical pre-equilibrated DPPC bilayer composed of either 128 lipid and 2000 water molecules or 512 lipid and 8000 water molecules. Ions were added as necessary to neutralize the system charge. Helices for the coarse-grained molecular dynamics simulations were constructed with ideal alpha-helical backbone angles using VMD Molefacture plugin version 1.2. The secondary structure of the helices was harmonically restrained with 1000 kJ/mol restraints.

TABLE 4.2: Elastic membrane material properties

Lipid type	**Thickness**	K_a	K_c
DDPC (10)	32.0 Å	2.30×10^{-11} N/Å	2.45×10^{-10} NÅ
DLPC (12)	36.3 Å	2.30×10^{-11} N/Å	3.95×10^{-10} NÅ
DMPC (14)	39.9 Å	2.30×10^{-11} N/Å	5.47×10^{-10} NÅ
DPPC (16)	43.6 Å	2.30×10^{-11} N/Å	7.30×10^{-10} NÅ
DSPC (18)	47.7 Å	2.30×10^{-11} N/Å	9.45×10^{-10} NÅ

See Tables 4.1 and 4.2 for continuum calculation parameters.

4.3 Results

4.3.1 Using coarse-grained simulations to tune the continuum model

When we originally developed our continuum membrane bending model to explore the stability of charged membrane proteins [22], we were inspired by MD simulations that showed significant membrane bending around buried charged amino acids [9] and membrane-penetrating charged molecules [69]. For embedded membrane proteins, our model produced deformations similar to those observed in fully atomistic simulations [22, 37], and here we decided to explore its ability to match deformations observed in ion and charged molecule permeation studies. We moved an ion from the upper solution at z = +30 Å to the lower solution at z = -30 Å in 3 Å steps. The membrane was modeled with DPPC lipids, and in the flat, unstressed case it spans from +21.8 Å to -21.8 Å, centered at zero. We initially modeled a large membrane patch with a radius of 800 Å in the x-y plane. Four equilibrium snapshots of the ion at different positions along the permeation pathway are shown in Fig. 4.2A. Interestingly, the membrane adopts a low-energy bent conformation to avoid penetration by the ion. There is some bending of the upper and lower leaflets at the site of contact with the ion, but the most prominent feature is the large deflection of the entire patch in the ± z direction depending on the position of the ion. Avoidance by the membrane is not surprising, given the low energetic cost for the membrane to adopt a large wavelength deformation and the high energetic cost for a charged molecule to penetrate the low-dielectric environment of the membrane interior. However, this behavior is not observed in MD simulations in which the molecule penetrates deeply into the membrane and sharp curvature is observed at the site of penetration [69, 125, 135, 136].

The membrane patch size used in the continuum calculations in panel A is very large compared to most MD simulations of membranes. To better understand the differences between our continuum model and previous MD simulations, we carried out our own

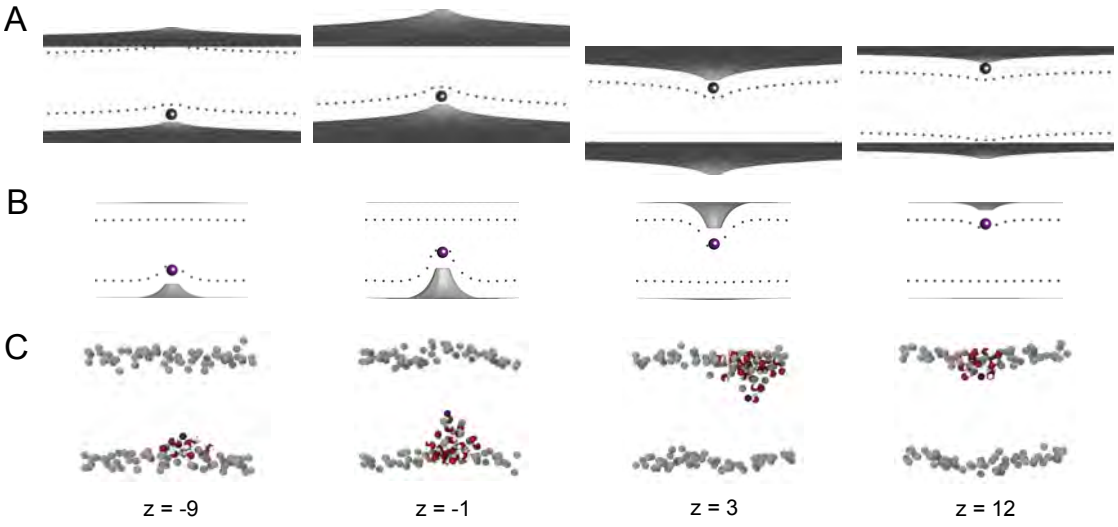

FIGURE 4.2: Continuum membrane bending is qualitatively similar to deformations observed in coarse-grained simulations.

In all three rows, 4 snapshots are shown for a cation (purple) placed at -9, -1, +3, and +12 Å with respect to the center of mass of the membrane. In panels A and B the gray surfaces are the membrane-water interfaces, which separate the headgroup region from aqueous solution. The interfaces between the headgroup region and the membrane core are shown as gray dotted curves. The phosphate beads are gray in the snapshots in panel C and penetrating waters are red and white. A) Snapshots from the continuum membrane bending model for a large patch of membrane with boundary conditions applied at 800 Å from the ion. A search was carried out to identify the optimum contact angle and contact value for the membrane at the upper and lower leaflets for each position of the ion. The membrane bends to avoid the ion at all positions even when the ion is placed near the center of the system (z = -1 Å). B) Snapshots from the continuum model for a small patch of membrane with a 35 Å radius. A search was carried out to identify the optimum contact value for the membrane at the upper and lower leaflets, and the contact angle was fixed at $\alpha = 0.85$ and $\beta = 0$ according to Eq. 4.7 to better match the results in panel C. For this small patch of equivalent size to most MD simulations, the membrane is not able to adopt a low energy, large scale deformation to avoid penetration by the ion. The leaflet being penetrated bends sharply, while the opposite leaflet adopts a more gentle bend to relieve compression. C) Snapshots from a coarse-grained MD simulation of Na^+ penetrating a DPPC bilayer using the MARTINI forcefield. The membrane is approximately square with a side length of 65 Å, and it is composed of 128 DPPC lipids. Starting with an identical flat, equilibrated bilayer, 71 independent umbrella sampling simulations were performed with the ion restrained at positions along the membrane normal. The deformation patterns are similar to the corresponding snapshots from the continuum model in panel B.

MD simulations of a cation penetrating a bilayer using the coarse-grained MARTINI force field [129] (Fig. 4.2C). We also carried out continuum calculations on a much smaller patch size closer to those used in MD simulations (Fig. 4.2B). As discussed in the Methods, a Na^+ was used for these studies since K^+ is not parameterized in the MARTINI force field. The membrane was composed of 128 DPPC lipids, and the x-y extent of the system was 65 Å $\times$ 65 Å. Umbrella sampling was used to harmonically restrain the ion at positions along the z direction extending from -30 Å to +30 Å. Simulations were carried out at each position. As in previous work, we observe deep penetration of the ion into the membrane causing severe deformation of the lipids adjacent to the ion, which extends laterally away from the site of penetration in a manner consistent with an elastic deformation (Fig. 4.2C).

Simply reducing the size of the membrane patch to typical MD simulation sizes already produces continuum membrane deformations that are similar to the coarse-grained results (data not shown). However, to more closely match the coarse-grained snapshots, we tuned the contact angles at the upper and lower leaflets where the membrane touches the permeating ion. We observed an empirical relationship between the depth of the penetration from one side of the membrane, say u^+ in this case when penetrating from the upper solution, and the contact angle at the upper and lower boundaries:

$$\begin{aligned} \frac{du^+(r_0)}{dr} &= \alpha u^+(r_0) \\ \frac{du^-(r_0)}{dr} &= \beta u^+(r_0), \end{aligned} \tag{4.7}$$

where α and β are constants with $\alpha = 0.85 > \beta = 0$ as indicated by the larger contact angle at the leaflet from which the ion is penetrating the membrane. These relationships are imposed on the continuum model throughout the rest of the manuscript. Since we imposed contact angles on the model that do not minimize the total energy, the solutions shown in panel B are higher energy than those shown in panel A, which means that the states observed in the MD simulations are non-equilibrium, high energy states. There could be several reasons that the MD simulations produce higher energy states than the continuum model. First, the finite system size of the MD simulations may restrict the degree of membrane bending, and second, the simulations may be too short to observe large scale conformational changes of the membrane. We will discuss these two aspects, and other potential reasons, in more detail later.

4.3.2 Ion free energy profiles from continuum model match profiles from molecular simulations

Our model successfully reproduces the membrane shapes observed in CG simulations during ion penetration; however, it is not clear if the energetics produced from our model are in agreement with values from atomistic simulations. Li and colleagues found that a continuum model of guanidinium permeation poorly matched the results of their atomistic MD simulations [125]. In particular, energy profiles obtained with their continuum model exhibited relatively flat, rounded peaks at the free energy maximum when the ion was at the center of the bilayer. In contrast, their MD simulations yielded sharply peaked "witch's hat" profiles, which qualitatively match energy profiles obtained in other ion permeation simulations [135, 137]. Additionally, guanidinium is stabilized in the headgroup region relative to bulk solution, as observed in cation simulations [135, 137], but their continuum model predicts no stabilization in the headgroup region [125].

To understand how our model compares with atomistic simulations, we computed the total free energy according to Eq. 4.1 for K^+ and Cl^- movement across the membrane in 3 Å steps (red and blue solid lines in Fig. 4.3, respectively). At the center of the bilayer both curves are sharply peaked, just as observed in the atomistic MD simulations carried out by Li and co-workers [125]. Also, our model predicts that K^+ is stabilized in the headgroup, as shown in simulation [125, 135, 137]. Stabilization in our model occurs because we assume that the headgroup has a high dielectric value so there is little electrostatic penalty for moving charged species into this region, while we assume that there is a favorable nonpolar energy associated with the solute leaving the aqueous environment. In fact, the snapshots in Fig. 4.2B show that the membrane bends during penetration to keep the ion in the headgroup region, as noted previously for atomistic simulations [125]. Thus, our model does a very good job of recreating both the qualitative snapshots and the quantitative energy profiles predicted from atomistic simulations. We also carried out calculations in which the bilayer was not allowed to bend, producing the red and blue dashed lines in Fig. 4.3 for K^+ and Cl^-, respectively. These results are in qualitative agreement with the continuum model created by Li and colleagues, which also assumes that the membrane is incapable of bending [125], and we believe that these results highlight the importance of including membrane bending in any continuum model of the membrane.

Paula and colleagues used spectrofluorimetry to demonstrate that anions permeate vesicles composed of phosphatidylcholine-based lipids at a much greater rate than cations [124, 133]. Since K^+ and Cl^- have comparable hydrated ionic radii, they suggested that charge differences between these ions, rather than size differences, account for the

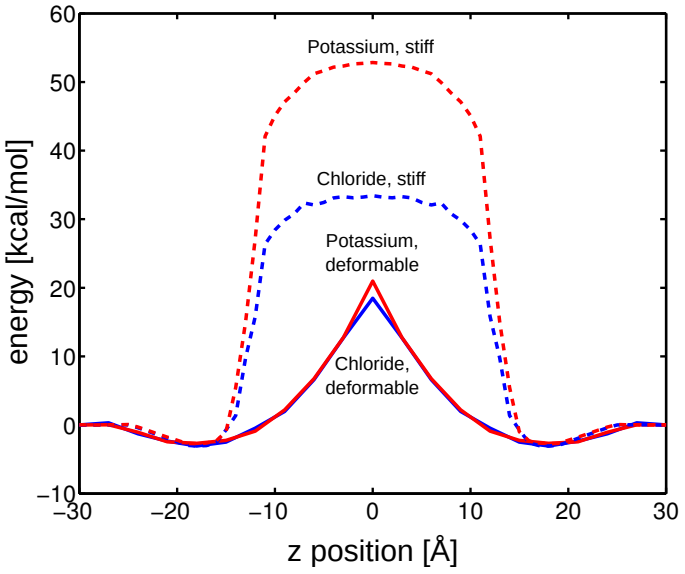

FIGURE 4.3: Free energy profiles along the transmembrane coordinate for a cation and an anion.

Using our fully flexible membrane model, we translated K^+ (solid red curve) or Cl^- (solid blue curve) across the membrane in 3 Å steps with the ion initially positioned in bulk solvent approximately 6 Å from the membrane-water interface (z = -30 Å). As the ions penetrate the bilayer from below at z = -25 Å, they are stabilized in the headgroup region. At the bilayer center, the membrane has undergone maximal deformation to ensure that the ion does not penetrate the hydrocarbon region of the membrane. The symmetric K^+ and Cl^- profiles both exhibit peaks at the membrane center, and the equilibrium configurations fail to show penetration of the ions into the hydrophobic core. The free energy profiles for cation and anion permeation through a non-deformable membrane (dashed curves) are plotted to demonstrate how membrane elasticity minimizes the energy required to move ions into the center of the membrane by 12-30 kcal/mol. The membrane dipole stabilizes Cl^- by ∼20 kcal/mol in the non-deformable model (difference between dashed curves), but only by 2-3 kcal/mol in the membrane bending model (difference between solid curves).

differences in their permeability values [133]. The only term in our model that accounts for differences between similarly sized ions of different charge is the membrane potential dipole term, which is part of ΔG_{elec}. The charge composition of PC based lipids creates a positive dipole potential in the membrane interior, which is measured to be on the order of +300 mV [108]. The positive value causes an increase in the energetic barrier for cations compared to anions, as can be seen by the higher energy value for K^+ (red) to permeate the bilayer compared to Cl^- (blue) (Fig. 4.3). The energy difference is larger for ions permeating through the core of a flat bilayer since they experience the full +300 mV of the dipole potential, while ions penetrating bent bilayers remain at the interface between the headgroup and the hydrophobic core where the dipole field is not at its maximum value (compare solid curves to dashed curves in Fig. 4.3). Interestingly, an atomistic MD simulation comparing Na^+ and OH^- permeation across saturated phospholipid bilayers reported a permeation barrier for anions 5-10 kcal/mol greater

than that encountered by cations using the Smondyrev lipid forcefield [138] with the SPC/Fe water model [135]. Similarly the McCammon group found that the barrier for Cl^- was +2 kcal/mol higher than K^+ using CHARMM32 with a TIP3P water model [137]. So while our continuum model predicts that Cl^- permeation should be easier than K^+ permeation, in qualitative agreement with experiments, atomistic simulations suggest just the opposite.

Another difference between anion and cation interactions with phospholipid bilayers is that many MD simulations suggest that cations are stable in the headgroup region with respect to bulk solvent, while anions are not [135, 137]; however, we do note that simulations with GROMACS suggest that Cl^- binds to the headgroup, but more weakly than Na^+ [139]. Our coarse-grained simulations using the MARTINI model predict behavior similar to the Tepper and Khavrutskii atomistic simulations (data not shown). In stark contrast, our continuum model predicts that cations and anions are equally stable as they partition into the headgroup region from solvent (Fig. 4.3), an effect that results from the nonpolar contribution of inserting ions of equivalent surface areas as well as our treatment of the membrane dipole potential. We model the charge on the phospholipid headgroup as a uniform surface of positive and negative charges with a thin separation centered at the interface between the headgroup and hydrocarbon core. Ions do not experience the influence of the membrane dipole potential until they cross this boundary, so there is no charge selectivity for molecules in the headgroup region. Interestingly, Knecht and Klasczyk recently showed using electrophoresis and isothermal titration calorimetry that Na^+ and Cl^- exhibit similar affinities for interacting with the surface of POPC bilayers [140], in agreement with predictions from our model.

4.3.3 Permeation barriers increase with increased membrane thickness

As one might expect, the permeability of ions across phospholipid membranes decreases as the membrane thickness increases [124, 133]. To investigate the dependence of the energy profiles on membrane thickness, Li and colleagues carried out atomistic MD simulations of guanidinium penetrating homogeneous phospholipid bilayers having tail lengths ranging from 10 carbons (DDPC) to 18 carbons (DSPC) [125]. We used our model to compare with the atomistic results by translating a K^+ ion in 3 Å steps across membranes of comparable thicknesses and corresponding material properties as those examined by Li and colleagues. At each step, we carried out a search algorithm to identify the contact values of the upper and lower leaflets that minimized the insertion energy, while holding the contact angle constant as shown in Eq. 4.1. The energy required to move the ion into the middle of the bilayer increases dramatically as the membrane thickness increases (Fig. 4.4), which appears to be in qualitative agreement

with the results from experiment [124]. Additionally, the shapes of the energy profiles are remarkably similar to the results obtained for guanidinium from MD simulations, which are shown in the inset. The energy for the arginine side chain at the center of the membrane is in good agreement with that predicted by our model for K^+ for all but the thickest membrane. Unfortunately, atomistic free energy profiles as a function of membrane thickness do not exist for K^+, and the reduced energy for arginine is certainly in part related to chemical differences. The curves from both methods exhibit a constant slope approaching the membrane center, which indicates that there is a constant force on the molecule. In the continuum model, the constant force is largely the linear restoring force of the elastic membrane. Except for the thickest membrane, DSPC, the permeation energy barrier increased by about 5 kcal/mol for each increase in bilayer thickness, similar to the trend seen by Li and colleagues shown in the inset of Figure 4.4 [125]. While our method matches the results from atomistic simulations very well, one difference is that for the thin bilayers, DDPC and DLPC, the energy profiles from MD simulations plateau rather than peak as predicted by the continuum model (Fig. 4.4). This discrepancy is most likely related to the permeation mechanism as discussed next.

4.3.4 The nature of the transition state for ion and small molecule permeation

The solubility-diffusion model and the ion-induced pore formation model are the two prevailing models for passive ion permeation across bilayers [133]. The critical step in each mechanism, the transition state, is the point at which the ion has penetrated deep into the bilayer and is ready to cross to the other side. If the process occurs at equilibrium, symmetry arguments mandate that the shape of the membrane at the transition state must be the same whether permeation occurs from the upper leaflet or the lower leaflet. For the solubility-diffusion model, the transition state occurs once the ion has partitioned into the hydrophobic core of the flat, unstrained membrane and diffused half way across the membrane. In the ion-induced pore model, ion penetration creates a defect in the membrane in which the headgroups from both leaflets surround the ion, and water penetrates from both sides. From our model, when the ion is at the center of the membrane the symmetry is broken depending on which side the ion originated (Fig. 4.5A). Both snapshots show that the ion still remains in the headgroup, and the entire hydrophobic width of the membrane, d, separates it from the adjacent leaflet. Moving the ion 1 Å farther produces a snap through bifurcation in which the ion is now localized in the headgroup region of the other leaflet (Fig. 4.5A). This

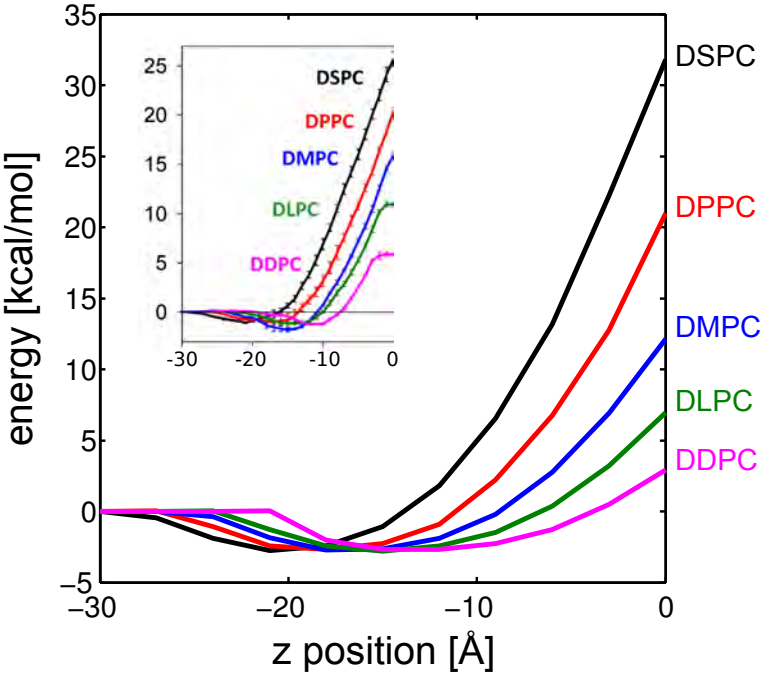

FIGURE 4.4: Free energy profiles for K^+ penetration into bilayers of different thicknesses.

For all thicknesses, the ion is stabilized as it enters the headgroup region, but rises to a sharp-peak at the membrane center. The penetration energy increases with membrane thickness with values at the center ranging from 3 to 32 kcal/mol. The inset shows similar free energy profiles obtained from atomistic MD simulations carried out on the positively charged arginine side chain analogue, $MguanH^+$ [125]. The equilibrium length (L_0) and bending modulus (K_c) were increased to match the known properties of lipids being modeled, and values are given in Table 4.2. The compression modulus (K_a) was held constant since it is thought to be independent of the hydrophobic thickness. In all cases, L_0 for each lipid type is similar between the MD simulations and continuum model except for DSPC, as discussed in the Methods.

second configuration also has broken symmetry, and in fact, our model never samples the transition state.

The range of measured permeability values as a function of membrane thickness is smaller for chloride ions (10^{-9} to 10^{-8} cm/s) than it is for K^+ ions (10^{-12} to 10^{-10} cm/s) [133]. Based on these measurements, Paula and colleagues argued that anions always permeate via a solubility-diffusion model, but the wide spread in K^+ permeabilities can only be understood if permeation occurs by solubility-diffusion for thick membranes and ion-induced pore model for thin membranes [133]. The careful PMFs carried out by the Allen group on guanidinium penetration seem to support this hypothesis. The peaked "witch's hat" profiles occur for thick membranes (DMPC-DSPC), which indicates that the ion never leaves the headgroup region as it is moved to the center of the bilayer, as observed with our continuum model (inset and main figure of Fig. 4.4, respectively). So for permeation to occur, the cation must still partition into the hydrophobic core

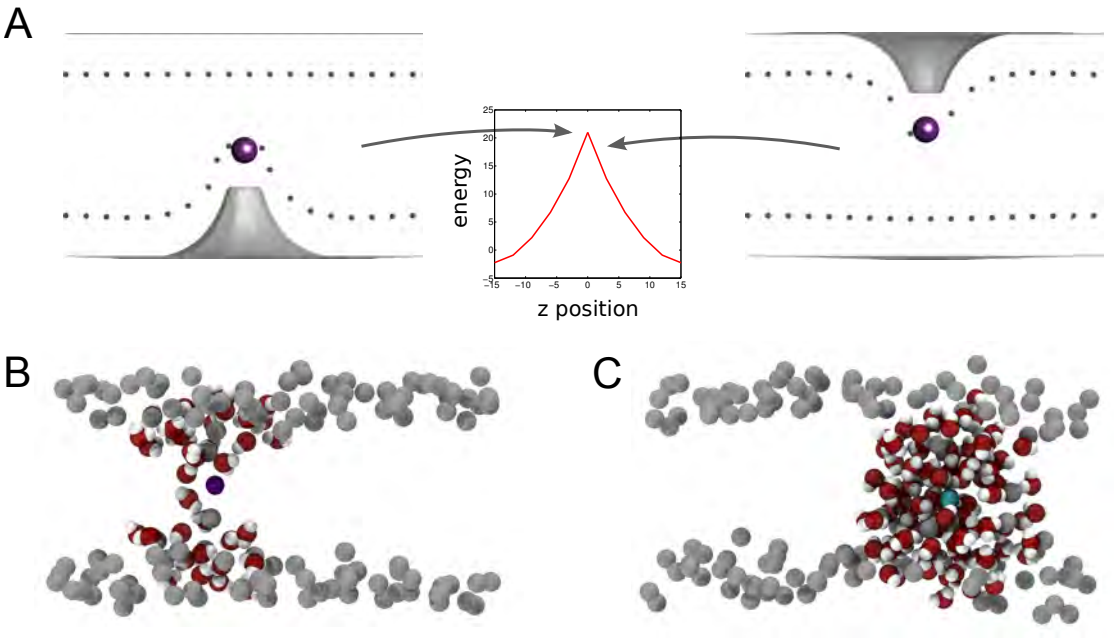

FIGURE 4.5: Comparison of coarse-grained and continuum model treatment of the transition state for ion permeation.

A) Membrane configurations from the continuum model for a K^+ at the center of the membrane (left) and just to the right of the membrane center (right). The relevant portion of the energy profile from Fig. 4.3 is shown in the middle. B) Snapshot from a coarse-grained MARTINI model simulation of a Na^+ ion (purple) restrained at the center of a DHPC bilayer. Polarizable water beads are depicted in red and white; phosphate beads of the membrane are shown in gray. The phosphate beads bend in both the upper and lower leaflets of the membrane to interact with the ion and expose it to water. C) Snapshot from a coarse-grained MARTINI model simulation of a Cl^- ion (cyan) restrained at the center of a DHPC bilayer. The coloring scheme is the same as panel B. The ion-induced pore formed in the membrane is much more profound than the defect induced by Na^+.

and diffuse all the way across to the other leaflet. This step is not sampled in the Allen data, and there is symmetry breaking in the system at $z = 0$ just as in our model for thick membranes. However, for thin membranes (DDPC and DLPC), the atomistic simulations show that the energy profile plateaus at $z = 0$ (inset of Fig. 4.4). Snapshots of these simulations indicate that water penetration and lipid bending occurs into the middle of the bilayer from both leaflets, which restores the symmetry and supports the pore-formation model [125]. Unfortunately, our continuum model does not identify such low energy conformations, and we will return to this in the Discussion.

We decided to carry out coarse-grained MARTINI model simulations of Na^+ and Cl^- embedded at or near the center of membranes to further explore the nature of the transition state. The Marrink group used coarse grained simulations to study the movement of Na^+ and Cl^- through preformed pores in the membrane, and they showed that once a pore is formed Na^+ will permeate small and large pores, but Cl^- will only permeate large pores [136]. Based on this observation, they argue that Cl^- most

likely permeates via a solubility-diffusion mechanism, but cations can permeate via pores, although their simulations did not address ion-induced pores. Our coarse-grained simulations indicate that membrane breakdown occurs when Na^+ or Cl^- is restrained at the center of the membrane for 10 ns (Fig. 4.5B,C). Interestingly, Cl^- elicits much more profound and long-lived membrane breakdown than does Na^+, and this qualitative observation does not fit with the hypothesis that Cl^- permeation only occurs via a solubility-diffusion mechanism [133]. For Na^+ in thicker bilayers, we failed to observe any membrane breakdown over the course of the 60 ns simulation, which supports the solubility-diffusion model for cation permeation of thick bilayers [133].

4.3.5 Large scale membrane deformations are not always observed in coarse-grained simulations

Current computational resources and techniques are making it possible to explore the movement of not only small molecules and ions into membranes, but also small proteins. In recent years, research groups have used computational approaches to explore the insertion and translocation of proteins such as the charged S4 segments from voltage-gated ion channels [8, 9, 37, 102, 104], the HIV Tat protein [141, 142], peptide antibiotics that insert into membranes [143–145]. These studies range from using fully atomistic simulations to continuum methods, and they also range from determining quantitative energies to reporting qualitative observations. Of particular interest are those studies that included a high level of molecular detail yet also perform rigorous free energy calculations, because they have the potential to have predictive power and shape our understanding of membrane related phenomena. However, there is a trade-off between the chemical accuracy of the system and whether the relevant membrane and protein configurations can be adequately sampled.

We carried out extensive coarse-grained simulations on the membrane targeting domain of the rhoptry protein 5 (ROP5) to attempt to calculate its binding energy to the membrane. ROP5 is a rhoptry protein secreted by the pathogen *Toxoplasma gondii* during infection of a host cell. ROP5 associates with the nascent parasitophorous vacuole membrane (PVM), which forms about the parasite. The ability of ROP5 to associate with the PVM is due to a specific arginine-rich domain consisting of three putative alpha-helices, and this domain has been shown to be necessary and sufficient for membrane binding [146]. ROP5 is a potent virulence gene in Toxoplasma [147, 148]. Deletion of this locus renders highly virulent strains of this parasite avirulent. This interaction is hypothesized to be important to the infection process [146], but further experiments are needed to confirm this.

Each helix has a high positive charge content due to the presence of the arginine residues, and they also contain a hydrophobic face making them amphipathic. Deletion of helix 2 in the ROP5 protein most effectively reduced ROP5 binding to the PVM [146] leading to the hypothesis that helix 2 has the highest binding affinity to the membrane. We attempted to test this hypothesis by carrying out separate coarse-grained, MARTINI model MD simulations of helix 1, 2 or 3 in the presence of a homogeneous DPPC bilayer. Following the protocols outlined by the Sansom lab [102, 104], umbrella sampling combined with weighted histogram analysis were used to construct free energy profiles for each helix [132]. In this protocol, the reaction coordinate was chosen as the distance from the center of mass (COM) of the protein to the COM of the membrane. The membrane starts in a flat state that is identical across all simulations, and the protein is translated to many different starting positions across the bilayer prior to minimization and production runs (Fig. 4.6B). The long axis of the helix is initially parallel to the membrane normal with the N-terminus always pointing up. Minimization and equilibration successfully remove any steric clashes between the embedded protein and the lipids, and then production is run for 60 ns per window.

The binding energy for helix 2 is reported in Fig. 4.6B for both a small membrane patch of 128 lipids (red curve) and a large membrane patch with 512 lipids (black curve). As expected, the helix is most stable at the membrane-water interface (-20 Å), where it adopts a conformation with the hydrophobic face buried in the membrane core and the arginine residues exposed to water. Interestingly, the free energy curves are not identical for these two systems. While the energy barrier at the center of the bilayer is nearly identical, the shape of the PMF is quite different between the two lipid patch sizes leading to different estimates of the interfacial binding energy (Fig. 4.6B). We observe that when a small number of lipids are simulated with the helix restrained at 28 Å from the membrane center no large scale membrane bending occurs, and the helix remains largely solvated in water. However, simulations of the same situation with the larger patch size shows a large scale deformation of the bilayer that embeds the hydrophobic residues in the membrane (Fig. 4.7). We performed 3 additional simulations with different random seeds for each system and found this difference in membrane behavior was consistent; the smaller patch never exhibited large scale bending during the length of the entire simulation. Carrying out umbrella sampling in windows separated by 1 Å steps, we found that the small lipid patch does not deform until the helix is restrained 25 Å from the COM of the bilayer. The behavior is in exact agreement with our continuum model shown in Fig. 4.2A in which the membrane undergoes large scale deformations to minimize the energy of the system. In the small patch size simulations, it is not possible for the membrane to undergo such large scale deformations, and the results are necessarily higher energy compared to the larger systems. Thus, it is important to

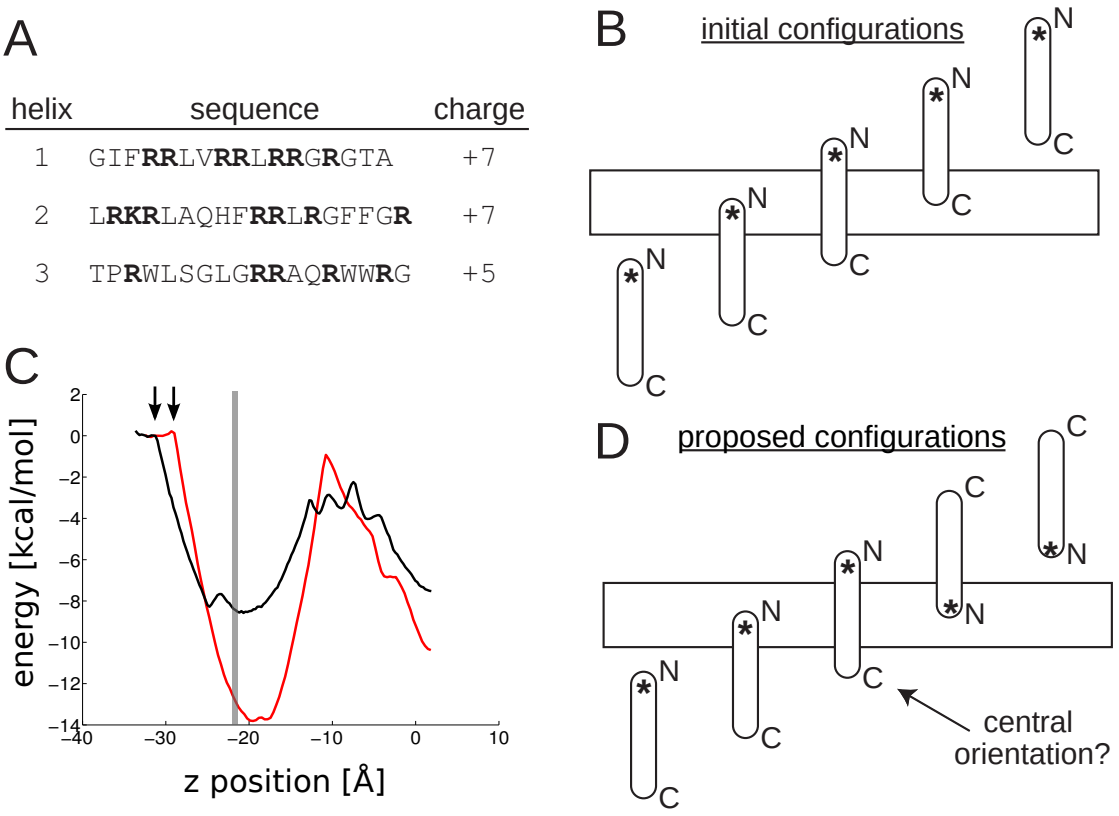

FIGURE 4.6: Free energy of ROP5 binding to a membrane.

A) Sequence of 3 helices from the RAH targeting domain of the ROP5 protein. All sequences are amphipathic, suggesting that they would be stabilized at the membrane-water interface. B) Initial setup for all peptide simulations. Identical copies of helix 2 were translated along the z-axis in 1 Å steps to initiate umbrella sampling simulations. The initial orientation was the same in each umbrella, with the N terminus (starred end) in the positive z-direction. C) The Potential of Mean Force (PMF) for helix 2 translated from the lower bath into the center of the bilayer. The PMFs are flat in water, but exhibit a sharp downward slope at -32 Å (512 patch, black curve) and -28 Å (128 patch, red curve) when the membrane starts to bend to interact with the helix. The large patch is able to bend to reach the helix before the small patch leading to robust differences between the two PMFs. The interfacial region near -20 Å is the most stable position for both simulations, but the binding is predicted to be 5 kcal/mol more stable for the small patch than the large patch. The interface between the headgroup and aqueous environment in the unstrained membrane is indicated by the grey line. D) Symmetry breaking of the helix orientation. Equilibration in each window is as long or longer than typical published protocols; however, we find that this time is insufficient for helix 2 to reorient in the membrane and adopt configurations that must be minimum energy as dictated by symmetry. This poor sampling gives rise to non-symmetric PMF profiles for helices and peptides translated across the entire bilayer, and we suggest using orientations shown in panel D to start with the most favorable terminus in the membrane. *A priori* it is difficult to know which terminus is most stable in the membrane, and the central position must sample both configurations by symmetry arguments.

consider membrane patch size when computing protein binding energies to membranes, and future studies must address this issue in a rigorous manner. One way to remove the dependence on patch size is to define the membrane COM using a small number of lipid molecules within a cutoff radius of the permeating molecule. This definition selects higher energy configurations, but it also uncouples the long wavelength behavior of the membrane to the local changes that accompany permeation. Interestingly, the PMFs in Figure 4.6C suggest that the ROP helix is somewhat stable in a TM region given the low energy at z = 0. When these calculations are carried out with the MARTINI forcefield that does not use long range electrostatics, these highly charged helices are highly unstable in the transmembrane configuration (data not shown).

Finally, simple considerations of symmetry dictate that the free energy profile for protein movement through the bilayer should be symmetric with respect to the origin. Additionally, if the protein, or helix in the cases discussed here, is asymmetric with respect to the N- and C-termini, then its orientation along the z-axis must flip as it moves through the origin (Fig. 4.6D). The system setup we employed (Fig. 4.6B), and used by Sansom and co-workers [102, 104], places the protein with the same orientation for all initial positions. Therefore, if the computed free energy profiles are to be symmetric, the protein must be able to flip its orientation during each window of the simulation. In practice, we do not observe these events for crucial windows in which the helix is buried in the membrane even when we extend our simulations to be 6 times longer than those reported by Bond and Wee (data not shown) [102, 104]. Therefore, even with coarse-grained simulations adequate sampling is still a major hurdle.

4.4 Discussion

Our continuum model produces shapes (Fig. 4.2) and energetics (Fig. 4.4) that are qualitatively consistent with fully atomistic and coarse-grained simulations of ion penetration into membranes. This connection is encouraging since ion, ionophore and peptide permeation across membranes is of extreme interest from both a basic biological stand point and a pharmacological perspective. Computational approaches to understanding these phenomena are needed to gain atomic level insight and provide predictive power. One advantage of a continuum model is that the reduction of the system size, by treating the membrane and water as a continuum, leads to energy calculations that are thousands of times faster than corresponding atomistic simulations [37]. Another benefit of continuum approaches is that it is very easy to determine the contribution of each energy term in the model to the total energetics of the system. For instance, the membrane bending energy is easily computed from our model, but is quite hard to accurately calculate

from averaging over membrane configurations in an atomistic simulation. Along these lines, the Weinstein lab has observed similar qualitative agreement between MD and continuum results, and they have implemented a method that combines both approaches to better understand the energetics of their membrane protein systems [24].

Our model predicts that both cations and anions are stabilized in the headgroup region, which is in agreement with recent experiments [140]. Our model has very little chemical detail, and the degree of stabilization in the headgroup may be overstated. While atomistic MD simulations of guanidinium predicted similar stabilization in PC headgroups, guanidinium has a much larger nonpolar surface area than K^+ and Cl^-, and in the near future we intend to tune variables in our continuum model to more closely match results from chemically accurate simulations. Unfortunately, molecular dynamics simulations fail to reproduce the experimental finding that anions are stable in the headgroup and that anions permeate bilayers more readily than cations [135, 137]. It is possible that the higher anion permeation barriers compared to cations is due to poor sampling of the true transition state, but it is also possible that these differences are inherent in the forcefields. These fundamental issues must be worked out before attempting to fit our continuum model to energy profiles produced from MD simulations.

The nature of the transition state for ion permeation is poorly defined and poorly sampled in atomistic MD simulations, but understanding the molecular details of the ion passing from one leaflet to the other is crucial for making connections to classical pore formation or solubility diffusion models of permeation. As we move ions through the membrane, our continuum model exhibits a bifurcation point at the origin where the ion discontinuously switches from one leaflet to the other. The McCammon lab observed very similar bistable configurations in their atomistic simulations of Na^+ and Cl^- permeation across a DMPC bilayer [137]. When the ions reach the center of the bilayer, the finger of water connecting the ion to one side of the membrane quickly retracts and a new finger of water from the opposite side appears. This switching is rare, but when it occurs it happens very fast - on the nanosecond time scale [137]. The degeneracy of these two configurations when the ion is at the center of the bilayer highlights the fact that the z position does not fully describe the reaction, and the transition state occurs along other degrees of freedom. Not surprisingly, it was shown that PMFs along z exhibit the greatest error at this critical position [137]. In order to understand ion permeation, the details and energetics must be explored along the relevant reaction coordinate orthogonal to the z-axis when the ion is at the origin. It is likely that the transition is a non-equilibrium event in which ballistic ions partition into and move through the hydrophobic core on a time scale that is too fast for the membrane to reorganize and achieve equilibrium. If this is the case, our model will fail, and we must include dynamics to attempt to understand these transitions.

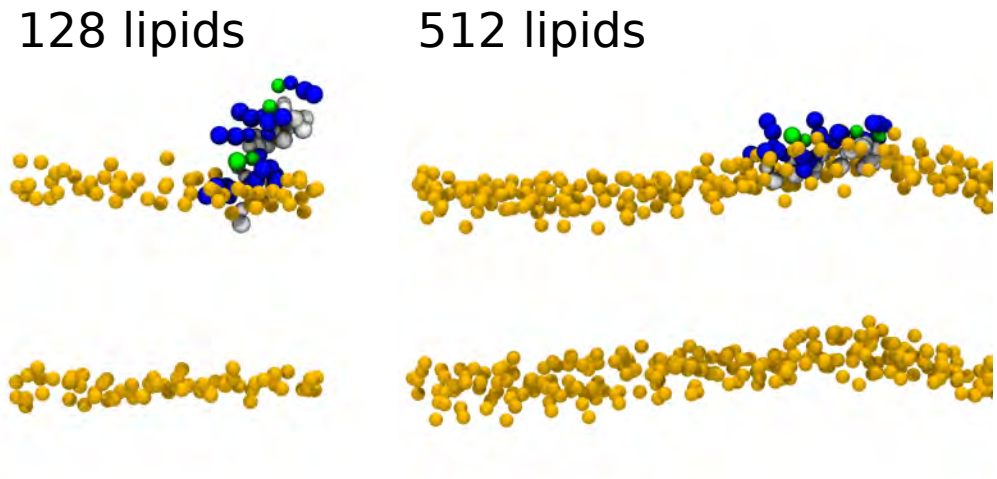

FIGURE 4.7: Large scale deformations are observed in large coarse-grained simulations but not small systems.

When helix 2 from the ROP5 protein is restrained -30 Å from the center of a DPPC bilayer, a large membrane patch is able to undergo a large scale conformational change to allow the helix to go completely interfacial (right), while the small patch is unable to accommodate such a bending mode (left). These differences in system size give rise to differences in the energetics of helix association with the membrane as seen in Fig. 4.6C.

Perhaps our most important observation is that computed energy profiles for ion and peptide association with the membrane depend on the size of the membrane patch. Advances in computer hardware and computational methods are making it possible to quantitatively probe membrane interactions with peptides and small proteins using molecular simulation. However, our continuum model shows that if the membrane patch is large enough low energy, long wavelength deformations in the bilayer allow for protein-membrane interactions over long distances [37], and this is highlighted in our qualitative coarse grained simulations with ROP5 (Fig. 4.7). The underlying free energy profiles are quite different for the small system and the big system (Fig. 4.6C), which will make it difficult to compare results between studies unless system size is taken into account. Moreover, it is not clear which simulation setup is most appropriate for comparing theory to experimental binding energy values.

While our continuum model does a good job of describing large scale deformations that are difficult to capture in molecular simulations, it does not capture small length scales changes at the single lipid level. Kim and co-workers recently described the membrane deformation profile around the membrane spanning antibiotic peptide gramicidin A [149]. They showed that the membrane surface undergoes non-monotonic changes in height in the first few lipid shells surrounding the peptide. Our experience leads us

to agree with their conclusion that such solutions are not possible given the class of elastic models we are using. The impact that these undulations play on membrane protein function and system energetics must be further explored, and it may take more sophisticated continuum models to describe membrane structure at this level of detail.

One of our primary goals for this study was to predict kinetic rates of ion and small molecule permeation across membranes using our continuum model, but our inability to accurately describe the transition states has made this impossible. In our opinion, nearly all computational studies of ion and small protein movement across bilayers poorly describe the transition states where the molecules are near the center of the bilayer. Future studies must employ more sophisticated reaction coordinates to better sample the point at which molecules partition into the hydrocarbon core, or the point at which molecules rapidly switch between opposite leaflets. Additionally, peptide binding studies must more carefully treat the orientation of the peptide in the membrane when it is near the center of the bilayer as highlighted in Fig. 4.6D. Our continuum model does not produce minimum energy configurations in which the leaflets bend from both sides of the membrane producing pore like structures. These topological transformations are most likely difficult to obtain using our Monge gauge representation of the membrane, but we hope to incorporate such changes in future studies. We also hope to extend our calculations into the time regime, which may be needed if permeation proves to be a non-equilibrium phenomenon. Finally, we would like to use our model to describe charged peptide transport, which would require coupling in conformational changes in the permeating molecule, which has been successfully done for neutral molecules [150].

Chapter 5

APBSmem: A Graphical Interface for Electrostatic Calculations at the Membrane

Electrostatics are one of the primary determinants of molecular interactions. They are intricately involved in the folding of proteins, protein-protein interactions, and they facilitate protein-DNA and protein-ligand binding. Numerically solving the Poisson-Boltzmann equation is a popular method for evaluating the electrostatic properties of biological systems. In this chapter we present a method for using the Adaptive Poisson-Boltzmann Solver (APBS) as a back-end for membrane protein calculations, which can be technically difficult and time-intensive to configure properly. These calculations are an essential component of the results shown in Chapters 2, 3, and 4. A Java-based graphical user interface is also presented with three relevant test systems that highlight the different quantities of interest that can be calculated. [1]

[1] This chapter is adapted from: K M Callenberg, O P Choudhary, G L DeForest, D W Gohara, N A Baker, and M Grabe. APBSmem: a graphical interface for electrostatic calculations at the membrane. PloS ONE, 5(9):e12722, 2010 [29].

5.1 Introduction

The relationship between the electric field and the charge in a system is determined by Maxwell's equations; however, several factors contribute to making these equations difficult to solve in a heterogeneous, condensed phase. The most popular method for carrying out electrostatic calculations in a biological setting is to solve the Poisson-Boltzmann (PB) equation. Starting from a known protein structure, this method treats the protein and water as distinct dielectric environments, and the charges on the protein give rise to the electric field. Additionally, PB theory implicitly accounts for counter-ions in solution via a non-linear term that depends on the bulk counter-ion concentration and the electrostatic potential. The PB equation for a one-to-one electrolyte solution is:

$$-\nabla \cdot [\epsilon(\vec{r})\nabla\phi(\vec{r})] + \overline{\kappa}^2(\vec{r})\ sinh\,[\phi(\vec{r})] = \frac{e}{k_B T}\ 4\pi\rho(\vec{r}), \tag{5.1}$$

where $\phi = e\Phi/k_B T$ is the reduced electrostatic potential and Φ is the electrostatic potential, $\overline{\kappa}^2$ is the Debye-Hückel screening parameter, which accounts for ionic shielding, ϵ is the dielectric constant for each of the distinct microscopic regimes in the system, and ρ is the density of charge within the protein moiety. Since the 1980s, researchers have studied the electrostatic properties of protein and nucleic acid systems by numerically solving the PB equation using finite difference and finite element methods [151–154]. Today, there are several popular software packages available to perform PB calculations such as DelPhi [155], the Adaptive Poisson-Boltzmann Solver (APBS) [73], MIBPB [156], ZAP [157], and the PBEQ module in CHARMM [158]. Unfortunately, there is a dearth of programs that allow researchers to carry out these calculations at or near a membrane. Nonetheless, over the last two decades the number of high-resolution membrane protein structures has dramatically increased. The membrane has several unique electrical properties. For instance, the core of the membrane is extremely hydrophobic giving rise to a desolvation penalty for moving charged molecules into this region. This property is essential to the membrane's ability to control the flow of materials into and out of the cell. Additionally, most cells have a substantial membrane potential that coordinates the action of voltage-dependent membrane proteins such as voltage-gated ion channels. Without including the effects of the membrane dielectric and the transmembrane potential, there is a huge class of molecules whose electrical properties cannot easily be explored.

Groups have carried out simulations using several different levels of theory to include the effects of the membrane such as fully atomistic calculations (for an incomplete list of references see [70, 159–164]), implicit membrane calculations using Generalized Born models (for an incomplete list see [45, 82, 165–175]), and continuum approaches

employing the PB equation (for an incomplete list see [61, 114, 176–185]); however, all of these studies require the user to have a high level of computational sophistication as highlighted by the relatively few papers from non-computational laboratories. Thus, it is desirable to have a program that removes many of the technical and bookkeeping aspects from these calculations. Toward this end, very recently, an online web server was created to facilitate PB calculations on membrane proteins using the PBEQ module [186], and here, we present our program, APBSmem, which combines an easy to use interface with APBS to allow non-experts to calculate the electrostatic properties of membrane proteins. APBSmem can be downloaded, easily installed, and run locally on Windows, Mac, and Linux platforms. APBSmem has several pull down templates that allow researchers to carry out specific membrane related calculations, and it has a built-in graphical window that provides quick visual feedback to make sure that the system is set up correctly and to view results.

5.2 Methods

5.2.1 User interface

Though the majority of the calculations described here may be performed using APBS input files, keeping track of the files and parameters can become quite difficult. To improve this process we built a Java-based GUI that writes the input files and runs the calculations (Figure 5.1). The GUI has an embedded Jmol [187] viewer that allows users to visualize the protein-membrane system and the electrostatic potential. Here we explain the necessary parameters and use of the interface in a step-by-step fashion.

Calculation Type. To perform a calculation, the user first selects a type (Protein Solvation, Ion Solvation, or Gating Charge) from the drop down menu. Each type is described in more detail in the case studies below. The user then selects coordinate files, in PQR format, for all of the protein configurations of interest. PQR files contain the atomic positions of all of the atoms in the system in addition to their charge and radii. PQR files can be generated from PDB files with the PDB2PQR tool [188], which allows the user to choose from several commonly used charge and radii parameter sets: PARSE [44], CHARMM27 [189], Swanson [190], AMBER99 [191], along with several other sets and user defined values. This choice is crucial since calculations can be sensitive to the parameter set [192] especially when performing solvation energy calculations. File locations may be entered manually or found and selected from the filesystem with the Browse button. At present, APBSmem does not allow the spatial orientation and placement of the protein to be altered once read in through the GUI, and external

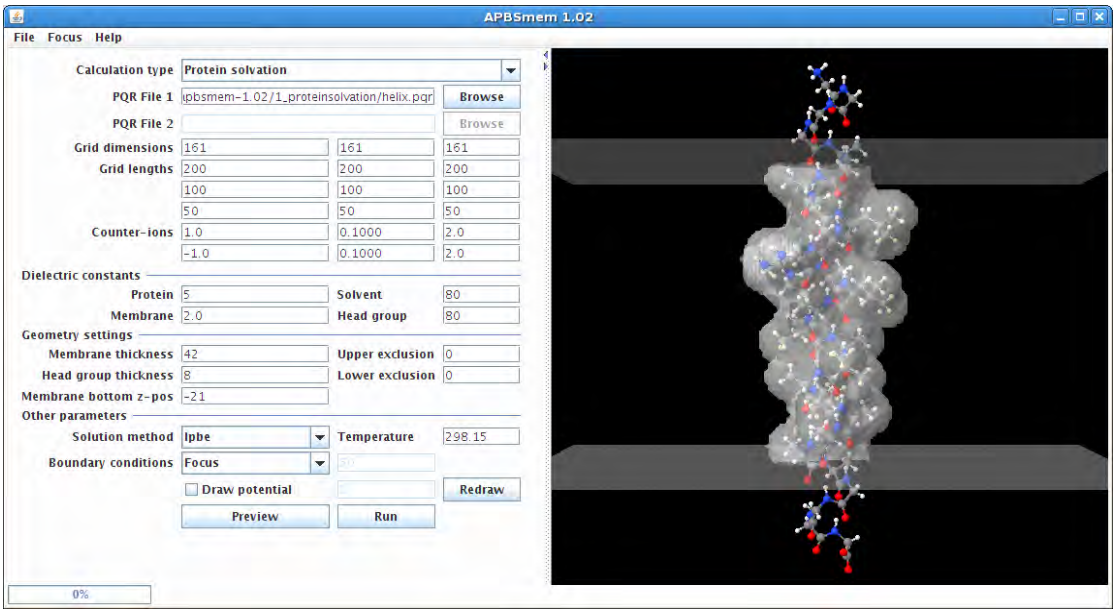

FIGURE 5.1: A screenshot of the user interface.

Parameters pertaining to the calculation are entered in the field on the left, and the molecule and membrane can be viewed in the embedded Jmol viewer on the right. Pictured here is the membrane-embedded single transmembrane helix used for the calculations in CASE I.

software must be employed if a different orientation is desired. For Protein Solvation calculations, the user should provide a coordinate file with only the membrane protein. Ion Solvation calculations require a PQR file with only the protein and a PQR file with only the ion. Two files corresponding to an open and a closed channel are needed in the case of a Gating Charge calculation.

Grid Spacing. Next, the user must specify the desired level of discretization, which is related to the fidelity with which the underlying equations will be solved. It is necessary to apply the appropriate boundary conditions far from the protein to accurately solve electrostatics calculations, and this requires large grid lengths to remain computationally tractable. However, coarse discretization does not capture the correct electrostatic behavior near the protein, where small grid spacing is needed. A technique known as focusing is employed to rectify this problem by solving the equations in a series of steps starting at the largest length scale and focusing into the smallest length scale [155]. When using multiple levels of focusing, the user can set the desired level in the Focus menu to enable fields for additional grid lengths.

With any numeric calculation, the accuracy of the solution is directly related to the degree of discretization. It is important to check the convergence properties of your solution. This is typically done by recalculating with increasing numbers of grid points without changing any of the other parameters. The exact convergence properties depend

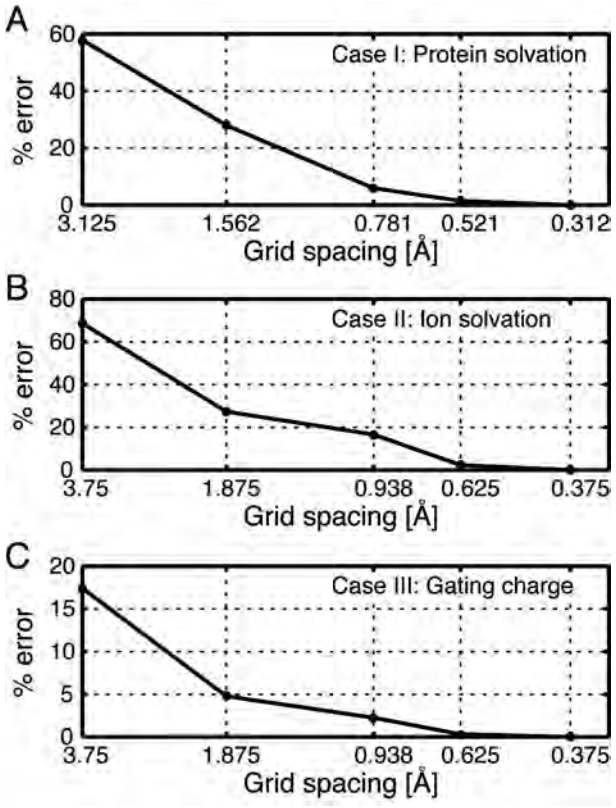

FIGURE 5.2: Convergence properties of test cases I-III.

We computed the absolute value of the percent error, $100 \cdot |(E(\Delta x) - E(\Delta x_{finest}))/E(\Delta x_{finest})|$, for each test case using a number of different discretization values. All energies are reported with respect to the solution value at the finest level of discretization, Δx_{finest}, which was 0.312 Å in test Case I and 0.375 Å in Cases II and III. Values along the x-axis are spaced using a log base 2 scale. In all graphs, the number of grid points used to achieve the grid spacing on the x-axis was 17, 33, 65, 97, 129, and 161 (Δx_{finest}). (A) Convergence of the protein solvation energy, Case I. A grid spacing of 0.512 Å gives a solution 1.5% of the highest resolution value. The energy values smoothly converge as the resolution increases. (B) Convergence of the ion solvation energy, Case II. The error monotonically decreases as the level of discretization increases. At $\Delta x = 0.625$ Å , the energy value is within 2.5% of the final value. (C) Convergence of the gating charge energy in the closed state, Case III. Rather than report the gating charge, here we plot the energy of the closed state. This method converges much more quickly than the other Cases since it does not involve Born Self energy terms. The energy at the second finest level is 0.33% of the value at the finest level. Even at a grid spacing of $\Delta x = 0.938$ Å the computed energy is within 3% of the best value. In all cases, the convergence properties and the accuracy of the solutions depend critically on the refinement of the protein surface boundaries. Here we use the spl2 method for charge mapping in APBS, which gives very desirable convergence properties.

on the numeric algorithm and the details of the system. In Figure 5.2, we calculated the convergence for each test case in the Results section. However, all systems behave differently, and users should not assume that discretization schemes that give accurate results here will also give accurate values for other protein-membrane systems.

Dielectric Parameters. In continuum electrostatics, different regions of the system

are defined by unique dielectric values. These values are related to the polarizability of each region in response to an applied electric field. The protein dielectric value is assigned to points within the protein's solvent accessible surface. All points outside the protein, but within the membrane region defined by the geometry settings, are assigned a dielectric value corresponding to the membrane. While the core of the membrane often has a very low dielectric value, the head group region may be characterized by a much higher value. If desired, this physical feature can be included in calculations by increasing the default head group thickness and setting the head group dielectric value. All other points in the system are assigned the solvent dielectric value.

Proteins are heterogeneous, and it is not always appropriate to describe the entire molecule with a single uniform dielectric value [41]. Nonetheless, uniformity is a common assumption of PB solvers. Experiments indicate that the protein interior is modeled best by dielectric values between 2 and 20 [42]. With this in mind, we recommend that researchers test the robustness of their results by repeating calculations with several different dielectric constant values within this range.

Boundary Conditions. Several options are offered for Dirichlet boundary conditions when solving the PB equation in APBS. The user may set all boundaries to zero, use a single Debye-Hückel model, multiple Debye-Hückel model, or focusing, in which the boundaries are determined by a previous calculation. When the Gating Charge calculation type is chosen, the boundary condition is set to impose a range of membrane potentials across the membrane as described in Case III. The user provides a membrane potential value in milliVolts, V_{in}, and the interface performs a sweep of calculations from $-|V_{in}|$ to $+|V_{in}|$ to determine the valence of the gating motion. At present, calculations with a membrane potential are only carried out in the linearized limit of Eq. 5.1. Additionally, application of the boundary conditions ignores differences between the dielectric values of the head group and the membrane core, which has been included in a recent study [193].

Protein Surface Representation. An accurate representation of the protein surface is important in constructing the dielectric and ion-accessibility maps. A probe-based dielectric function is used to construct the protein surface in APBS. The solvent probe radius specifies the size of water spheres for the determination of the solvent space and is typically set to 1.4 Å for water. The surface sphere density determines the resolution at which this boundary is calculated and is typically set to 10 grid points/Å^2.

System Geometry. The system geometry parameters determine the shape and location of the membrane. The membrane thickness and vertical position should be adjusted for the protein of interest so that the bilayer interfaces with the protein as expected. It is difficult to determine this placement, and it is an ongoing area of research in the Grabe

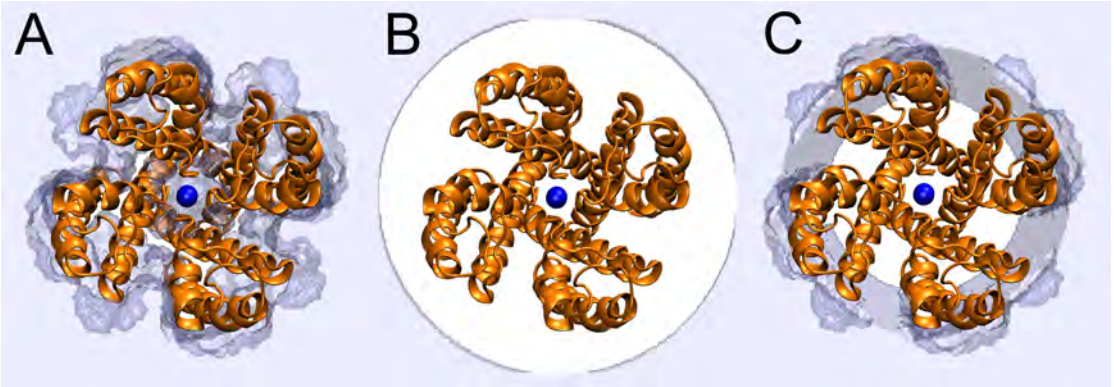

FIGURE 5.3: Top view of the KcsA channel (green) and the $\epsilon = 2.01$ isocontour highlighting the membrane interface (gray).

The K^+ ion in the center of the channel is shown in blue. (A) When the membrane is not excluded from the channel pore, we observe that membrane is added to the pore region. (B) With the exclusion radii set too high at 28 Å, there are large gaps of water between the outer membrane and the protein. (C) The channel should be clear of membrane and the membrane should fit snugly around the outside of the protein as shown here. Membrane exclusion radii are 24 Å and 16 Å at the top and bottom of the channel, respectively.

lab [22]. In practice, this placement is often done ad hoc based on the location of the hydrophobic residues making up the membrane spanning region. A better alternative is to first estimate the orientation of the membrane protein and extent of the membrane spanning region by using the Orientations of Proteins in Membranes database [21]. A second point of concern is that ion channels and transporters often have hydrophilic, water-filled cavities essential for transport. Users must employ the interface exclusion radii to prevent APBSmem from rewriting these cavities as membrane. These radii should be adjusted so that central cavities, if present, are filled with water and the membrane is arranged flush with the outside of the protein. We intend to provide automated cavity detection in future releases. Figure 5.3 compares correct and incorrect configurations of the membrane geometry with the KcsA potassium channel.

System Preview. After the user has entered parameters for the dielectric environment and membrane geometry, the Preview button can be used to visualize the system. This Preview action performs a quick "dummy" calculation with coarse grid dimensions to generate the numeric representation of the membrane and display it graphically. If the system and parameters appear to be correct, the user can click Run to perform the calculation with APBS. When the calculations have completed, the total energy is given in kJ/mol, kcal/mol and k_BT, and the most focused dielectric map of the membrane is displayed in the Jmol panel. The electrostatic potential may also be viewed in the Jmol panel by selecting the Draw Potential option. The user provides an isocontour value of interest and the interface displays the positive (red) and negative (blue) surfaces over the protein. The exterior bulk and cavity (if any) at the interior of the protein

are modeled into APBS as coefficient maps (openDX- format). These maps include dielectric maps (diel), ion-accessibility coefficient maps (kappa) and charge distribution maps (charge) for different regions of the protein-membrane complex. All input and output files, including the potential and DX maps are saved for later use and reference.

5.2.2 Membrane potential boundary conditions

In a typical cell, electrogenic transporters create a difference between the electrical potential inside the cell, V_{in}, and outside the cell, V_{out}. A small violation in electroneutrality near the membrane gives rise to this potential difference; however, more than a Debye length from the membrane, electroneutrality is restored. It is possible to model this behavior with the Poisson-Boltzmann equation as outlined by Roux in his seminal work on this topic [13]. Most researchers will want to compute the membrane potential in the absence of protein charges to understand the profile across the protein, and in some cases, they will be interested in computing the interaction energy of the membrane electric field with the charges on the protein. The field due to the protein charges and the membrane potential are only separable when solving the linearized form of the equation. Thus, in order to be self consistent, APBSmem only solves the linearized Poisson-Boltzmann equation when employing membrane potential boundary conditions. In future releases, we will extend this to the full non-linear equation. The presentation in this section and the next largely follows the supporting text found in Grabe et al. [114], but the essence is similar to Roux's [13]. We start by rewriting Eq. 5.1 in the linearized form:

$$-\nabla\cdot[\epsilon(\vec{r})\nabla\phi(\vec{r})]+\overline{\kappa}^2(\vec{r})\phi(\vec{r})=\frac{e}{k_BT}\,4\pi\rho(\vec{r}), \tag{5.2}$$

However, this equation does not satisfy the asymptotic boundary condition: $\Phi(x,y,z\rightarrow -\infty)\rightarrow V_{in}$. This oversight can be corrected by adding a constant term to the equation for all positions in the inner solution space:

$$-\nabla\cdot[\epsilon(\vec{r})\nabla\phi(\vec{r})]+\overline{\kappa}^2(\vec{r})\left(\phi(\vec{r})-f(\vec{r})\frac{e}{kT}V_{in}\right)=\frac{e4\pi\rho(\vec{r})}{k_BT}\,, \tag{5.3}$$

where $f(\vec{r})$ is 1 for all points in the inner solution space and zero otherwise (see Figure 5.4). Now far from the protein where ϕ is no longer changing, $\Phi(x,y,z\rightarrow -\infty)\rightarrow V_{in}$ as desired. Eq. 5.3 can be rewritten as:

$$-\nabla\cdot[\epsilon(\vec{r})\nabla\phi(\vec{r})]+\overline{\kappa}^2(\vec{r})\phi(\vec{r})=\frac{e4\pi}{k_BT}\,\left(\rho(\vec{r})+\frac{\overline{\kappa}^2V_{in}}{4\pi}f(\vec{r})\right). \tag{5.4}$$

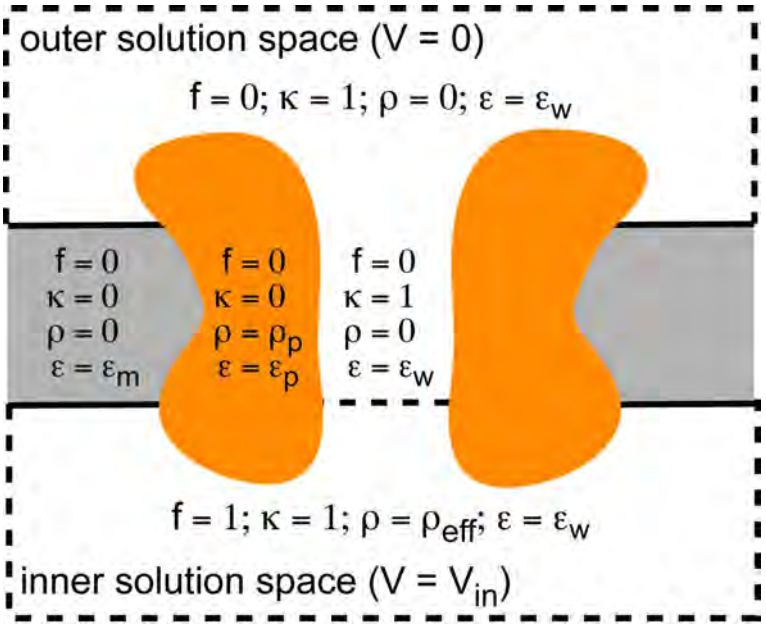

FIGURE 5.4: A cartoon representation of the distinct dielectric environments in each calculation.

The orange regions represent protein, the gray membrane, and all white areas indicate water. The inner solution space at the bottom is assigned a voltage of V_{in}, and correspondingly an effective charge density ρ_{eff} is assigned and a value of one for the variable f. The water in the center of the channel is assigned values for ρ and f that correspond to the outer solution space. The lower z value of the membrane (dashed line) separates the inner and outer solution spaces. In the gray region, κ and ϵ are set to 0 and ϵ_m, respectively, to mimic the membrane.

Thus, the modified Poisson-Boltzmann equation above takes the form of Eq. 5.2 with the membrane potential arising from a term that looks like a uniform source charge. The spatial dependence of $\overline{\kappa}$ is carried by $f(\vec{r})$ on the right hand side. Since Eq. 5.4 is linear, it is possible to separate the total reduced electrostatic potential, ϕ, into contributions from the membrane potential, ϕ^m, and contributions from the protein, ϕ^m, as $\phi = \phi^p + \phi^m$. Each field is the solution to corresponding equations as shown:

$$\begin{aligned} -\nabla \cdot [\epsilon(\vec{r})\nabla\phi^p(\vec{r})] + \overline{\kappa}^2(\vec{r})\phi^p(\vec{r}) &= \tfrac{e}{k_B T}\, 4\pi\rho(\vec{r}), \\ -\nabla \cdot [\epsilon(\vec{r})\nabla\phi^m(\vec{r})] + \overline{\kappa}^2(\vec{r})\phi^m(\vec{r}) &= \tfrac{e}{k_B T}\, 4\pi \tfrac{\overline{\kappa}^2 V_{in}}{4\pi} f(\vec{r}). \end{aligned} \tag{5.5}$$

Far away from the protein, ϕ^p approaches zero. Poisson-Boltzmann solvers typically set zero boundary conditions at the outer boundary to account for this behavior, or they use some asymptotic approximation to the field based on the protein's total charge. In the case of a membrane potential, the behavior of ϕ^m far from the membrane protein is required so that far field boundary conditions can be imposed on the system.

ϕ^m on the boundary is determined by considering a planar slab of low-dielectric material with symmetric electrolyte solution in the half-spaces above and below the slab. This

follows the work of Roux with a slight change in geometry [13]. By symmetry $\phi^m(\vec{r}) = \phi(z)$, and we assign $z = 0$ to the center of the membrane. The slab has a length L, and there are three distinct regions of space: $z > L/2$ (out); $L/2 \geq z \geq -L/2$ (membrane); $z < -L/2$ (in). The dielectric of water is ϵ_w, and the dielectric constant of the membrane is assigned ϵ_m. We assume that ions cannot enter the membrane so $\overline{\kappa}$ is set to 0 in this region, while the inner and outer spaces have the same value of the screening parameter. According to Eq. 5.5 the ϕ_m satisfies the following equations in each region

$$\begin{aligned} &-\epsilon_w \partial_z^2 \phi_1^m(z) + \overline{\kappa}^2 \phi_1^m(z) = 0 && (outer) \\ &-\epsilon_m \partial_z^2 \phi_2^m(z) = 0 && (membrane) \\ &-\epsilon_w \partial_z^2 \phi_3^m(z) + \overline{\kappa}^2 (\phi_3^m(z) - \tfrac{e}{k_B T} V_{in}) = 0. && (inner) \end{aligned} \tag{5.6}$$

From elementary electrostatics, we know that the potential is continuous at the membrane boundaries but the z-component of the electric field is discontinuous due to the jump in dielectric value:

$$\begin{aligned} &\phi_3^m(-\tfrac{L}{2}) = \phi_2^m(-\tfrac{L}{2}); && \epsilon_w \partial_z \phi_3^m|_{-\frac{L}{2}} = \epsilon_m \partial_z \phi_2^m|_{-\frac{L}{2}} \\ &\phi_2^m(\tfrac{L}{2}) = \phi_1^m(\tfrac{L}{2}); && \epsilon_m \partial_z \phi_2^m|_{\frac{L}{2}} = \epsilon_w \partial_z \phi_1^m|_{\frac{L}{2}}. \end{aligned} \tag{5.7}$$

The potential profile can be determined from Eqs. 5.6 and 5.7:

$$\begin{aligned} \phi_1^m(z) &= \tfrac{e}{k_B T} V_{in} \tfrac{1}{\frac{\epsilon_w}{\epsilon_m}\kappa L + 2} e^{\kappa(L/2 - z)} && (outer) \\ \phi_2^m(z) &= \tfrac{e}{k_B T} V_{in} \left(\tfrac{1}{2} - \tfrac{1}{\frac{\epsilon_w}{\epsilon_m}\kappa L + 2} \tfrac{\epsilon_w}{\epsilon_m} \kappa z \right) && (membrane) \\ \phi_3^m(z) &= \tfrac{e}{k_B T} V_{in} \left(1 - \tfrac{1}{\frac{\epsilon_w}{\epsilon_m}\kappa L + 2} e^{\kappa(z + L/2)} \right), && (inner) \end{aligned} \tag{5.8}$$

where $\overline{\kappa}^2 \equiv \epsilon_w \kappa^2$. When membrane potential calculations are performed, Eq. 5.8 is used to set ϕ^m on the domain boundary. This requires first providing the z-position of the top and bottom of the membrane and the dielectric constants of the membrane and water.

5.2.3 Addition of the membrane

The influence of the membrane must be included in the calculation. Based on the structure file provided, the program calls on APBS to generate dielectric (ϵ), charge (ρ), and ion-accessibility maps (κ) of the molecule as if it were in solution. The protein dielectric value can be set to any value, and the method for delineating the solvent

boundary is also configurable. At present, the GUI allows up to 2 levels of focusing, which corresponds to 3 sets of maps produced at this initial stage. Maps are then modified to add the presence of a low-dielectric slab acting as a surrogate membrane. APBS is run with the finite differencing scheme option; therefore, all map points are associated with a regular grid in 3-space. Next, the initial maps are read by a second routine, and the numeric values of points on the grid are modified based on the spatial position and the user-defined placement of the membrane. The program iterates over every grid position and evaluates each position in the following order:

1) Determine if the point is inside the provided protein. If the initial dielectric map value equals ϵ_p, the point is located within the protein. Dielectric map values are not changed for these points.

2) Determine if the point is inside the membrane. If the point does not fall within the protein, it falls within the z-extent of the membrane determined by z_{upper} and z_{lower}, and it falls outside the cylinder described by the exclusion radii, the value of the dielectric map is set to ϵ_m, the ion-accessibility is set to zero, and the charge map is not changed.

3) Determine if the point is in the inner solution space. If the point is below the membrane and the ion-accessibility is not zero, then the neutral charge map is modified for the calculations of ϕ^m. The value assigned to the charge map position is determined from Eq. 5.5 (bottom equation). The effective charge density, ρ_{eff}, follows from the right hand sides of the upper and lower equations:

$$\frac{e}{k_B T} 4\pi\rho_{eff} = \frac{e}{k_B T} 4\pi \frac{\overline{\kappa}^2 V_{in}}{4\pi}$$

The text maps are written in terms of the number density, $n_{eff} = \rho_{eff}/e$, and using this along with the definition of the Debye length we arrive at the modified value for the charge map

$$n_{eff} = \epsilon_w \frac{\kappa^2 V_{in}}{4\pi e} = \frac{\epsilon_w V_{in}}{4\pi e} \left(\frac{8\pi e^2 \; N_a I}{\epsilon_w \; k_B T} \right),$$

where I is the molar concentration of one of the salt species (assumed balanced) and N_a is Avogodro's number. The Debye constant above is twice the value that can be found on page 497 of Jackson's Classical Electrodynamics (Second Edition) [194], since we assume that there are mobile cationic and anionic species, not just one mobile species. Simplifying this equation we arrive at:

$$n_{eff} = 0.001204428\ I\ u_{in},$$

where $u_{in} = eV_{in}/k_BT$ is the reduced inner potential and the counter-ion concentration is given in moles per liter. The effective number density is now in inverse Ångstroms cubed, which is consistent with the APBS solver.

Results

APBSmem was developed in Java and requires Java Runtime Environment 5.0 or later and APBS version 1.2.0 or later which can be downloaded from http://java.sun.com/ and http://www.poissonboltzmann.org/, respectively. The program can be run from the command-line using `java -jar apbsmem.jar`. Three case studies are presented here to demonstrate potential calculations. All files necessary to perform these calculations are packaged with the APBSmem program.

5.2.4 CASE I: Protein Solvation

The cell membrane is composed of lipid molecules and hosts membrane proteins which account for a third of all proteins in a cell. The hydrophobic core of the membrane provides a dielectric barrier against polar and charged molecules. The transmembrane segments of membrane proteins are therefore largely composed of hydrophobic residues; but charged and polar residues are also sometimes present, so it is natural to ask how these charged residues can be stably accomodated in the membrane. Choe *et al.* [22] investigated this question using continuum electrostatics with APBS. Here we revisit this problem to demonstrate the applicability of our graphical interface, and we do this by calculating the solvation energy required to insert a charged helix into the membrane. The total energy of a simple α-helix in bulk water (Figure 5.5B) is first computed and then subtracted from the total energy of the helix embedded in the membrane (Figure 5.5A).

Using APBSmem to compute the protein solvation energy requires the protein to be read in as PQR file 1. The system of interest for this case study is an α-helix composed of 27 residues, aligned along the z-axis and centered at the origin. The helix is composed of nonpolar hydrophobic residues with the exception of a charged arginine at the center. The protein solvation energy calculation is performed on a 161^3 grid using two levels of focusing from a cube with side length 200 Å to a cube of side length 50 Å. The bathing solution contains 0.1 M symmetric monovalent salt with 2 Å probe radii. The protein

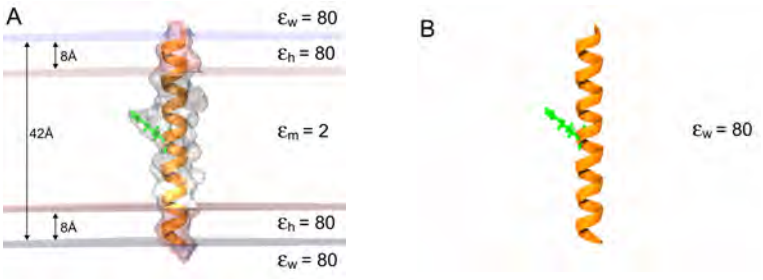

FIGURE 5.5: States used to compute protein solvation energies.

(A) The helix (orange) is pictured embedded in the membrane, which is delineated by the upper blue and lower gray lines. The membrane core between the two red lines is assigned a dielectric value $\epsilon_m = 2$. A headgroup region of 8 Å is indicated between the water and membrane core. Bulk water above and below the membrane is assigned a dielectric value of $\epsilon_w = 80$. (B) The helix in the bulk water ($\epsilon_w = 80$) in the absence of the membrane. The helix carries one charged residue (Arg14) shown in green in (A) and (B). The protein solvation energy is calculated by computing the total electrostatic energy of systems A and B and then calculating the quantity: $E_{total} = E_A - E_B$. Images rendered with VMD [195].

is assigned a dielectric value of $\epsilon_p = 5$, bulk water is assigned a value of $\epsilon_w = 80$, and membrane is assigned a dielectric of $\epsilon_m = 2$. The head group is modeled as a region of high dielectric, $\epsilon_h = 80$, with a thickness of 8 Å. Calculations are carried out with the linearized PB equation with a solvent probe radius of 1.4 AA, a surface sphere density of 10 gridpoints/Å^2 and a temperature of 298.15 K. The total membrane thickness is 42 Å running from z = -21 Å to z = +21 Å. The upper and lower exclusion radii are set to 0 Å since there is no pore. Parameters are summarized in Table 5.1.

For this system, we obtain a protein solvation energy of 28 kcal/mol, and Figure 5.2A indicates good convergence with grid spacing smaller than 0.781 Å at the finest level. While this energy is large, it is greatly reduced when nonpolar energies are considered. Additionally, a large component of this energy is the cost of inserting the charged arginine. If the arginine is replaced with an alanine, the solvation energy drops to 4 kcal/mol. It has been shown that the electrostatic component of the membrane deformation energy can be considerably reduced by allowing the membrane to bend around the charged residue in the core of the membrane [22]. We will incorporate membrane bending and nonpolar energy terms in future releases of APBSmem.

5.2.5 CASE II: Ion Solvation

The primary role of ion channels is to facilitate the movement of ions across the dielectric barrier imposed by the lipid bilayer. The hydrated ions in the bulk water are essentially stripped of water molecules (depending on the channel pore size) upon entering a low-dielectric medium [11, 196, 197]. The total ion solvation free energy of an ion consists of

TABLE 5.1: Parameters for protein solvation CASE I

Parameter	**Value**
Calculation type	Protein solvation
PQR File	Helix.pqr
Grid Dimensions	161 × 161 × 161
Coarse Grid Lengths	200 × 200 × 200
Medium Grid Lengths	100 × 100 × 100
Fine Grid Length	50 × 50 × 50
Counter-Ions	1.0, 0.10, 2.0
	-1.0, 0.10, 2.0
Protein Dielectric	5.0
Solvent dielectric	80.0
Membrane Dielectric	2.0
Headgroup Dielectric	80.0
Solution Method	lpbe
Boundary Condition	Focus
Solvent probe radius (srad)	1.4
Surface sphere density (sdens)	10.0
Temperature	298.15
Z-position of membrane bottom	-21
Membrane thickness	42
Head group thickness	8
Upper exclusion radius	0
Lower exclusion radius	0

a Born solvation term, which corresponds to the removal of water molecules away from the ion and an electrostatic term that corresponds to interaction between protein charges and the ion. APBSmem calculates the ion solvation free energy by first computing the total energy of the protein-ion assembly embedded in the membrane and then subtracting the energies of the membrane-embedded protein without the ion and the energy of the ion in bulk water.

Roux and MacKinnon carried out a classic study using this approach to investigate the transfer energy for a single K^+ from bulk water to the central cavity of the potassium channel KcsA [198]. Here we revisit this calculation. KcsA (PDB ID 1BL8) is aligned along the z-axis and centered at the origin. The ion solvation calculation requires: a PQR file with only the KcsA ion channel and a PQR file consisting of a K^+ ion at the coordinate of interest. The ion transfer free energy is calculated using a finite difference method on a 161^3 grid with two levels of focusing from a cubic system of side length 300 Å to a cube of side length 60 Å. The bathing solution contains 0.1 M symmetric monovalent salt with 2 Å probe radii. The protein is assigned a dielectric interior of $\epsilon_p = 2$, bulk water above and below the membrane, a dielectric of $\epsilon_w = 80$, and a low-dielectric slab of dielectric value $\epsilon_m = 2$ represents the membrane. The separate

TABLE 5.2: Parameters for ion solvation free energy CASE II

Parameter	**Value**
Calculation type	Ion solvation
PQR file 1	KcsA PQR file
PQR file 2	K^+ ion PQR file
Grid dimensions	161 × 161 × 161
Coarse grid lengths	300 × 300 × 300
Medium grid lengths	120 × 120 × 120
Fine grid length	60 × 60 × 60
Counter-ions	1.0, 0.03, 2.0
	-1.0, 0.03, 2.0
Protein dielectric	2.0
Solvent dielectric	80.0
Membrane dielectric	2.0
Headgroup dielectric	80.0
Solution method	lpbe
Boundary condition	Focus
Solvent probe radius (srad)	1.4
Surface sphere density (sdens)	10.0
Temperature	298.15
Z-position of membrane bottom	-12
Membrane thickness	24
Headgroup thickness	0
Upper exclusion radius	24
Lower exclusion radius	16

dielectric for the head group region ($\epsilon = 80$) is not used since its thickness is set to zero. The linearized PB equation is solved using focused boundary conditions (one level of focusing) at 298.15 K in the absence of membrane potential. The solvent probe radius is set to 1.4 Å and a surface sphere density of 10 gridpoints/Å^2 is used. The z-position of the bottom of the membrane and thickness of the membrane slab are set to -12 Å and 24 Å, respectively. Membrane exclusion radii of 24 Å and 16 Å are used for the channel at the top and bottom, respectively (Figure 5.3C). Parameters are summarized in Table 5.2.

APBSmem performs nine calculations: three sequential focusing calculations on the protein-ion system embedded in the membrane (Figure 5.6A), three sequential focusing calculations on just the protein in the membrane (Figure 5.6B) and three sequential focusing calculations on the K^+ ion in bulk water (Figure 5.6C). Note that the system in Figure 5.6C computes the self energy of K^+ in bulk water. APBSmem obtains the ion solvation energy by subtracting the energy values obtained from the fine grid calculation of systems in Figure 5.6B and 5.6C from the system in Figure 5.6A, and a grid spacing of 0.625 Å or smaller gives well converged values (Figure 5.2B).

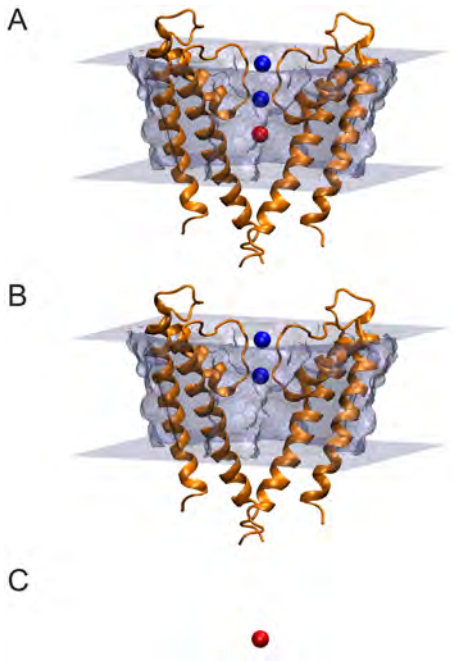

FIGURE 5.6: States used to compute ion solvation energies.

(A) KcsA ion channel (orange) embedded in a slab of low-dielectric material (gray) with two ions in the selectivity filter (blue) and a single ion in the water filled cavity (red). For clarity only two subunits are shown. (B) Set up in panel A without the cavity ion. (C) The cavity ion in bulk water in the absence of KcsA and the membrane. The ion solvation energy is calculated by computing the total electrostatic energy of each system in A, B and C and then calculating the quantity: $E_{total} = E_A - E_B - E_C$.

Using these parameters, the calculated transfer free energy (from bulk water to the center of the cavity) is 7.5 kcal/mol for a single K^+ ion when protein charges are turned off. When two K^+ ions (blue spheres in Figure 5.6) are present in the selectivity filter, the calculated transfer free energy increases to 16.2 kcal/mol. This is due to electrostatic repulsion between the K^+ ions in the selectivity filter and the incoming K^+ ion. Upon turning protein charges on and in the presence of two K^+ ions in the selectivity filter, the transfer free energy drops to -8.3 kcal/mol. Four pore helices (residues 62 - 74) along with the two K^+ ions in the selectivity filter account for an ion transfer free energy of -3.5 kcal/mol. While there are minor differences between some of our calculated values and those of Roux and MacKinnon (see Table 5.3), we believe that the same conclusions can be drawn from our values.

TABLE 5.3: Ion solvation free energy (kcal/mol)

	Roux and MacKinnon [198]	**Calculated values**
K_1^+ only	6.3	7.5
K_1^+, K_2^+, K_3^+ only	16.3	16.2
K_1^+, K_2^+, K_3^+ and all protein	-8.5	-8.3
K_1^+, K_2^+, K_3^+ and pore helices only	-4.5	-3.5

5.2.6 CASE III: Gating Charge

Voltage-gated ion channels are sensitive to changes in membrane potential. The charged residues of the channel experience a force due to the electric field across the membrane-channel complex, and this force drives the channel to open and closed conformations as the membrane potential changes. The voltage dependence of conformational changes can be described by an equivalent "gating charge" or "sensor valence" that is defined as the fraction of the membrane electric field traversed by charges on the protein during the gating process. Thus, a gating charge of 1 indicates that a unit charge has moved through the entire membrane electric field. The gating charge often adopts non-integer values, and the higher the gating charge of a channel, the steeper its voltage dependence. The theory for using continuum electrostatic calculations to determine sensor valence was developed previously [13]. Briefly, the modified PB equation considers the transmembrane potential and calculates the interaction energy of protein charges with the field.

Here we use the murine voltage dependent anion channel 1 (mVDAC1) to illustrate gating charge calculations using APBSmem. The X-ray crystal structure of mVDAC1 shows that it is a 19-stranded β-barrel with an N-terminal α-helix thought to be mVDAC1's primary voltage sensor [199]. Both PB and Poisson-Nernst-Planck (PNP) electrostatic calculations on mVDAC1 suggested that the structure represents the open state of the channel [200]. This case study examines the plausibility of a hypothetical gating motion of the channel, ruled out by Choudhary and co-workers [200]. We consider a gating motion in which the N-terminal helix moves out of the channel and into the outer bath, as shown in Figure 5.7.

The gating charge calculation for this gating motion requires two PQR files - mVDAC1 (PDB ID 3EMN) and a hypothetical closed state structure, to be read in as PQR file 1 and PQR file 2, respectively. We first align mVDAC1 and the hypothetical closed state structure along the z-axis and center them at the origin. The gating charge calculations in this study are carried out on a 161^3 grid with two levels of focusing from a cubic system with side length 300 Å to a smaller cubic system of side length 60 Å. The bathing solution contains 0.1 M symmetric monovalent salt with 2 Å probe radii. The

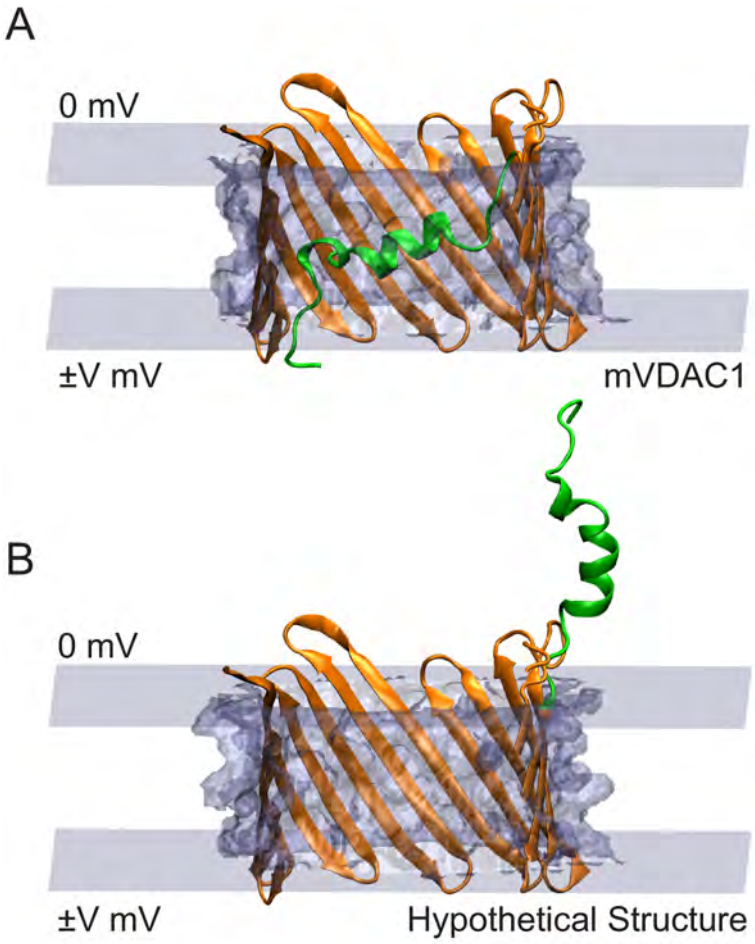

FIGURE 5.7: Hypothetical gating motion involving movement of N-terminal helix (green) out of the pore and into the outer bath.

(A) mVDAC1 x-ray structure (PDB ID 3EMN) embedded in a slab of low-dielectric material (gray). (B) Hypothetical closed state structure embedded in the membrane. In (A) and (B), the potential at the outer bath is held at 0 mV and the potential at inner bath is varied from -50 mV to +50 mV.

influence of the membrane is included as a dielectric slab of value $\epsilon_m = 2$. Water is assigned a dielectric value of $\epsilon_w = 80$, and the protein dielectric is set to $\epsilon_p = 5$. The head group dielectric ($\epsilon = 80$) is only a placeholder variable since its thickness is zero.

The linearized PB equation (lpbe) is solved using focused boundary conditions with one level of focusing at 298.15 K. The interface varies the membrane potential of the inner bath from -50 mV to +50 mV, keeping the potential of the outer bath constant at 0 mV, as shown in Figure 5.7. A solvent probe radius of 1.4 Å and a surface sphere density of 10 gridpoints/Å^2 is used. The z-position of the bottom of the membrane and thickness of the membrane slab are set to -14 Å and 28 Å, respectively. The upper and lower exclusion radii for the membrane are both set to 18.5 Å. All the parameters used for this case study are summarized in Table 5.4.

TABLE 5.4: Parameters for gating charge calculation CASE III

Parameter	**Value**
Calculation type	Gating charge
PQR File 1	3EMN
PQR File 2	Hypothetical closed state
Grid Dimensions	161 × 161 × 161
Coarse Grid Lengths	300 × 300 × 300
Medium Grid Lengths	120 × 120 × 120
Fine Grid Length	60 × 60 × 60
Counter-Ions	1.0, 0.10, 2.0
	-1.0, 0.10, 2.0
Protein Dielectric	5.0
Solvent dielectric	80.0
Membrane Dielectric	2.0
Headgroup Dielectric	80.0
Solution Method	lpbe
Boundary Condition	Membrane potential
	(-50 → +50 mV)
Solvent probe radius (srad)	1.4
Surface sphere density (sdens)	10.0
Temperature	298.15
Z-position of membrane bottom	-14
Membrane thickness	28
Head group thickness	0
Upper exclusion radius	18.5
Lower exclusion radius	18.5

APBSmem performs PB calculations to determine the membrane potential's contribution to the energy difference between mVDAC1, E_1, and the hypothetical closed structure, E_2 ($E = E_2 - E_1$). The energy difference is due to interaction of the protein charges with the membrane electric field. Note that the N-terminal helix has a net charge of +2. The slope of the voltage dependence curve is a measure of voltage-sensor valence which is 1.58 e in this case. This value is very close to that obtained by Choudhary and co-workers [200]. These calculations are useful for determining the voltage sensitivity of a proposed gating mechanism, and within 2.5% of the best estimate they converge to a coarse grid of 1 Å (Figure 5.2). As long as researchers can provide models of hypothetical transitions, these gating calculations can be used to help evaluate their biophysical correctness.

5.3 Discussion

APBSmem is an easy to use software package that carries out electrostatic calculations in the presence of a membrane. We have provided three common cases of interest to

researchers in this field. The first calculates the electrostatic penalty of moving charged proteins into the membrane. This has implications for the stability of membrane proteins and for the design of membrane-permeable molecules. The second example examines the electrostatic energy for moving ions through or into ion channels and transporters. Finally, we showed how APBSmem can be used to determine the voltage dependence of a particular molecular movement. As noted earlier in the protein solvation case study, the membrane is modeled as a dielectric slab of variable thickness. Choe *et al.* [22] discussed the significant effects of membrane bending and its relationship to charged particles. APBSmem will eventually be expanded to identify optimal membrane deformations near the embedded molecule to provide a more complete picture of membrane protein energetics.

APBSmem has been tested on Linux, Mac OS X, and Windows, and both source code and binaries are available for download at http://apbsmem.sourceforge.net/.

Chapter 6

Conclusion

In this dissertation we have presented and evaluated results from a continuum model for evaluating the stability of proteins in the lipid bilayer. The central goal of this model has been to address the question: what are the dominant energetic factors contributing to membrane protein stability? This question is largely motivated by yet another: how can polar and charged residues be stable in the membrane? To this end, we have shown that the model is able to discriminate between membrane proteins and water soluble proteins. The model shows that charged peptides can be stable in the membrane, but not all are stable. This result is important for understanding the function of highly charged membrane proteins such as voltage gated channels as well as charged antibiotic peptides that insert into and cross membranes. Additionally, our model has provided a simple mechanical explanation for the phenomenon of non-additivity of charge insertion.

6.1 Future Directions

We imagine many possible directions for future extensions and enhancements of the work presented here. It would be very useful to use our model to carry out a broader statistical analysis of all membrane proteins alongside a large set of known water soluble proteins, e.g. [201]. This analysis would allow us to more finely tune the model to discriminate between membrane and soluble proteins, likely revealing the most critical physical properties for protein insertion. These results could also be used to build a comparable resource to the Orientation of Proteins in Membranes (OPM) database [21], thereby providing researchers with an alternative prediction of protein stability and membrane interaction which would account for the flexible nature of the membrane. For many proteins, we imagine the results of both approaches would be quite similar,

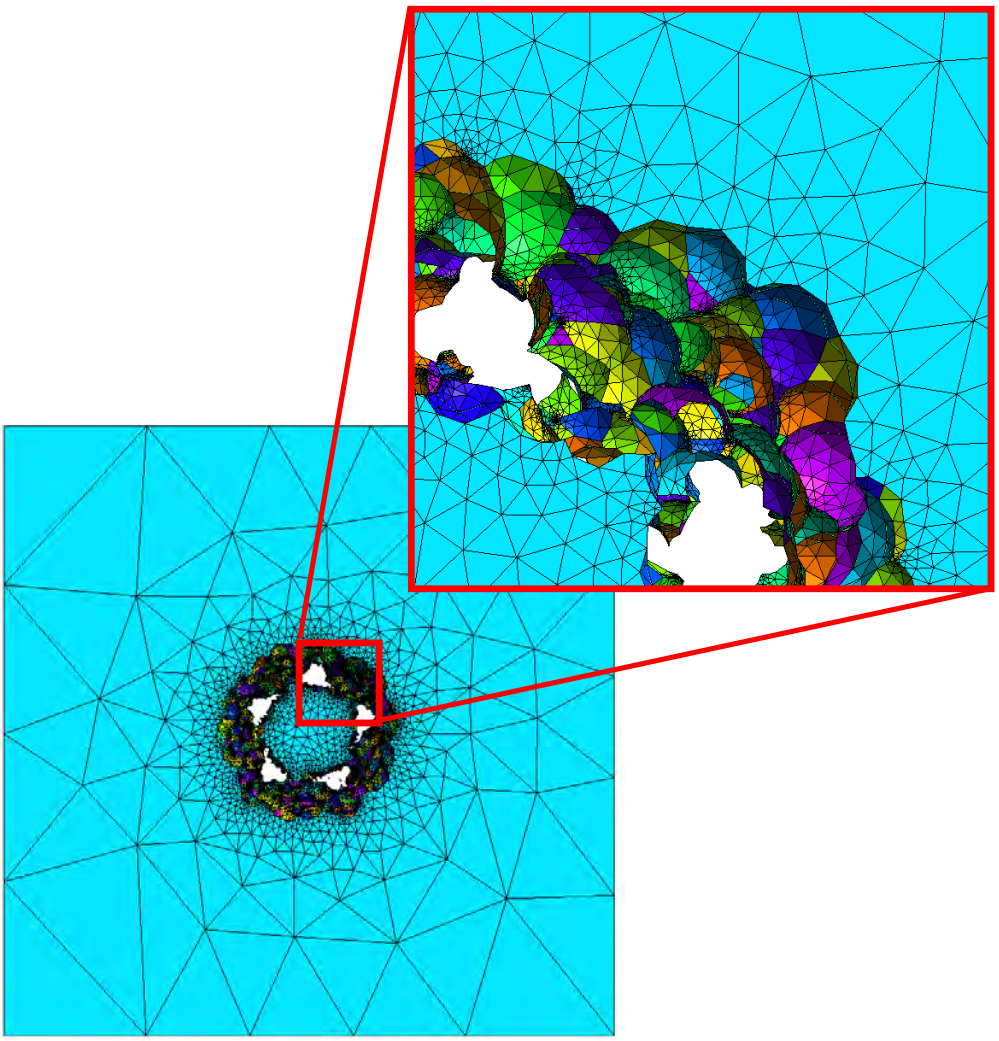

FIGURE 6.1: Finite element mesh of the membrane surrounding a large mechanosensitive channel.

Atoms of the protein are not shown for clarity. The mesh is finely discretized near the protein for greater accuracy, yet increasingly coarsely discretized toward the outer boundary for computational speed. The inset image is a close-up to highlight the fine discretization at the protein-membrane interface.

but in the case of charged proteins we expect our method to potentially give a much more accurate result.

However, as discussed at the end of Chapter 3, in order to extend this model to a broader set of biological systems, there are several limitations of the current method that must be overcome. First, the ability of the protein to tilt to help minimize hydrophobic mismatch is an important phenomenon that cannot currently be represented in this model. This is due to the implementation of our elastic solver which couples the upper and lower leaflets, requiring that each point in the upper leaflet be matched by a point in the lower leaflet. In the case of a tilted protein, this requirement is not met in the region close to the protein. Additionally, charged amino acid side-chains in transmembrane proteins

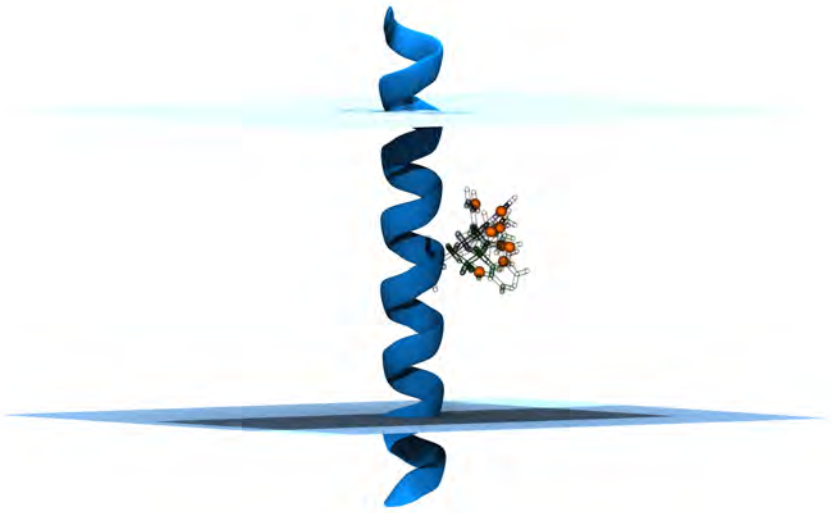

FIGURE 6.2: Most probable rotamer conformations of an arginine side-chain in a transmembrane alpha helix.

The helix (blue) is displayed in cartoon representation, embedded in a flat membrane (light blue). The top 8 most probable arginine side-chains according to the Dunbrack backbone-dependent rotamer library [202] are shown as outlines with the charged termini highlighted as orange spheres.

are known to adjust to their membrane environment. Arginines and lysines in particular have been shown to "snorkel" out of the core of the membrane to interact with polar lipid headgroups and water. Our model utilizes static X-ray and NMR structures and currently does not test alternative side-chain conformations. An important extension of the model would be to optimize important side-chain rotamers, during or after our membrane shape optimization (Figure 6.2). Finally, and perhaps most importantly, our model is currently limited to proteins of approximately cylindrical shape. We have explored the use of cartesian-based elastic solvers, similar to those used by the Weinstein lab [23]; however convergence is very slow for simple finite difference schemes, and the application of non-trivial boundary conditions on the complex boundary proved to be more complex than originally thought. Although challenging to implement, a finite element or adaptive grid refinement scheme may greatly speed up convergence in these systems. These schemes simultaneously allow for both a fine discretization of the elastic membrane surface near the protein to improve accuracy and convergence, and a coarsely discretized surface far from the protein for computational efficiency (Figure 6.1).

There are several other extensions of this work that could be of high practical and scientific value. First, a webserver could be created that allows researchers to upload their own protein, determine the energy of stabilization, and identify the most probable configuration of the protein and shape of the membrane.

Next, this model would be well-suited for exploring the extraction kinetics of membrane

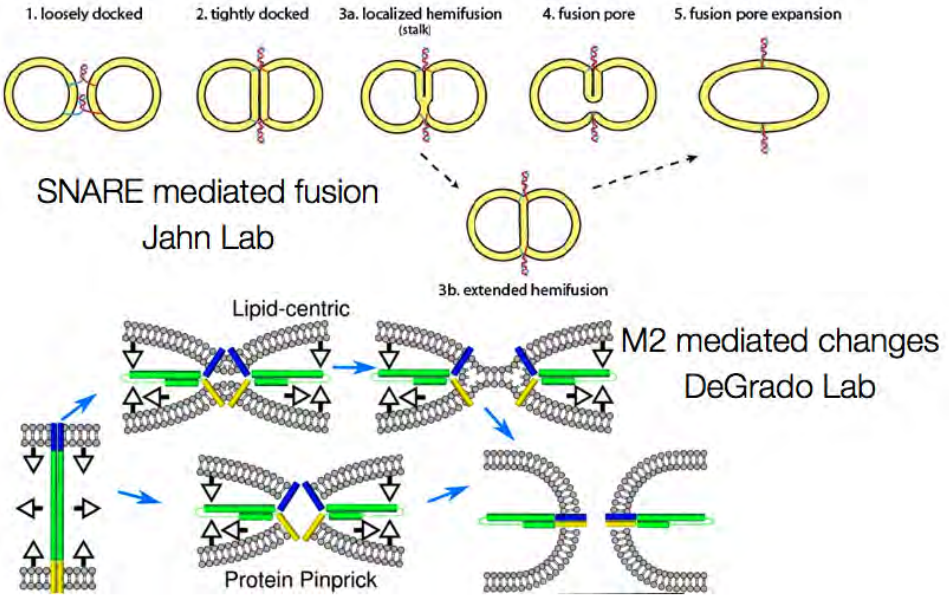

FIGURE 6.3: Model of SNARE-mediated and parainfluenza virus 5 fusion from [1].

proteins from the endoplasmic reticulum (ER) membrane once they have been targeted for ER-associated degradation. How fast can some proteins be removed compared to others? Do charged, lumenal portions of the protein slow down the process of removal across the membrane?

Finally, the flexibility of this membrane model makes it ideal for examining the fusion of adjacent membranes during viral membrane fusion in influenza [1] or SNARE-mediated membrane fusion during exocytosis (Figure 6.3). The membrane proteins play a crucial role in facilitating this process, so the atomistic details are important; however, the system is so large that molecular dynamics would be very difficult to simulate sufficiently. However, our model allows for large-scale membrane deformation and can capture the atomistic nature of the embedded proteins that initiate the fusion.

Appendix A

Supplemental material for Chapter 3

A.1 Search strategies

Searches that are initiated from a flat membrane must overcome a large nonpolar energy barrier to expose a central charged residue to aqueous solution. The red curve in Figure A.1 illustrates the difficulty that the original search algorithm has in crossing this barrier to solvate a central lysine residue on a hydrophobic leucine-alanine TM segment. At iteration 0, the membrane is flat and the insertion energy for the segment is -15 kcal/mol, while we know that the true minimum energy is below -40 kcal/mol (see blue and green curves). Even after almost 3000 iterations, the initial strategy fails to promote sufficient bending of the membrane to expose the lysine, resulting in unfavorable electrostatics. Our next approach was to ignore the nonpolar energy term in the cost function for the first 50 iterations, thereby removing the nonpolar barrier and minimizing the electrostatic energy component. Within the first 50 iterations the search identifies large bent configurations that drop the total energy down below -20 kcal/mol by exposing the lysine (green curve). By 1000 iterations, the search has dropped below -40 kcal/mol and shows little improvement over the next 2000 iterations. The large spikes in the energy every 250 iterations are due to the search algorithm attempting to cover the charged residue. Lastly, we started the search from two initial guesses that exposed the buried charged residue. First, the lower leaflet remained flat and the shape of the upper leaflet was set to a pure sinusoidal curve with a period of 2π and an amplitude and phase that placed the charged atoms in the polar headgroup region or solvent. This was then repeated for the bottom leaflet, and the shape that produced the lowest energy was used to initiate the Powell's-based search. The initial guess method significantly

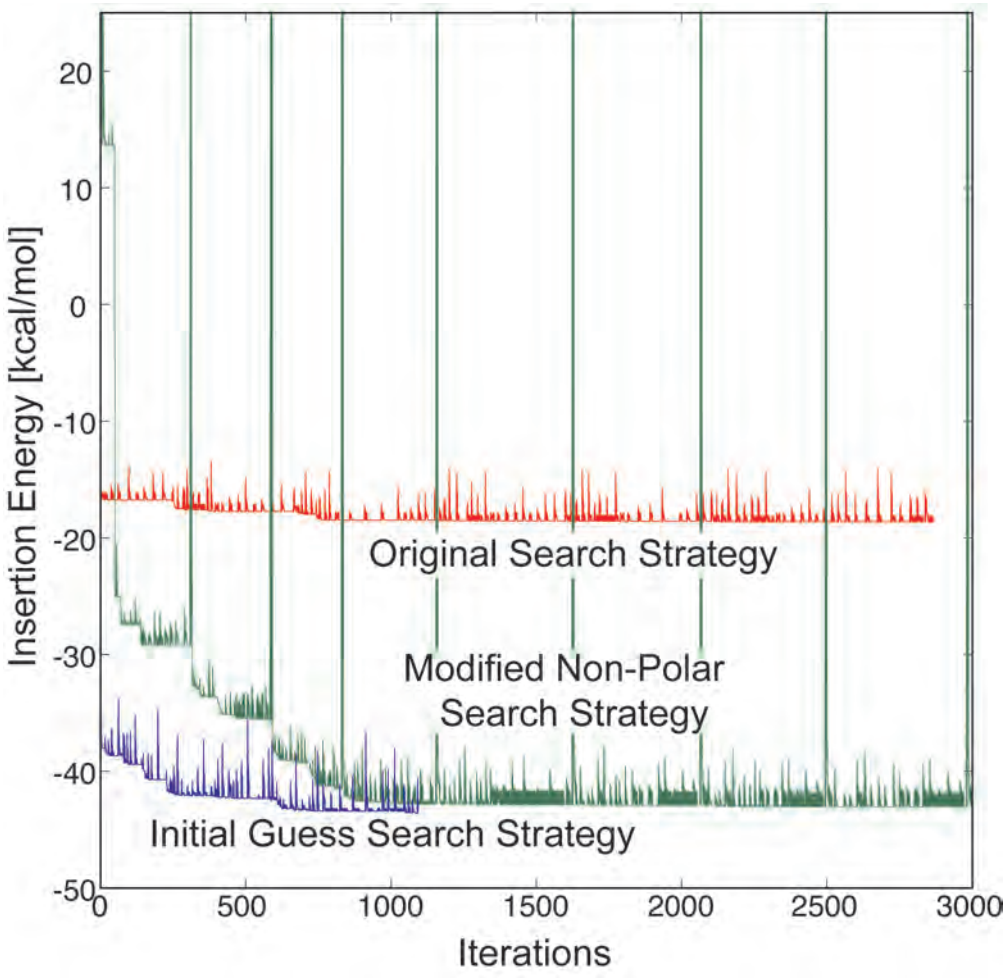

FIGURE A.1: Three different search strategies. We attempted to minimize the total insertion energy of a hydrophobic helix with a central charged lysine.

The original search strategy has the membrane start from a flat, unstressed state. The height value of the contact curve nodes shown in Fig. 1C were then used as independent parameters in the Powell's search strategy. After nearly 3000 iterations of the search strategy, the total energy has been reduced by only a few kcal/mol due to the inability to cross a high energy barrier of exposing hydrophobic residues to solvent before uncovering the lysine (red curve). The modified nonpolar search strategy disregards the nonpolar energy for the first 50 iterations to overcome the barrier and expose the central charged residue to water after about 1000 iterations (green curve). The initial guess search strategy starts from a distorted contact curve that already exposes the buried charged residue to water (blue curve). This method quickly identifies a membrane configuration that is a few kcal/mol more stable than the nonpolar method.

outperforms the other strategies in both its speed and ability to identify global minima as indicated by the blue curve in Figure A.1. For all of the results presented in this manuscript, the initial guess strategy was used and produced the most energetically favorable solutions; however, in many cases we ran all search strategies as a precaution.

A.2 Comparison to existing residue insertion scales

The construction of a hydrophobicity scale allows us to compare our method to a range of previous computational and experimental work. Our expectation was that optimizing the membrane configuration would lead to lower insertion energies compared to our previous calculations which posited simple contact curves [22], and this is important since experiments reveal relatively low insertion energy values compared to computational scales. As in previous studies [22, 121], we matched each helix containing a unique central amino acid with an identical helix whose central residue had been replaced with leucine. We determined the apparent free energy of insertion for each amino acid by finding the difference in the two peptides' insertion energies and subtracting the insertion energy of an individual leucine, -3.6 kcal/mol, calculated as described in our previous work [22].

As shown in Figure A.2, our revised scale is consistent with the overall trend of experiments that finds hydrophobic residues most stable in the membrane and polar and charged residues less stable. The magnitude and spread of the energy values remain the same between our current results and our original work [22], but importantly, our new algorithm outperforms the original model for all amino acids predicting charged residue insertion energies to be 1-2 kcal/mol lower. While the rank ordering of our scale is similar to a recent experiment on peptide insertion in the inner mitochondrial membrane [203], our predicted values are still more in-line with computational results (e.g. [161]) than the low values reported by the translocon studies [66, 121]. Visualization of the system geometry revealed that the membrane significantly bends around central charged residues but that it remains flat when polar and hydrophobic amino acids are inserted. As we previously reported, charged lysine and polar asparagine have comparable insertion energies, although the cost of inserting asparagine is primarily electrostatic since the membrane does not bend while the cost of inserting lysine is largely nonpolar since the membrane bends to expose large regions of the TM segment.

We also tested the effect that the material properties of the membrane had on the scale. In separate calculations, we reduced the compression modulus (K_a), bending modulus (K_c), and stretch (α) parameters to 1/2 of their normal value and in each case the insertion energy scale was only mildly impacted. The charged residue values were most affected, becoming 0.5 kcal/mol easier to insert (data not shown).

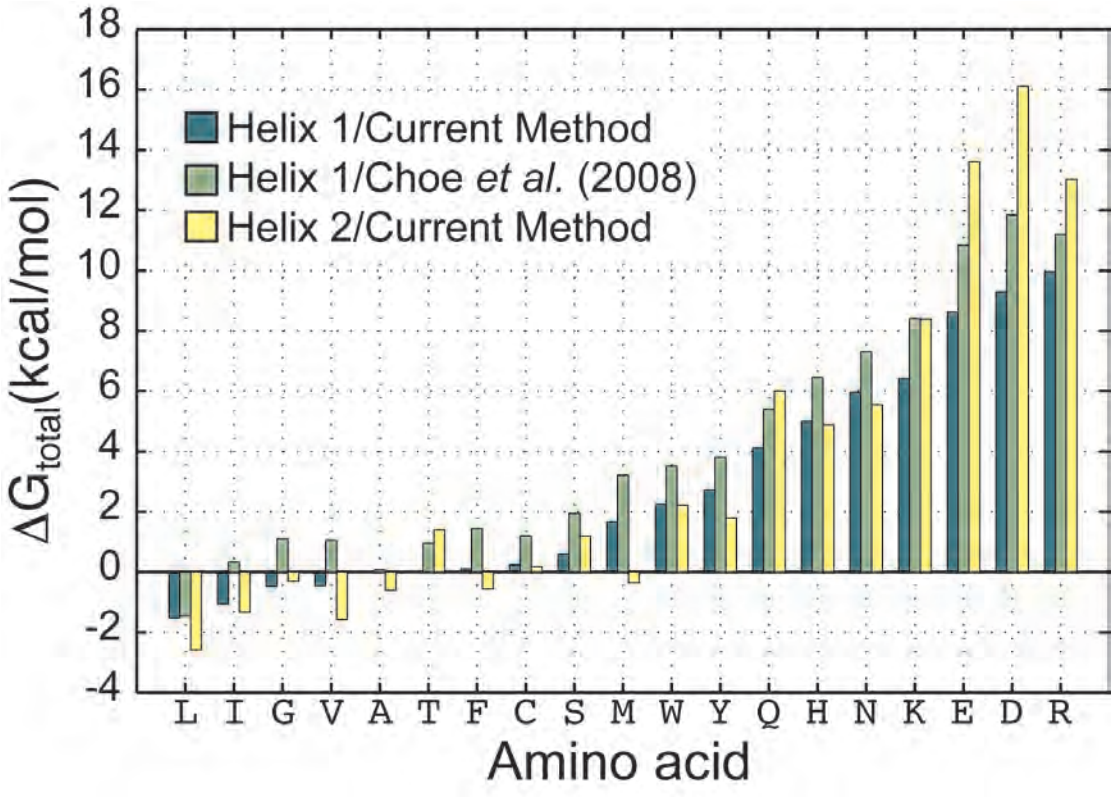

FIGURE A.2: Biological hydrophobicity scale for inserting all natural amino acids (except proline) in the center of a TM helix.

Our search algorithm (dark green) identifies insertion energies that are lower than manual guesses from our previous work (light green) when using the same Helix 1 peptides (H-segments) flanked by 4 glycine residues [22]. Charged amino acids (K, E, D, R) are 2-7 kcal/mol more destabilizing to Helix 2 peptides (yellow bars), which are flanked by polar asparagines and charged lysines. All 3 scales were shifted by +2.04 kcal/mol to set the alanine insertion energy to zero for the Current Method.

A.3 Context dependence of hydrophobicity scales

A biological hydrophobicity scale was reconstructed using a TM segment with different flanking residues (yellow bars in Figure A.2). We replaced the N- and C-terminal flanking glycine residues, similar to the H-segment studied by Hessa and co-workers [121], with a charged sequence, NNKK ... KKNN, typical of amino acid sequences at the membrane-water interface. As shown in the bar chart, most of the Helix 2 insertion energies are within 1 kcal/mol of the original values (dark green); however, glutamate, aspartate, lysine and arginine all destabilize the new segment 2-7 kcal/mol more than they destabilize the original segment.

This destabilization is predominantly due to a large increase in the solvent-accessible surface area. In the new reference peptide, in which the central amino acid is a leucine, the membrane remains flat and the lysine residues are buried in the headgroup region.

This is an energetically favorable configuration since it reduces the SASA of the TM segment while allowing the charged lysines to interact favorably with polar lipid headgroups. When the central amino acid is replaced by a charged residue, the membrane bends to expose the NNKK sequence to water resulting in a much greater nonpolar energy penalty than incurred for the original GGGG sequence due to the larger size of lysines and asparagines.

A.4 Comparison with Generalized Born

We wanted to compare our continuum method for computing the energetics of membrane proteins to other continuum methods that use Generalized Born methods along with modifications to model the membrane. We chose the CHARMM GBSW module which is an extremely popular method in the field [2, 172]. Insertion energies for TM helices harboring varying numbers of arginine residues were calculated in CHARMM c32b2 using the molecular surface representation, a bilayer thickness of 42 Ångstroms, a membrane dielectric of 2, a solvent dielectric of 80, and an effective surface tension coefficient of 0.005. We used the set of same parameter values to carry out the comparison calculations using our method. The peptide's atomic radii were taken from the radius_gbsw set which was calibrated for GBSW calculations [204, 205]. A membrane switching length of 2.5 angstroms was used. The default values were used for all other GBSW parameters. Briefly, we carried out an electrostatic point calculation in the presence of the membrane, and then we carried out the same point calculation in solution using an external dielectric value of 80 everywhere outside the protein. The electrostatic component of the insertion energy was recorded as the difference between these two energies.

TABLE A.1: Electrostatics and system parameters for all calculations

Parameter	**Value**
Electrostatics Grid Dimensions	$161 \times 161 \times 161$ Å^3
Coarse Grid Lengths	$200 \times 200 \times 200$ Å^3
Medium Grid Lengths	$100 \times 100 \times 100$ Å^3
Fine Grid Lengths	$50 \times 50 \times 50$ Å^3
Counter-Ions	0.1 M symmetric salt
Protein Dielectric	2.0
Membrane Dielectric	2.0
Headgroup Dielectric	80.0
Solvent Dielectric	80.0
Solution Method	Linearized Poisson-Boltzmann Equation
Solvent Probe Radius	1.4 Å
Surface Sphere Density	10.0 grid points/Å^2
Temperature	298.15 K
Membrane Thickness	42.0 Å
Headgroup Thickness	8.0 Å
Bending modulus (K_c)	2.85×10^{-10} N/Å
Compression modulus (K_a)	1.425×10^{-11} N/Å
Surface tension (α)	3×10^{-13} NÅ

Bibliography

[1] J. E. Donald, Y. Zhang, G. Fiorin, V. Carnevale, D. R. Slochower, F. Gai, M. L. Klein, and W. F. DeGrado, "Transmembrane orientation and possible role of the fusogenic peptide from parainfluenza virus 5 (piv5) in promoting fusion," *Proceedings of the National Academy of Sciences*, vol. 108, no. 10, pp. 3958–3963, 2011.

[2] W. Im, M. S. Lee, and C. L. Brooks, "Generalized born model with a simple smoothing function.," *Journal of Computational Chemistry*, vol. 24, pp. 1691–702, Nov. 2003.

[3] K. Illergård, A. Kauko, and A. Elofsson, "Why are polar residues within the membrane core evolutionary conserved?," *Proteins: Structure, Function, and Bioinformatics*, vol. 79, no. 1, pp. 79–91, 2011.

[4] E. Vivès, P. Brodin, and B. Lebleu, "A truncated HIV-1 Tat protein basic domain rapidly translocates through the plasma membrane and accumulates in the cell nucleus," *Journal of Biological Chemistry*, vol. 272, no. 25, pp. 16010–16017, 1997.

[5] S. Cabani, P. Gianni, V. Mollica, and L. Lepori, "Group contributions to the thermodynamic properties of non-ionic organic solutes in dilute aqueous solution," *Journal of Solution Chemistry*, vol. 10, no. 8, pp. 563–595, 1981.

[6] T. Hessa, H. Kim, K. Bihlmaier, C. Lundin, J. Boekel, H. Andersson, I. Nilsson, S. White, and G. Von Heijne, "Recognition of transmembrane helices by the endoplasmic reticulum translocon," *Nature*, vol. 433, pp. 377–381, Jan. 2005.

[7] C. P. Moon and K. G. Fleming, "Side-chain hydrophobicity scale derived from transmembrane protein folding into lipid bilayers.," *Proceedings of the National Academy of Sciences*, pp. 1103979108–, May 2011.

[8] J. A. Freites, D. J. Tobias, G. Von Heijne, and S. H. White, "Interface connections of a transmembrane voltage sensor," *Proceedings of the National Academy of Sciences*, vol. 102, no. 42, pp. 15059–15064, 2005.

[9] S. Dorairaj and T. W. Allen, "On the thermodynamic stability of a charged arginine side chain in a transmembrane helix.," *Proceedings of the National Academy of Sciences*, vol. 104, pp. 4943–8, Mar. 2007.

[10] D. Krepkiy, M. Mihailescu, J. A. Freites, E. V. Schow, D. L. Worcester, K. Gawrisch, D. J. Tobias, S. H. White, and K. J. Swartz, "Structure and hydration of membranes embedded with voltage-sensing domains.," *Nature*, vol. 462, pp. 473–9, Nov. 2009.

[11] A. Parsegian, "Energy of an ion crossing a low dielectric membrane: solutions to four relevant electrostatic problems.," *Nature*, vol. 221, no. 5183, pp. 844–846, 1969.

[12] N. Ben-Tal, A. Ben-Shaul, A. Nicholls, and B. Honig, "Free-energy determinants of alpha-helix insertion into lipid bilayers," *Biophysical Journal*, vol. 70, pp. 1803–1812, Apr. 1996.

[13] B. Roux, "Influence of the membrane potential on the free energy of an intrinsic protein.," *Biophysical Journal*, vol. 73, pp. 2980–9, Dec. 1997.

[14] W. Helfrich, "Elastic properties of lipid bilayers: theory and possible experiments.," *Zeitschrift für Naturforschung. Teil C: Biochemie, Biophysik, Biologie, Virologie*, vol. 28, no. 11, p. 693, 1973.

[15] H. W. Huang, "Deformation free energy of bilayer membrane and its effect on gramicidin channel lifetime.," *Biophysical Journal*, vol. 50, pp. 1061–70, Dec. 1986.

[16] C. Nielsen, M. Goulian, and O. Andersen, "Energetics of inclusion-induced bilayer deformations.," *Biophysical Journal*, vol. 74, pp. 1966–83, Apr. 1998.

[17] N. Dan, P. Pincus, and S. Safran, "Membrane-induced interactions between inclusions," *Langmuir*, vol. 9, no. 11, pp. 2768–2771, 1993.

[18] K. S. Kim, J. Neu, and G. Oster, "Curvature-mediated interactions between membrane proteins.," *Biophysical Journal*, vol. 75, pp. 2274–91, Nov. 1998.

[19] M. Grabe, J. Neu, G. Oster, and P. Nollert, "Protein interactions and membrane geometry," *Biophysical Journal*, vol. 84, no. 2, pp. 854–868, 2003.

[20] A. L. Lomize, I. D. Pogozheva, M. A. Lomize, and H. I. Mosberg, "Positioning of proteins in membranes: a computational approach," *Protein Science*, vol. 15, no. 6, pp. 1318–1333, 2006.

[21] M. A. Lomize, A. L. Lomize, I. D. Pogozheva, and H. I. Mosberg, "OPM: orientations of proteins in membranes database.," *Bioinformatics (Oxford, England)*, vol. 22, pp. 623–5, Mar. 2006.

[22] S. Choe, K. A. Hecht, and M. Grabe, "A continuum method for determining membrane protein insertion energies and the problem of charged residues.," *Journal of General Physiology*, vol. 131, pp. 563–73, June 2008.

[23] G. Khelashvili, D. Harries, and H. Weinstein, "Modeling membrane deformations and lipid demixing upon protein-membrane interaction: the BAR dimer adsorption.," *Biophysical Journal*, vol. 97, pp. 1626–35, Sept. 2009.

[24] S. Mondal, G. Khelashvili, J. Shan, O. S. Andersen, and H. Weinstein, "Quantitative modeling of membrane deformations by multihelical membrane proteins: application to g-protein coupled receptors," *Biophysical Journal*, vol. 101, no. 9, pp. 2092–2101, 2011.

[25] S. Mondal, G. Khelashvili, L. Shi, and H. Weinstein, "The cost of living in the membrane: A case study of hydrophobic mismatch for the multi-segment protein leut," *Chemistry and Physics of Lipids*, 2013.

[26] N. Kucerka, S. Tristram-Nagle, and J. F. Nagle, "Structure of fully hydrated fluid phase lipid bilayers with monounsaturated chains.," *The Journal of Membrane Biology*, vol. 208, pp. 193–202, Dec. 2005.

[27] C. Helm, H. Möhwald, K. Kjaer, and J. Als-Nielsen, "Phospholipid monolayer density distribution perpendicular to the water surface. a synchrotron x-ray reflectivity study," *Europhysics Letters*, vol. 4, no. 6, p. 697, 1987.

[28] B. Honig and a. Nicholls, "Classical electrostatics in biology and chemistry.," *Science*, vol. 268, pp. 1144–9, May 1995.

[29] K. M. Callenberg, O. P. Choudhary, G. L. DeForest, D. W. Gohara, N. A. Baker, and M. Grabe, "APBSmem: a graphical interface for electrostatic calculations at the membrane," *PloS ONE*, vol. 5, no. 9, p. e12722, 2010.

[30] T. Ooi, M. Oobatake, G. Nemethy, and H. A. Scheraga, "Accessible surface areas as a measure of the thermodynamic parameters of hydration of peptides," *Proceedings of the National Academy of Sciences*, vol. 84, no. 10, pp. 3086–3090, 1987.

[31] D. Sitkoff, N. Ben-Tal, and B. Honig, "Calculation of Alkane to Water Solvation Free Energies Using Continuum Solvent Models," *The Journal of Physical Chemistry*, vol. 100, pp. 2744–2752, Jan. 1996.

[32] A. Shrake and J. Rupley, "Environment and exposure to solvent of protein atoms. lysozyme and insulin," *Journal of Molecular Biology*, vol. 79, no. 2, pp. 351–371, 1973.

[33] A. L. Lomize, I. Pogozheva, and H. Mosberg, "Quantification of helix–helix binding affinities in micelles and lipid bilayers," *Protein Science*, vol. 13, no. 10, pp. 2600–2612, 2004.

[34] T. Dolinsky, J. Nielsen, J. McCammon, and N. a. Baker, "PDB2PQR: an automated pipeline for the setup of Poisson-Boltzmann electrostatics calculations," *Nucleic Acids Research*, vol. 32, no. Web Server Issue, p. W665, 2004.

[35] T. J. Dolinsky, P. Czodrowski, H. Li, J. E. Nielsen, J. H. Jensen, G. Klebe, and N. A. Baker, "PDB2PQR: expanding and upgrading automated preparation of biomolecular structures for molecular simulations.," *Nucleic acids research*, vol. 35, pp. W522–5, July 2007.

[36] M. J. D. Powell, "An efficient method for finding the minimum of a function of several variables without calculating derivatives," *The Computer Journal*, vol. 7, pp. 155–162, Feb. 1964.

[37] K. M. Callenberg, N. R. Latorraca, and M. Grabe, "Membrane bending is critical for the stability of voltage sensor segments in the membrane," *Journal Of General Physiology*, vol. 140, no. 1, pp. 55–68, 2012.

[38] S. Kirkpatrick, C. D. Gelatt, and M. P. Vecchi, "Optimization by simulated annealing," *Science*, vol. 220, pp. 671–680, 1983.

[39] M. Celis, J. Dennis, and R. Tapia, "A trust region strategy for nonlinear equality constrained optimization," *Numerical optimization*, vol. 1984, pp. 71–82, 1985.

[40] S. H. White, "Formation of "solvent-free" black lipid bilayer membranes from glyceryl monooleate dispersed in squalene.," *Biophysical Journal*, vol. 23, pp. 337–47, Sept. 1978.

[41] C. Schutz and A. Warshel, "What are the dielectric constants of proteins and how to validate electrostatic models?," *Proteins: Structure, Function, and Bioinformatics*, vol. 44, no. 4, pp. 400–417, 2001.

[42] B. Cohen, T. McAnaney, E. Park, Y. Jan, S. Boxer, and L. Jan, "Probing protein electrostatics with a synthetic fluorescent amino acid," *Science*, vol. 296, no. 5573, pp. 1700–1703, 2002.

[43] S. Höfinger and T. Simonson, "Dielectric relaxation in proteins: a continuum electrostatics model incorporating dielectric heterogeneity of the protein and time-dependent charges," *Journal of Computational Chemistry*, vol. 22, no. 3, pp. 290–305, 2001.

[44] D. Sitkoff, K. Sharp, and B. Honig, "Accurate calculation of hydration free energies using macroscopic solvent models," *Journal of Physical Chemistry*, vol. 98, no. 7, pp. 1978–1988, 1994.

[45] S. Tanizaki and M. Feig, "A generalized Born formalism for heterogeneous dielectric environments: Application to the implicit modeling of biological membranes," *The Journal of Chemical Physics*, vol. 122, p. 124706, 2005.

[46] H. a. Stern and S. E. Feller, "Calculation of the dielectric permittivity profile for a nonuniform system: Application to a lipid bilayer simulation," *The Journal of Chemical Physics*, vol. 118, no. 7, p. 3401, 2003.

[47] A. Radzicka and R. Wolfenden, "Comparing the polarities of the amino acids: side-chain distribution coefficients between the vapor phase, cyclohexane, 1-octanol, and neutral aqueous solution," *Biochemistry*, vol. 27, no. 5, pp. 1664–1670, 1988.

[48] J. A. Wagoner and N. A. Baker, "Assessing implicit models for nonpolar mean solvation forces: the importance of dispersion and volume terms.," *Proceedings of the National Academy of Sciences*, vol. 103, pp. 8331–6, May 2006.

[49] D. Chandler, "Interfaces and the driving force of hydrophobic assembly," *Nature*, vol. 437, no. 7059, pp. 640–647, 2005.

[50] T. Hessa, S. H. White, and G. von Heijne, "Membrane insertion of a potassium-channel voltage sensor.," *Science*, vol. 307, p. 1427, Mar. 2005.

[51] A. Parsegian, "Energy of an ion crossing a low dielectric membrane: solutions to four relevant electrostatic problems," *Nature*, vol. 221, no. 5183, p. 844, 1969.

[52] D. Papazian, T. Schwarz, B. Tempel, Y. Jan, and L. Jan, "Cloning of genomic and complementary dna from shaker, a putative potassium channel gene from drosophila," *Science*, vol. 237, no. 4816, p. 749, 1987.

[53] S. K. Aggarwal and R. MacKinnon, "Contribution of the s4 segment to gating charge in the shaker k+ channel," *Neuron*, vol. 16, no. 6, pp. 1169–1177, 1996.

[54] S.-A. Seoh, D. Sigg, D. M. Papazian, and F. Bezanilla, "Voltage-sensing residues in the s2 and s4 segments of the shaker k+ channel," *Neuron*, vol. 16, no. 6, pp. 1159–1167, 1996.

[55] S. B. Long, E. B. Campbell, and R. MacKinnon, "Voltage sensor of kv1. 2: Structural basis of electromechanical coupling," *Science*, vol. 309, pp. 903–908, 2005.

[56] C. Armstrong, "Sodium channels and gating currents," *Physiological Reviews*, vol. 61, no. 3, p. 644, 1981.

[57] W. A. Catterall, "Molecular properties of voltage-sensitive sodium channels," *Annual Review of Biochemistry*, vol. 55, no. 1, pp. 953–985, 1986.

[58] S. K. Tiwari-Woodruff, C. T. Schulteis, A. F. Mock, and D. M. Papazian, "Electrostatic interactions between transmembrane segments mediate folding of shaker k+ channel subunits," *Biophysical Journal*, vol. 72, no. 4, pp. 1489–1500, 1997.

[59] S. Durell, Y. Hao, and H. Guy, "Structural models of the transmembrane region of voltage-gated and other k+ channels in open, closed, and inactivated conformations," *Journal of Structural Biology*, vol. 121, no. 2, pp. 263–284, 1998.

[60] H. Lecar, H. P. Larsson, and M. Grabe, "Electrostatic model of S4 motion in voltage-gated ion channels.," *Biophysical Journal*, vol. 85, pp. 2854–64, Nov. 2003.

[61] M. Pathak, V. Yarov-Yarovoy, G. Agarwal, B. Roux, P. Barth, S. Kohout, F. Tombola, and E. Isacoff, "Closing in on the resting state of the Shaker K+ channel," *Neuron*, vol. 56, no. 1, pp. 124–140, 2007.

[62] L. G. Cuello, D. M. Cortes, and E. Perozo, "Molecular architecture of the KvAP voltage-dependent K+ channel in a lipid bilayer.," *Science*, vol. 306, pp. 491–5, Oct. 2004.

[63] V. Ruta, J. Chen, and R. MacKinnon, "Calibrated measurement of gating-charge arginine displacement in the KvAP voltage-dependent K+ channel.," *Cell*, vol. 123, pp. 463–75, Nov. 2005.

[64] D. Schmidt, Q.-X. Jiang, and R. MacKinnon, "Phospholipids and the origin of cationic gating charges in voltage sensors," *Nature*, vol. 444, pp. 775–779, Dec. 2006.

[65] A. Johansson and E. Lindahl, "The role of lipid composition for insertion and stabilization of amino acids in membranes," *The Journal of chemical physics*, vol. 130, no. 18, p. 185101, 2009.

[66] T. Hessa, N. N. M. Meindl-Beinker, A. Bernsel, H. Kim, Y. Sato, M. Lerch-Bader, I. I. Nilsson, S. S. H. White, and G. von Heijne, "Molecular code for transmembrane-helix recognition by the Sec61 translocon," *Nature*, vol. 450, pp. 1026–1030, Dec. 2007.

[67] C. P. Moon and K. G. Fleming, "Side-chain hydrophobicity scale derived from transmembrane protein folding into lipid bilayers.," *Proceedings of the National Academy of Sciences*, May 2011.

[68] J. A. Freites, D. J. Tobias, G. von Heijne, and S. H. White, "Interface connections of a transmembrane voltage sensor.," *Proceedings of the National Academy of Sciences*, vol. 102, pp. 15059–64, Oct. 2005.

[69] J. L. MacCallum, W. F. D. Bennett, and D. P. Tieleman, "Partitioning of amino acid side chains into lipid bilayers: results from computer simulations and comparison to experiment.," *Journal of General Physiology*, vol. 129, pp. 371–7, May 2007.

[70] D. Krepkiy, M. Mihailescu, J. Freites, E. Schow, D. Worcester, K. Gawrisch, D. Tobias, S. White, and K. Swartz, "Structure and hydration of membranes embedded with voltage-sensing domains," *Nature*, vol. 462, no. 7272, pp. 473–479, 2009.

[71] H. Luo and S. C. Tucker, "Compressible Continuum Solvation Model for Molecular Solutes," *Journal of the American Chemical Society*, vol. 117, pp. 11359–11360, Nov. 1995.

[72] J. Dzubiella, J. M. J. Swanson, and J. A. McCammon, "Coupling hydrophobicity, dispersion, and electrostatics in continuum solvent models.," *Physical review letters*, vol. 96, p. 087802, Mar. 2006.

[73] N. Baker, D. Sept, S. Joseph, M. Holst, and J. McCammon, "Electrostatics of nanosystems: application to microtubules and the ribosome," *Proceedings of the National Academy of Sciences*, vol. 98, no. 18, pp. 10037–10041, 2001.

[74] W. Humphrey, A. Dalke, and K. Schulten, "VMD: visual molecular dynamics," *Journal of Molecular Graphics*, vol. 14, pp. 33–38, Feb. 1996.

[75] G. Krivov, M. Shapovalov, and R. Dunbrack Jr, "Improved prediction of protein side-chain conformations with SCWRL4," *Proteins: Structure, Function, and Bioinformatics*, vol. 77, no. 4, pp. 778–795, 2009.

[76] A. Sali and T. L. Blundell, "Comparative protein modelling by satisfaction of spatial restraints.," *Journal of Molecular Biology*, vol. 234, pp. 779–815, Dec. 1993.

[77] E. L. Snapp, R. S. Hegde, M. Francolini, F. Lombardo, S. Colombo, E. Pedrazzini, N. Borgese, and J. Lippincott-Schwartz, "Formation of stacked ER cisternae by low affinity protein interactions.," *The Journal of Cell Biology*, vol. 163, pp. 257–69, Oct. 2003.

[78] T. Itoh, K. S. Erdmann, A. Roux, B. Habermann, H. Werner, and P. De Camilli, "Dynamin and the actin cytoskeleton cooperatively regulate plasma membrane invagination by BAR and F-BAR proteins.," *Developmental cell*, vol. 9, pp. 791–804, Dec. 2005.

[79] M. C. S. Lee, L. Orci, S. Hamamoto, E. Futai, M. Ravazzola, and R. Schekman, "Sar1p N-terminal helix initiates membrane curvature and completes the fission of a COPII vesicle.," *Cell*, vol. 122, pp. 605–17, Aug. 2005.

[80] T. Wollert, C. Wunder, J. Lippincott-Schwartz, and J. Hurley, "Membrane scission by the ESCRT-III complex," *Nature*, vol. 458, no. 7235, pp. 172–177, 2009.

[81] M. Vrljic, P. Strop, J. A. Ernst, R. B. Sutton, S. Chu, and A. T. Brunger, "Molecular mechanism of the synaptotagmin-SNARE interaction in Ca2+-triggered vesicle fusion.," *Nature Structural & Molecular Biology*, vol. 17, pp. 325–31, Mar. 2010.

[82] M. Ulmschneider, J. Ulmschneider, M. Sansom, and A. Di Nola, "A generalized Born implicit-membrane representation compared to experimental insertion free energies," *Biophysical Journal*, vol. 92, no. 7, pp. 2338–2349, 2007.

[83] W. Yau, W. Wimley, and K. Gawrisch, "The preference of tryptophan for membrane interfaces," *Biochemistry*, vol. 37, pp. 14713–14718, Aug. 1998.

[84] T. M. Weiss, P. C. A. van der Wel, J. A. Killian, R. E. Koeppe, and H. W. Huang, "Hydrophobic Mismatch between Helices and Lipid Bilayers," *Biophysical Journal*, vol. 84, pp. 379–85, Jan. 2003.

[85] J. H. Kleinschmidt and L. K. Tamm, "Secondary and tertiary structure formation of the beta-barrel membrane protein OmpA is synchronized and depends on membrane thickness.," *Journal of Molecular Biology*, vol. 324, pp. 319–30, Nov. 2002.

[86] O. Soubias, S.-L. Niu, D. C. Mitchell, and K. Gawrisch, "Lipid-rhodopsin hydrophobic mismatch alters rhodopsin helical content.," *Journal of the American Chemical Society*, vol. 130, pp. 12465–71, Sept. 2008.

[87] T. A. Harroun, W. T. Heller, T. M. Weiss, L. Yang, and H. W. Huang, "Experimental evidence for hydrophobic matching and membrane-mediated interactions in lipid bilayers containing gramicidin," *Biophysical Journal*, vol. 76, no. 2, pp. 937–945, 1999.

[88] M. Ravazzola and L. Orci, "Glucagon and glicentin immunoreactivity are topologically segregated in the alpha granule of the human pancreatic A cell.," *Nature*, vol. 284, pp. 66–7, Mar. 1980.

[89] C. E. Morris, P. F. Juranka, W. Lin, T. J. Morris, and U. Laitko, "Studying the mechanosensitivity of voltage-gated channels using oocyte patches.," *Methods in molecular biology (Clifton, N.J.)*, vol. 322, pp. 315–29, Jan. 2006.

[90] S. Sukharev, S. R. Durell, and H. R. Guy, "Structural Models of the MscL Gating Mechanism," *Biophysical Journal*, vol. 81, pp. 917–36, Aug. 2001.

[91] E. Perozo, A. Kloda, D. M. Cortes, and B. Martinac, "Physical principles underlying the transduction of bilayer deformation forces during mechanosensitive channel gating," *Nat Struct Mol Biol*, vol. 9, no. 9, pp. 696–703, 2002.

[92] G. Chang, R. Spencer, A. Lee, M. Barclay, and D. Rees, "Structure of the MscL homolog from Mycobacterium tuberculosis: a gated mechanosensitive ion channel," *Science*, vol. 282, pp. 2220–2226, Dec. 1998.

[93] A. M. Powl, J. N. Wright, J. M. East, and A. G. Lee, "Identification of the hydrophobic thickness of a membrane protein using fluorescence spectroscopy: studies with the mechanosensitive channel MscL.," *Biochemistry*, vol. 44, pp. 5713–21, Apr. 2005.

[94] P. Wiggins and R. Phillips, "Analytic models for mechanotransduction: gating a mechanosensitive channel.," *Proceedings of the National Academy of Sciences*, vol. 101, pp. 4071–6, Mar. 2004.

[95] J. L. Maccallum, W. F. D. Bennett, and D. P. Tieleman, "Transfer of arginine into lipid bilayers is nonadditive.," *Biophysical Journal*, vol. 101, pp. 110–7, July 2011.

[96] W. Im, M. Lee, and C. Brooks, "Generalized born model with a simple smoothing function," *Journal of Computational Chemistry*, vol. 24, pp. 1691–702, Nov. 2003.

[97] M. Noda, S. Shimizu, T. Tanabe, T. Takai, T. Kayano, T. Ikeda, H. Takahashi, H. Nakayama, Y. Kanaoka, N. Minamino, K. Kangawa, H. Matsuo, M. A. Raftery, T. Hirose, S. Inayama, H. Hayashida, T. Miyata, and S. Numa, "Primary structure of Electrophorus electricus sodium channel deduced from cDNA sequence," *Nature*, vol. 312, pp. 121–127, Nov. 1984.

[98] I. S. Ramsey, M. M. Moran, J. A. Chong, and D. E. Clapham, "A voltage-gated proton-selective channel lacking the pore domain.," *Nature*, vol. 440, pp. 1213–6, Apr. 2006.

[99] M. Sasaki, M. Takagi, and Y. Okamura, "A voltage sensor-domain protein is a voltage-gated proton channel.," *Science*, vol. 312, pp. 589–92, Apr. 2006.

[100] Y. Murata, H. Iwasaki, M. Sasaki, K. Inaba, and Y. Okamura, "Phosphoinositide phosphatase activity coupled to an intrinsic voltage sensor.," *Nature*, vol. 435, pp. 1239–43, June 2005.

[101] H. R. Guy and P. Seetharamulu, "Molecular model of the action potential sodium channel," *Proceedings of the National Academy of Sciences*, vol. 83, no. 2, pp. 508–512, 1986.

[102] C. L. Wee, A. Chetwynd, and M. S. Sansom, "Membrane insertion of a voltage sensor helix," *Biophysical Journal*, vol. 100, no. 2, p. 410, 2011.

[103] L. Zhang, Y. Sato, T. Hessa, G. von Heijne, J.-K. Lee, I. Kodama, M. Sakaguchi, and N. Uozumi, "Contribution of hydrophobic and electrostatic interactions to the membrane integration of the Shaker K+ channel voltage sensor domain.," *Proceedings of the National Academy of Sciences*, vol. 104, pp. 8263–8, May 2007.

[104] P. J. Bond, C. L. Wee, and M. S. Sansom, "Coarse-grained molecular dynamics simulations of the energetics of helix insertion into a lipid bilayer," *Biochemistry*, vol. 47, no. 43, pp. 11321–11331, 2008.

[105] S. B. Long, X. Tao, E. B. Campbell, and R. MacKinnon, "Atomic structure of a voltage-dependent K+ channel in a lipid membrane-like environment.," *Nature*, vol. 450, pp. 376–82, Nov. 2007.

[106] G. M. Clayton, S. Altieri, L. Heginbotham, V. M. Unger, and J. a. H. Morais-Cabral, "Structure of the transmembrane regions of a bacterial cyclic nucleotide-regulated channel.," *Proceedings of the National Academy of Sciences*, vol. 105, pp. 1511–5, Feb. 2008.

[107] R. S. a. Vieira-Pires and J. a. H. Morais-Cabral, "3(10) helices in channels and other membrane proteins.," *The Journal of General Physiology*, vol. 136, pp. 585–92, Dec. 2010.

[108] L. Wang, P. S. Bose, and F. J. Sigworth, "Using cryo-em to measure the dipole potential of a lipid membrane," *Proceedings of the National Academy of Sciences*, vol. 103, no. 49, pp. 18528–18533, 2006.

[109] H. Hong and L. K. Tamm, "Elastic coupling of integral membrane protein stability to lipid bilayer forces.," *Proceedings of the National Academy of Sciences*, vol. 101, pp. 4065–70, Mar. 2004.

[110] K. J. Tierney, D. E. Block, and M. L. Longo, "Elasticity and phase behavior of dppc membrane modulated by cholesterol, ergosterol, and ethanol," *Biophysical Journal*, vol. 89, no. 4, pp. 2481–2493, 2005.

[111] Y. Tang, G. Cao, X. Chen, J. Yoo, A. Yethiraj, and Q. Cui, "A finite element framework for studying the mechanical response of macromolecules: application to the gating of the mechanosensitive channel MscL.," *Biophysical Journal*, vol. 91, pp. 1248–63, Aug. 2006.

[112] Y. C. Zhou, B. Lu, and A. a. Gorfe, "Continuum electromechanical modeling of protein-membrane interactions," *Physical Review E*, vol. 82, p. 041923, Oct. 2010.

[113] D. Shental-Bechor, S. J. Fleishman, and N. Ben-Tal, "Has the code for protein translocation been broken?," *Trends in Biochemical Sciences*, vol. 31, pp. 192–6, Apr. 2006.

[114] M. Grabe, H. Lecar, Y. N. Jan, and L. Y. Jan, "A quantitative assessment of models for voltage-dependent gating of ion channels.," *Proceedings of the National Academy of Sciences*, vol. 101, pp. 17640–5, Dec. 2004.

[115] N. Dan and S. A. Safran, "Effect of lipid characteristics on the structure of transmembrane proteins.," *Biophysical Journal*, vol. 75, pp. 1410–4, Sept. 1998.

[116] J. Jeon and G. a. Voth, "Gating of the mechanosensitive channel protein MscL: the interplay of membrane and protein.," *Biophysical Journal*, vol. 94, pp. 3497–511, May 2008.

[117] P. C. a. van der Wel, E. Strandberg, J. A. Killian, and R. E. Koeppe, "Geometry and intrinsic tilt of a tryptophan-anchored transmembrane alpha-helix determined by (2)H NMR.," *Biophysical Journal*, vol. 83, pp. 1479–88, Sept. 2002.

[118] E. Strandberg, S. Ozdirekcan, D. T. S. Rijkers, P. C. a. van der Wel, R. E. Koeppe, R. M. J. Liskamp, and J. A. Killian, "Tilt angles of transmembrane model peptides in oriented and non-oriented lipid bilayers as determined by 2H solid-state NMR.," *Biophysical Journal*, vol. 86, pp. 3709–21, June 2004.

[119] S. Ozdirekcan, D. T. S. Rijkers, R. M. J. Liskamp, and J. A. Killian, "Influence of flanking residues on tilt and rotation angles of transmembrane peptides in lipid bilayers. A solid-state 2H NMR study.," *Biochemistry*, vol. 44, pp. 1004–12, Jan. 2005.

[120] J. C. Mills, N. L. Stone, J. Erhardt, and R. N. Pittman, "Apoptotic membrane blebbing is regulated by myosin light chain phosphorylation," *The Journal of Cell Biology*, vol. 140, no. 3, pp. 627–636, 1998.

[121] T. Hessa, H. Kim, K. Bihlmaier, C. Lundin, J. Boekel, H. Andersson, I. Nilsson, S. White, and G. Von Heijne, "Recognition of transmembrane helices by the endoplasmic reticulum translocon," *Nature*, vol. 433, pp. 377–381, Jan. 2005.

[122] J. P. Dilger, S. McLaughlin, T. J. McIntosh, S. A. Simon, *et al.*, "The dielectric constant of phospholipid bilayers and the permeability of membranes to ions.," *Science*, vol. 206, no. 4423, p. 1196, 1979.

[123] A. Finkelstein, *Water movement through lipid bilayers, pores, and plasma membranes: theory and reality.* Wiley Interscience, NY, 1987.

[124] S. Paula, A. Volkov, A. Van Hoek, T. Haines, and D. Deamer, "Permeation of protons, potassium ions, and small polar molecules through phospholipid bilayers as a function of membrane thickness," *Biophysical Journal*, vol. 70, no. 1, pp. 339–348, 1996.

[125] L. B. Li, I. Vorobyov, and T. W. Allen, "The role of membrane thickness in charged protein-lipid interactions.," *Biochimica et Biophysica Acta, Biomembranes*, vol. 1818, pp. 135–45, Feb. 2012.

[126] P. de Gennes, "Conjectures sur l'etat smectique," *Le Journal de Physique Colloques*, vol. 30, no. C4, pp. C4–65, 1969.

[127] D. Sitkoff, K. A. Sharp, and B. Honig, "Accurate calculation of hydration free energies using macroscopic solvent models," *The Journal of Physical Chemistry*, vol. 98, no. 7, pp. 1978–1988, 1994.

[128] B. Hess, C. Kutzner, D. van der Spoel, and E. Lindahl, "GROMACS 4: Algorithms for Highly Efficient, Load-Balanced, and Scalable Molecular Simulation," *Journal of Chemical Theory and Computation*, vol. 4, pp. 435–447, Mar. 2008.

[129] S. O. Yesylevskyy, L. V. Schäfer, D. Sengupta, and S. J. Marrink, "Polarizable water model for the coarse-grained MARTINI force field.," *PLoS Computational Biology*, vol. 6, p. e1000810, June 2010.

[130] H. J. C. Berendsen, J. P. M. Postma, W. F. van Gunsteren, a. DiNola, and J. R. Haak, "Molecular dynamics with coupling to an external bath," *Journal of Chemical Physics*, vol. 81, no. 8, p. 3684, 1984.

[131] J. S. Hub, B. L. D. Groot, and D. V. D. Spoel, "g_wham A Free Weighted Histogram Analysis Implementation Including Robust Error and Autocorrelation Estimates," *Journal of Chemical Theory and Computation*, vol. 6, pp. 3713–3720, 2010.

[132] S. Kumar, D. Bouzida, R. Swendsen, P. Kollman, and J. Rosenberg, "The weighted histogram analysis method for free-energy calculations on biomolecules," *Journal of Computational Chemistry*, vol. 13, no. 8, pp. 1011–1021, 1992.

[133] S. Paula, A. Volkov, and D. Deamer, "Permeation of halide anions through phospholipid bilayers occurs by the solubility-diffusion mechanism.," *Biophysical Journal*, vol. 74, pp. 319–27, Jan. 1998.

[134] W. Rawicz, K. C. Olbrich, T. McIntosh, D. Needham, and E. Evans, "Effect of chain length and unsaturation on elasticity of lipid bilayers.," *Biophysical Journal*, vol. 79, pp. 328–39, July 2000.

[135] H. Tepper and G. Voth, "Mechanisms of passive ion permeation through lipid bilayers: insights from simulations," *Journal of Physical Chemistry B*, vol. 110, no. 42, pp. 21327–21337, 2006.

[136] H. Leontiadou, A. E. Mark, and S.-J. Marrink, "Ion transport across transmembrane pores.," *Biophysical Journal*, vol. 92, pp. 4209–15, June 2007.

[137] I. V. Khavrutskii, A. a. Gorfe, B. Lu, and J. A. McCammon, "Free energy for the permeation of Na(+) and Cl(-) ions and their ion-pair through a zwitterionic dimyristoyl phosphatidylcholine lipid bilayer by umbrella integration with harmonic fourier beads.," *Journal of the American Chemical Society*, vol. 131, pp. 1706–16, Feb. 2009.

[138] A. M. Smondyrev and M. L. Berkowitz, "United atom force field for phospholipid membranes: constant pressure molecular dynamics simulation of dipalmitoylphosphatidicholine/water system," *Journal of Computational Chemistry*, vol. 20, no. 5, pp. 531–545, 1999.

[139] S. A. Pandit, D. Bostick, and M. L. Berkowitz, "Molecular dynamics simulation of a dipalmitoylphosphatidylcholine bilayer with nacl," *Biophysical Journal*, vol. 84, no. 6, p. 3743, 2003.

[140] V. Knecht and B. Klasczyk, "Specific binding of chloride ions to lipid vesicles and implications at molecular scale," *Biophysical Journal*, vol. 104, no. 4, pp. 818–824, 2013.

[141] H. Herce, A. Garcia, J. Litt, R. Kane, P. Martin, N. Enrique, A. Rebolledo, and V. Milesi, "Arginine-rich peptides destabilize the plasma membrane, consistent with a pore formation translocation mechanism of cell-penetrating peptides," *Biophysical Journal*, vol. 97, no. 7, pp. 1917–1925, 2009.

[142] S. Yesylevskyy, S.-J. Marrink, and A. E. Mark, "Alternative mechanisms for the interaction of the cell-penetrating peptides penetratin and the tat peptide with lipid bilayers," *Biophysical Journal*, vol. 97, no. 1, pp. 40–49, 2009.

[143] H. Leontiadou, A. E. Mark, and S. J. Marrink, "Antimicrobial peptides in action," *Journal of the American Chemical Society*, vol. 128, no. 37, pp. 12156–12161, 2006.

[144] K. Kuroda, G. A. Caputo, and W. F. DeGrado, "The role of hydrophobicity in the antimicrobial and hemolytic activities of polymethacrylate derivatives," *Chemistry-a European Journal*, vol. 15, no. 5, pp. 1123–1133, 2009.

[145] J. N. Horn, J. D. Sengillo, D. Lin, T. D. Romo, and A. Grossfield, "Characterization of a potent antimicrobial lipopeptide via coarse-grained molecular dynamics," *Biochimica et Biophysica Acta, Biomembranes*, vol. 1818, no. 2, pp. 212–218, 2012.

[146] M. L. Reese and J. C. Boothroyd, "A helical membrane-binding domain targets the toxoplasma rop2 family to the parasitophorous vacuole," *Traffic*, vol. 10, no. 10, pp. 1458–1470, 2009.

[147] M. L. Reese, G. M. Zeiner, J. P. Saeij, J. C. Boothroyd, and J. P. Boyle, "Polymorphic family of injected pseudokinases is paramount in toxoplasma virulence," *Proceedings of the National Academy of Sciences*, vol. 108, no. 23, pp. 9625–9630, 2011.

[148] M. S. Behnke, A. Khan, J. C. Wootton, J. P. Dubey, K. Tang, and L. D. Sibley, "Virulence differences in toxoplasma mediated by amplification of a family of polymorphic pseudokinases," *Proceedings of the National Academy of Sciences*, vol. 108, no. 23, pp. 9631–9636, 2011.

[149] T. Kim, K. I. Lee, P. Morris, R. W. Pastor, O. S. Andersen, and W. Im, "Influence of hydrophobic mismatch on structures and dynamics of gramicidin a and lipid bilayers," *Biophysical Journal*, vol. 102, no. 7, pp. 1551–1560, 2012.

[150] T. Rezai, J. E. Bock, M. V. Zhou, C. Kalyanaraman, R. S. Lokey, and M. P. Jacobson, "Conformational flexibility, internal hydrogen bonding, and passive membrane permeability: successful in silico prediction of the relative permeabilities of cyclic peptides," *Journal of the American Chemical Society*, vol. 128, no. 43, pp. 14073–14080, 2006.

[151] J. Warwicker and H. Watson, "Calculation of the electric potential in the active site cleft due to α-helix dipoles," *Journal of Molecular Biology*, vol. 157, no. 4, pp. 671–679, 1982.

[152] R. Zauhar and R. Morgan, "A new method for computing the macromolecular electric potential," *Journal of Molecular Biology*, vol. 186, no. 4, pp. 815–820, 1985.

[153] I. Klapper, R. Hagstrom, R. Fine, K. Sharp, and B. Honig, "Focusing of electric fields in the active site of Cu-Zn superoxide dismutase: effects of ionic strength and amino-acid modification," *Proteins: Structure, Function, and Genetics*, vol. 1, no. 1, pp. 47–59, 1986.

[154] J. Warwicker, "Continuum dielectric modelling of the protein-solvent system, and calculation of the long-range electrostatic field of the enzyme phosphoglycerate mutase*," *Journal of Theoretical Biology*, vol. 121, no. 2, pp. 199–210, 1986.

[155] M. Gilson, K. Sharp, and B. Honig, "Calculating electrostatic interactions in biomolecules: method and error assessment.," *Proceedings of the National Academy of Sciences*, vol. 9, no. 4, pp. 327–335, 1987.

[156] Y. Zhou, M. Feig, and G. Wei, "Highly accurate biomolecular electrostatics in continuum dielectric environments," *Journal of Computational Chemistry*, vol. 29, no. 1, pp. 87–97, 2008.

[157] J. Grant, B. Pickup, and A. Nicholls, "A smooth permittivity function for Poisson-Boltzmann solvation methods," *Journal of Computational Chemistry*, vol. 22, no. 6, pp. 608–640, 2001.

[158] B. Brooks, C. Brooks III, A. Mackerell Jr, L. Nilsson, R. Petrella, B. Roux, Y. Won, G. Archontis, C. Bartels, S. Boresch, *et al.*, "CHARMM: the biomolecular simulation program," *Journal of Computational Chemistry*, vol. 30, no. 10, pp. 1545–1614, 2009.

[159] E. Tajkhorshid, P. Nollert, M. Jensen, L. Miercke, J. O'Connell, R. Stroud, and K. Schulten, "Control of the selectivity of the aquaporin water channel family by global orientational tuning," *Science*, vol. 296, no. 5567, pp. 525–530, 2002.

[160] S. Bernèche and B. Roux, "Energetics of ion conduction through the K+ channel.," *Nature*, vol. 414, no. 6859, pp. 73–77, 2001.

[161] J. MacCallum, M. Moghaddam, H. Chan, and D. Tieleman, "Hydrophobic association of α-helices, steric dewetting, and enthalpic barriers to protein folding," *Proceedings of the National Academy of Sciences*, vol. 104, no. 15, pp. 6206–6210, 2007.

[162] P. Bond, J. Faraldo-Gómez, S. Deol, and M. Sansom, "Membrane protein dynamics and detergent interactions within a crystal: A simulation study of OmpA," *Proceedings of the National Academy of Sciences*, vol. 103, no. 25, pp. 9518–9523, 2006.

[163] H. Petrache, D. Zuckerman, J. Sachs, J. Killian, R. Koeppe II, and T. Woolf, "Hydrophobic matching mechanism investigated by molecular dynamics simulations," *Langmuir*, vol. 18, no. 4, pp. 1340–1351, 2002.

[164] T. Allen, S. Kuyucak, and S. Chung, "Molecular dynamics study of the KcsA potassium channel," *Biophysical Journal*, vol. 77, no. 5, pp. 2502–2516, 1999.

[165] G. Khelashvili, D. Harries, and H. Weinstein, "Modeling Membrane Deformations and Lipid Demixing upon Protein-Membrane Interaction: The BAR Dimer Adsorption," *Biophysical Journal*, vol. 97, no. 6, pp. 1626–1635, 2009.

[166] G. Khelashvili, H. Weinstein, and D. Harries, "Protein diffusion on charged membranes: a dynamic mean-field model describes time evolution and lipid reorganization," *Biophysical Journal*, vol. 94, no. 7, pp. 2580–2597, 2008.

[167] D. Murray, A. Arbuzova, G. Hangyás-Mihályné, A. Gambhir, N. Ben-Tal, B. Honig, and S. McLaughlin, "Electrostatic properties of membranes containing acidic lipids and adsorbed basic peptides: theory and experiment," *Biophysical Journal*, vol. 77, no. 6, pp. 3176–3188, 1999.

[168] D. Murray, L. Hermida-Matsumoto, C. Buser, J. Tsang, C. Sigal, N. Ben-Tal, B. Honig, M. Resh, and S. McLaughlin, "Electrostatics and the membrane association of Src: theory and experiment," *Biochemistry*, vol. 37, no. 8, pp. 2145–2159, 1998.

[169] D. Murray, S. McLaughlin, and B. Honig, "The role of electrostatic interactions in the regulation of the membrane association of G protein beta gamma heterodimers," *Journal of Biological Chemistry*, vol. 276, no. 48, pp. 45153–45159, 2001.

[170] M. Feig, S. Tanizaki, and M. Sayadi, "Implicit Solvent Simulations of Biomolecules in Cellular Environments," *Annual Reports in Computational Chemistry*, vol. 4, pp. 107–121, 2008.

[171] M. Feig, W. Im, and C. Brooks III, "Implicit solvation based on generalized Born theory in different dielectric environments," *The Journal of Chemical Physics*, vol. 120, pp. 903–911, 2004.

[172] W. Im, M. Feig, and C. Brooks III, "An implicit membrane generalized born theory for the study of structure, stability, and interactions of membrane proteins," *Biophysical Journal*, vol. 85, no. 5, pp. 2900–2918, 2003.

[173] S. Tanizaki and M. Feig, "Molecular dynamics simulations of large integral membrane proteins with an implicit membrane model," *The Journal of Physical Chemistry B*, vol. 110, no. 1, pp. 548–556, 2006.

[174] E. Denning and T. Woolf, "Double Bilayers and Transmembrane Gradients: A Molecular Dynamics Study of a Highly Charged Peptide," *Biophysical Journal*, vol. 95, no. 7, pp. 3161–3173, 2008.

[175] J. Zhang and T. Lazaridis, "Calculating the free energy of association of transmembrane helices," *Biophysical Journal*, vol. 91, no. 5, pp. 1710–1723, 2006.

[176] M. Nina, S. Bernèche, and B. Roux, "Anchoring of a monotopic membrane protein: the binding of prostaglandin H 2 synthase-1 to the surface of a phospholipid bilayer," *European Biophysics Journal*, vol. 29, no. 6, pp. 439–454, 2000.

[177] B. Roux, S. Berneche, and W. Im, "Ion channels, permeation, and electrostatics: insight into the function of KcsA," *Biochemistry*, vol. 39, no. 44, pp. 13295–13306, 2000.

[178] A. Philippsen, W. Im, A. Engel, T. Schirmer, B. Roux, and D. Müller, "Imaging the electrostatic potential of transmembrane channels: atomic probe microscopy of OmpF porin," *Biophysical Journal*, vol. 82, no. 3, pp. 1667–1676, 2002.

[179] J. Faraldo-Gómez, B. Roux, *et al.*, "Electrostatics of ion stabilization in a ClC chloride channel homologue from Escherichia coli," *Journal of Molecular Biology*, vol. 339, no. 4, pp. 981–1000, 2004.

[180] B. Chanda, O. Asamoah, R. Blunck, B. Roux, and F. Bezanilla, "Gating charge displacement in voltage-gated ion channels involves limited transmembrane movement," *Nature*, vol. 436, no. 7052, pp. 852–856, 2005.

[181] V. Jogini and B. Roux, "Electrostatics of the intracellular vestibule of K+ channels," *Journal of Molecular Biology*, vol. 354, no. 2, pp. 272–288, 2005.

[182] J. Robertson, L. Palmer, and B. Roux, "Long-pore electrostatics in inward-rectifier potassium channels," *Journal of General Physiology*, vol. 132, no. 6, pp. 613–632, 2008.

[183] Y. Jiang, A. Lee, J. Chen, M. Cadene, B. Chait, and R. MacKinnon, "The open pore conformation of potassium channels," *Nature*, vol. 417, no. 6888, pp. 523–526, 2002.

[184] R. Hilf and R. Dutzler, "X-ray structure of a prokaryotic pentameric ligand-gated ion channel," *Nature*, vol. 452, no. 7185, pp. 375–379, 2008.

[185] F. Chatelain, N. Alagem, Q. Xu, R. Pancaroglu, E. Reuveny, and D. Minor Jr, "The pore helix dipole has a minor role in inward rectifier channel function," *Neuron*, vol. 47, no. 6, pp. 833–843, 2005.

[186] S. Jo, M. Vargyas, J. Vasko-Szedlar, B. Roux, and W. Im, "PBEQ-Solver for online visualization of electrostatic potential of biomolecules," *Nucleic Acids Research*, vol. 36, no. Web Server issue, pp. W270–W275, 2008.

[187] "Jmol: an open-source Java viewer for chemical structures in 3D.." http://www.jmol.org/.

[188] T. Dolinsky, P. Czodrowski, H. Li, J. Nielsen, J. Jensen, G. Klebe, and N. Baker, "PDB2PQR: expanding and upgrading automated preparation of biomolecular structures for molecular simulations," *Nucleic Acids Research*, vol. 35, no. Web Server issue, pp. W522–W525, 2007. http://www.poissonboltzmann.org/pdb2pqr/.

[189] A. MacKerell, D. Bashford, M. Bellott, R. Dunbrack, J. Evanseck, M. Field, S. Fischer, J. Gao, H. Guo, S. Ha, *et al.*, "All-atom empirical potential for molecular modeling and dynamics studies of proteins," *Journal of Physical Chemistry B*, vol. 102, no. 18, pp. 3586–3616, 1998.

[190] J. Swanson, J. Wagoner, N. Baker, and J. McCammon, "Optimizing the Poisson dielectric boundary with explicit solvent forces and energies: Lessons learned with atom-centered dielectric functions," *Journal of Chemical Theory and Computation*, vol. 3, no. 1, pp. 170–183, 2007.

[191] J. Wang, P. Cieplak, and P. Kollman, "How well does a restrained electrostatic potential(RESP) model perform in calculating conformational energies of organic and biological molecules?," *Journal of Computational Chemistry*, vol. 21, no. 12, pp. 1049–1074, 2000.

[192] D. Green and B. Tidor, "Evaluation of ab initio charge determination methods for use in continuum solvation calculations," *The Journal of Physical Chemistry B*, vol. 107, no. 37, pp. 10261–10273, 2003.

[193] J. Silva, H. Pan, D. Wu, A. Nekouzadeh, K. Decker, J. Cui, N. Baker, D. Sept, and Y. Rudy, "A multiscale model linking ion-channel molecular dynamics and electrostatics to the cardiac action potential," *Proceedings of the National Academy of Sciences*, vol. 106, no. 27, pp. 11102–11106, 2009.

[194] J. Jackson, *Classical Electrodynamics, Second Edition.* 1975.

[195] W. Humphrey, A. Dalke, and K. Schulten, "VMD – Visual Molecular Dynamics," *Journal of Molecular Graphics*, vol. 14, pp. 33–38, 1996.

[196] B. Hille, "Ionic channels of excitable membranes. Sunderland, MA," *Sinauer Associates Inc, 426pp*, vol. 174, pp. 289–300, 1984.

[197] O. Beckstein, K. Tai, and M. Sansom, "Not ions alone: barriers to ion permeation in nanopores and channels.," *Journal of the American Chemical Society*, vol. 126, no. 45, pp. 14694–14695, 2004.

[198] B. Roux and R. MacKinnon, "The cavity and pore helices in the KcsA K+ channel: electrostatic stabilization of monovalent cations," *Science*, vol. 285, no. 5424, pp. 100–102, 1999.

[199] R. Ujwal, D. Cascio, J. Colletier, S. Faham, J. Zhang, L. Toro, P. Ping, and J. Abramson, "The crystal structure of mouse VDAC1 at 2.3 Å resolution reveals mechanistic insights into metabolite gating," *Proceedings of the National Academy of Sciences*, vol. 105, no. 46, pp. 17742–17747, 2008.

[200] O. P. Choudhary, R. Ujwal, W. Kowallis, R. Coalson, J. Abramson, and M. Grabe, "The Electrostatics of VDAC: Implications for Selectivity and Gating," *Journal of Molecular Biology*, vol. 396, no. 3, pp. 580–592, 2010.

[201] N. Bhardwaj, R. V. Stahelin, R. E. Langlois, W. Cho, and H. Lu, "Structural bioinformatics prediction of membrane-binding proteins," *Journal of Molecular Miology*, vol. 359, no. 2, pp. 486–495, 2006.

[202] M. V. Shapovalov and R. L. Dunbrack Jr, "A smoothed backbone-dependent rotamer library for proteins derived from adaptive kernel density estimates and regressions," *Structure*, vol. 19, no. 6, pp. 844–858, 2011.

[203] S. C. Botelho, M. Osterberg, A. S. Reichert, K. Yamano, P. Björkholm, T. Endo, G. von Heijne, and H. Kim, "TIM23-mediated insertion of transmembrane α-helices into the mitochondrial inner membrane.," *The EMBO Journal*, vol. 30, pp. 1003–1011, Feb. 2011.

[204] M. Nina, D. Beglov, and B. Roux, "Atomic radii for continuum electrostatics calculations based on molecular dynamics free energy simulations," *The Journal of Physical Chemistry B*, vol. 101, no. 26, pp. 5239–5248, 1997.

[205] J. Chen, W. Im, and C. L. Brooks, "Balancing solvation and intramolecular interactions: toward a consistent generalized Born force field.," *Journal of the American Chemical Society*, vol. 128, pp. 3728–36, Mar. 2006.